TECHNISCHE UNIVERSITÄT WIEN

# Diplomarbeit

# Electrochemical properties of $La_{0.6}Sr_{0.4}FeO_{3-\delta}$ upon polarization

Ausgeführt am

Institut für Chemische Technologie und Analytik
der Technischen Universität Wien

unter Anleitung von

Univ.-Prof. Dipl.-Phys. Dr. Jürgen Fleig
Univ.Ass. Dipl.-Ing. Ghislain M. Rupp

durch

Alexander Schmid
Alliiertenstrasse 9/18
A-1020 Wien

Wien, im Februar 2016

Alexander Schmid

# Abstract

The perovskite-type oxide $La_{0.6}Sr_{0.4}FeO_{3-\delta}$ (LSF) is a mixed ionic and electronic conductor. Its high ionic and electronic conductivity, acceptable catalytic activity for the oxygen exchange reaction along with its chemical stability over a wide range of oxygen partial pressures make it an attractive electrode material for solid oxide fuel cells and solid oxide electrolysis cells. In this study electrochemical impedance spectroscopy was used to characterize well defined thin film LSF electrodes in different atmospheres and at varying bias voltages. This allowed to study the effects of chemical potential of oxygen in the atmosphere and electrical potential of the electrode on charge carrier concentrations (defect chemistry) and oxygen exchange kinetics.

It could be shown, that the chemical capacitance (as a measure of the charge carrier concentration in the material) solely depends on the potential of oxygen within the electrode, independent of its origin (either by atmospheric oxygen partial pressure or applied electrode potential). Comparison with calculations based on defect chemical bulk data exhibited qualitative agreement between calculated and measured chemical capacitance over a wide range of oxygen partial pressure. However, the chemical capacitance of the thin films was shown to be lower than expected from bulk data.

Impedance spectroscopy on samples with three electrode geometry in different oxidizing atmospheres revealed different impacts of atmosphere and polarization on oxygen incorporation and oxygen release reaction. While the oxygen incorporation reaction exhibits strong dependance on the atmosphere at equal electrode potential, the oxygen release reaction was shown to be less dependent on the atmosphere but strongly affected by the chemical potential of oxygen within the electrode.

# Contents

# 1 Introduction

With the ever growing demands on electrical energy, various challenges have to be overcome. Decentralized, adaptable energy production systems have to be established. Furthermore, reduced $CO_2$ and particulates emission is strongly emphasized. Solid oxide fuel cells (SOFCs) offer several advantages over conventional production of electrical energy, and therefore show great potential for meeting these challenges.

In SOFCs, the chemical energy bound in fuel and oxidizer is directly transformed into electrical energy, contrary to the conventional approach over thermal and mechanical energy. SOFCs offer high energy conversion efficiency with experimentally realized values as high as 60 %. Fuel flexibility as well as scalability make SOFCs a very adaptable versatile solution for a broad range of applications, such as auxiliary power units and combined power and heating systems. [1]

When operated in the reverse direction, SOFCs can be used for electrolytic splitting of water into oxygen and hydrogen. In this mode they are referred to as solid oxide electrolysis cells, SOEC. A combination of SOECs and SOFCs offers great potential as load balancing system, since excess energy from the power grid can be transformed into much easier storable fuel, and reconverted to electrical energy when needed. With the current trend towards renewable energy sources, the availability of high performance load balancing systems is of vital importance, as many renewable energy sources like solar power or wind power provide fluctuating power output. [2]

However, for SOFCs to be competitive in the energy market major obstacles have to be overcome. Long term stability of the electrodes is still a problem, in part due to high operation temperatures. Furthermore, special materials are needed for high temperature sealing and current collection, which leads to economic obstacles. The development of high performance electrode materials for lower temperatures is therefore a main goal. [1] [3] [2] [4]

State of the art anodes are currently made of Ni/YSZ (yttria stabilized zirconia) cermet. However, these electrodes are prone to sulfur poisoning, which is a major drawback if biogas or diesel is considered as fuel. Finding alternative anode materials would therefore be desirable. Perovskite type oxides offer an alternative to Ni/YSZ cermets. As they are often mixed ionic and electronic conductors (MIECs) greater parts of the surface area are active towards oxygen exchange reaction, compared with the Ni/YSZ where oxygen exchange only takes place at the triple phase boundary. However, the reducing conditions at the anode side can proof challenging in view of thermochemical stability of these oxides. [5] [6] [7]

Perovskite type oxides are already employed as cathode materials in oxidizing conditions, most SOFCs use (La,Sr)$MnO_3$ as cathode material. However, because of its limited electrochemical performance, other perovskite materials like (La,Sr)$CoO_3$, (La,Sr)(Cr,Mn)$O_3$ and (Sr,La)(Ti,Fe)$O_3$ are investigated in search for high performance SOFC cathode materials. Long

term stability and resistance to poisoning effects are still major obstacles. A better understanding of the electrochemical processes involved in the oxygen exchange reaction could help in overcoming these issues. [8] [9] [10] [11] [12] [13] [14] [15]

A promising member of the perovskite class of mixed conducting oxides is $La_{0.6}Sr_{0.4}FeO_{3-\delta}$ (LSF). Due to its stability over a wide range of oxygen partial pressures LSF is both a promising anode and cathode material for SOFCs and SOECs. Furthermore, LSF offers good compatibility with YSZ and gadolinium doped ceria (GDC) in terms of thermal expansion [16] [17], and reactions between electrolyte and electrode material (at temperatures beneath 900 °C in case of a YSZ substrate [18]). Various studies on electronic and ionic charge transport [19] [20] [21] [22] [23] [24], oxygen exchange and diffusion coefficients [25] [26] [27] [28] and on the defect chemistry [17] [29] [19] have been done at different oxygen partial pressures.

To gain better understanding of the fundamental processes governing the oxygen exchange, it is helpful to investigate oxygen evolution and oxygen incorporation independently which is possible by electrochemical impedance spectroscopy under polarization. Furthermore, a variation of the defect chemical state of the electrode independent of oxygen partial pressure could also improve knowledge on parameters and processes governing the oxygen exchange. Such a variation of defect concentrations in a fixed gas atmosphere is again possible by applying a bias voltage. For example, Kawada et.al. showed that the defect chemical state of $(La,Sr)CoO_{3-\delta}$ can be tuned independent of the oxygen partial pressure. [30]

In this study, impedance spectroscopy was applied to investigate polarized LSF thin film electrodes. The main goal was to evaluate the possibility of decoupling the effects of voltage and external atmosphere on the defect concentrations and on the electrochemical processes at the surface. The influence of bias polarization under different atmospheres on the defect chemistry and oxygen exchange kinetics of LSF was therefore investigated in detail. Thus, the similarities but also the differences of oxygen partial pressure changes and bias changes could be elucidated.

# 2 Theoretical background

## 2.1 Crystal structure and defect chemistry in LSF

$La_{0.6}Sr_{0.4}FeO_{3-\delta}$ crystallizes in the perovskite structure, depicted in figure 2.1. The general formula of perovskites is $ABO_3$, where A is a larger cation than B, with a combined valence of +6. In LSF the B site is occupied by $Fe^{3+}$ and the A site is occupied by $La^{3+}$ and $Sr^{2+}$. LSF can therefore be seen as solid solution of $SrFeO_3$ in $LaFeO_3$. The substitution of $La^{3+}$ by $Sr^{2+}$ causes a shortage of positive charge, which in Kröger Vink notation can be expressed as a negative charge relative to the pure LaFeO3 structure, $Sr'_{La}$.

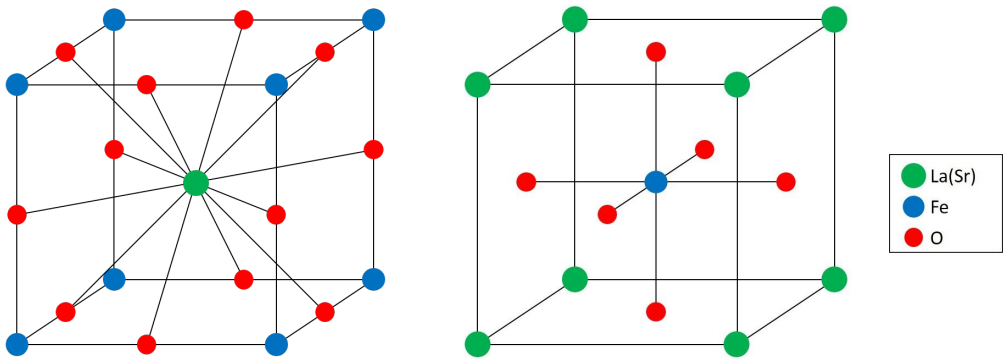


(a) A-centered (b) B-centered

Figure 2.1: Idealized cubic perovskite structure of LSF, A-centered and B-centered view.

Both, strontium and lanthanum have a fixed valence. Iron on the other hand can adopt different valence states, therefore the relative negative charge can be electronically compensated by introduction of electron holes ($Fe^{\bullet}_{Fe}$) localized at or close to the iron ion which is equivalent to an oxidation of the iron ion to a nominal oxidation state of $Fe^{4+}$, see equation 2.1. Similarly $Fe^{2+}$ is interpreted as an electron ($Fe'_{Fe}$). [17] [21] Electron holes and electrons are coupled by the equilibrium described in equation 2.2.

$$Sr'_{La} \longrightarrow Fe^{\bullet}_{Fe} \tag{2.1}$$

$$2\,Fe^{\times}_{Fe} \rightleftharpoons Fe'_{Fe} + Fe^{\bullet}_{Fe} \tag{2.2}$$

Additionally, ionic compensation takes place via the introduction of oxygen vacancies, see equation 2.3.

$$Sr'_{La} \longrightarrow \tfrac{1}{2}\, V^{\bullet\bullet}_{O} \tag{2.3}$$

These two mechanisms enable LSF to undergo oxygen exchange reaction, described by equation 2.4: Oxygen can be released from the material, thereby forming an oxygen vacancy $V^{\bullet\bullet}_{O}$ and two electron holes $Fe^{\bullet}_{Fe}$ and vice versa.

$$V^{\bullet\bullet}_{O} + \tfrac{1}{2}\, O_2 + 2\, Fe^{\times}_{Fe} \rightleftharpoons O^{\times}_{O} + 2\, Fe^{\bullet}_{Fe} \tag{2.4}$$

From equations 2.2 and 2.4 it is evident, that the concentrations of the charge carriers (oxygen vacancies, electron holes and electrons) depend on the oxygen partial pressure. At high oxygen partial pressure the equilibrium is on the right hand side, thus few oxygen vacancies and many electron holes are present, leading to low ionic and high electronic conductivity. At lower oxygen partial pressures the equilibrium shifts to the left hand side, leading to more oxygen vacancies and less electron holes. If the atmosphere contains hydrogen, the oxygen nonstoichiometry is governed by different reacting species, see equation 2.5. [16] [17] [19] [21] [22] [24] [31] [32]

$$V^{\bullet\bullet}_{O} + H_2O + 2\, Fe'_{Fe} \rightleftharpoons O^{\times}_{O} + 2\, Fe^{\times}_{Fe} + H_2 \tag{2.5}$$

## 2.2 Defect chemical calculations

### 2.2.1 Calculation of the Brouwer diagram

According to the defect model for LSF [17], there are two equilibria responsible for the concentration of charge carriers. Equation 2.6 describes the mass action law for the oxygen exchange reaction (equation 2.4).

$$K_{Ox} = \frac{c(O^{\times}_{O}) \times c(Fe^{\bullet}_{Fe})^2}{c(V^{\bullet\bullet}_{O}) \times \sqrt{p(O_2)} \times c(Fe^{\times}_{Fe})^2} \tag{2.6}$$

Additionally the balance for oxygen sites (equation 2.7) has to be fulfilled, where $c_0(O)$ represents the concentration of oxygen sites in the crystal.

$$c(V^{\bullet\bullet}_{O}) + c(O^{\times}_{O}) = c_0(O) \tag{2.7}$$

The second equilibrium is the disproportion of iron, respectively the formation of electrons and electron holes, see equations 2.2 and 2.8.

$$K_i = \frac{c(Fe^{\bullet}_{Fe}) \times c(Fe^{\bullet}_{Fe})}{c(Fe^{\times}_{Fe})^2} \tag{2.8}$$

Additionally, as both electrons and holes are located at the iron, the following balance, equation 2.9, has to be fulfilled, where $c_0(Fe)$ denotes for the concentration of iron sites in the lattice, which is a third of the oxygen site concentration.

$$c(\mathrm{h}^{\bullet}) + c(\mathrm{e}') + c(\mathrm{Fe}^{3+}) = c_0(\mathrm{Fe}) \tag{2.9}$$

Since the material has to stay electroneutral, charge balance (equation 2.10) must be fulfilled.

$$c(\mathrm{Sr}'_{\mathrm{La}}) + c(\mathrm{e}') = 2 \times c(\mathrm{V}^{\bullet\bullet}_{\mathrm{O}}) + c(\mathrm{h}^{\bullet}) \tag{2.10}$$

Combining equations 2.6 to 2.10 the concentrations of oxygen vacancies, electron holes and electrons can be numerically calculated as a function of the oxygen partial pressure. $K_i$ and $K_{Ox}$ can be calculated according to equations 2.11 and 2.12 using thermodynamic data ($\Delta H_{Ox} = -95.62\,\mathrm{kJ\,mol^{-1}}$, $\Delta S_{Ox} = -54.27\,\mathrm{J\,mol^{-1}\,K^{-1}}$, $\Delta H_i = 95.75\,\mathrm{kJ\,mol^{-1}}$ and $\Delta S_i = -21.63\,\mathrm{J\,mol^{-1}\,K^{-1}}$) determined by thermogravimetric measurements [17]and the concentration of oxygen sites from [25]. Figure 2.2 shows the resulting Brouwer diagram for LSF at 625 °C.

$$K_{Ox} = e^{\left(\frac{\Delta H_{Ox}}{R \times T} - \frac{\Delta S_{Ox}}{R}\right)} \tag{2.11}$$

$$K_i = e^{\left(\frac{\Delta H_i}{R \times T} - \frac{\Delta S_i}{R}\right)} \tag{2.12}$$

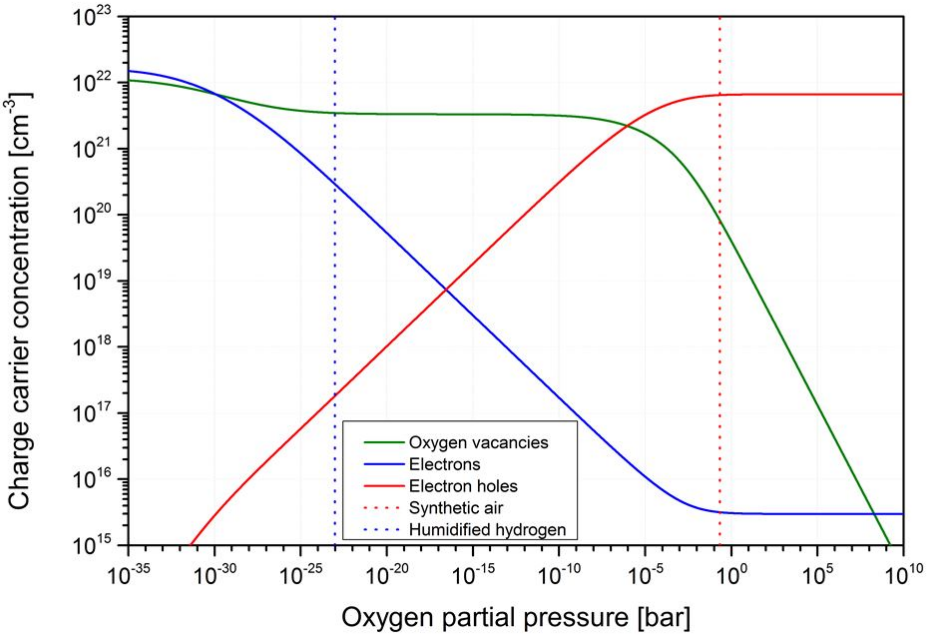


Figure 2.2: Brouwer diagram for LSF at 625 °C, calculated from literature data [17]. The dotted lines mark the two atmospheres mainly used in this work for impedance spectroscopy measurements.

### 2.2.2 Calculation of the chemical capacitance

In MIECs two different charge carrier species are present. In LSF these are oxygen vacancies (ionic) and, depending on the oxygen partial pressure, electrons or electron holes (electronic). The equilibrium concentrations of these charge carriers depend on the chemical potential of oxygen in LSF, which itself is given by oxygen partial pressure and polarization, see section 2.3.4.

Therefore, applying voltage shifts this equilibrium, thereby changing the stoichiometry of the material. This can be seen as transfer of charge between ionic and electronic charge carriers and causes a capacitive response to the applied voltage. This capacitance is referred to the chemical capacitance. [33] [34] [35]

Assuming an ideal solution behavior with no interactions between individual charge carriers, the chemical capacitance is given by equation 2.13. Based upon the concentrations of charge carriers calculated in section 2.2.1, the chemical capacitance per volume can then be calculated as a function of the oxygen partial pressure, see figure 2.3. From equation 2.13 it is obvious that the concentration of the minority charge carrier species (ionic or electronic) dominates the chemical capacitance, as shown in figure 2.3.

$$C_{Chem} = \frac{e^2}{k \times T} \times \left( \frac{1}{z_{ion}^2 \times c_{ion}} + \frac{1}{z_{eon}^2 \times c_{eon}} \right)^{-1} \tag{2.13}$$

If only electron holes are considered as electronic charge carriers, which is valid in oxidizing atmospheres, equation 2.10 can be simplified to equation 2.14.

$$c(\mathrm{Sr}'_{\mathrm{La}}) = 2 \times c(\mathrm{V}_{\mathrm{O}}^{\bullet\bullet}) + c(\mathrm{h}^{\bullet}) \tag{2.14}$$

The chemical capacitance is then given by equation 2.15.

$$C_{Chem} = \frac{e^2}{k \times T} \times \left( \frac{1}{2 \times \left( c\left(\mathrm{Sr}'_{\mathrm{La}}\right) - c\left(\mathrm{h}^{\bullet}\right) \right)} + \frac{1}{c\left(\mathrm{h}^{\bullet}\right)} \right)^{-1} \tag{2.15}$$

Thus, the chemical capacitance reaches a maximum if equation 2.16 is fulfilled.

$$c\left(\mathrm{h}^{\bullet}\right) = c\left(\mathrm{Sr}'_{\mathrm{La}}\right) \times \left(2 - \sqrt{2}\right) \tag{2.16}$$

Combining equations 2.15 and 2.16 then yields the maximum chemical capacitance, according to equation 2.17.

$$C_{Chem,max} = \frac{e^2}{k \times T} \times c\left(\mathrm{Sr}'_{\mathrm{La}}\right) \times \left(6 - 4 \times \sqrt{2}\right) \tag{2.17}$$

Hence, as long as defects show an ideal solution behavior, the maximum chemical capacitance solely depends on the dopant concentration $c(\mathrm{Sr}'_{\mathrm{La}})$.

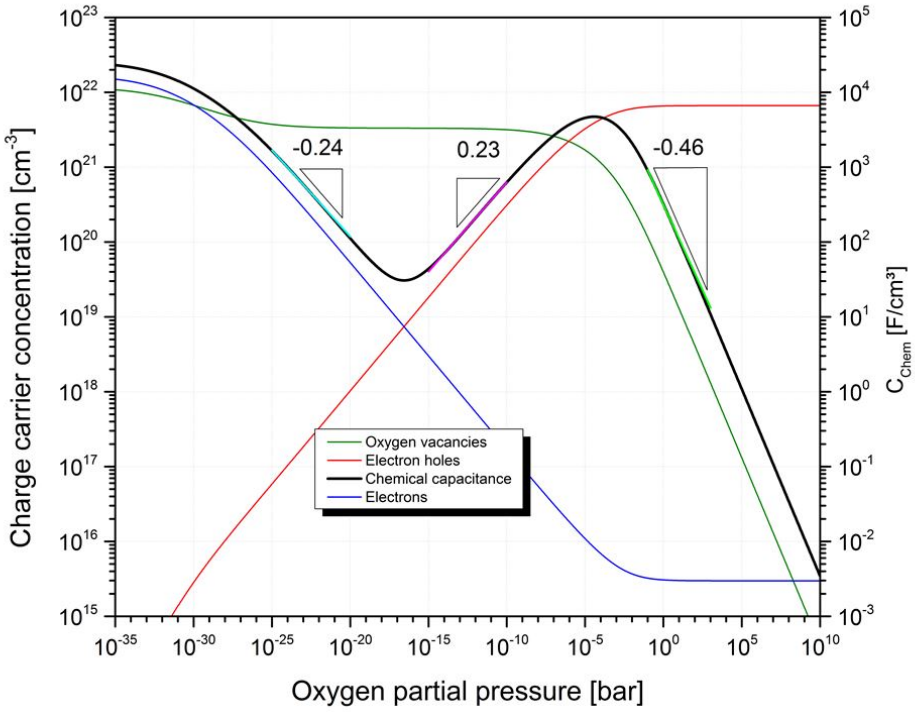


Figure 2.3: Brouwer diagram and calculated chemical capacitance for LSF at 625 °C with characteristic slopes. Chemical capacitances were calculated assuming charge carriers exhibit perfect solution behavior.

## 2.3 Impedance spectroscopy

Impedance spectroscopy is among the most useful techniques for the characterization of electrical or electrochemical systems. Advantages of impedance spectroscopy include a relatively simple experimental setup, a broad usability and being a non destructive analysis method. One of the major difficulties in impedance spectroscopy often is the correct interpretation of the spectra, in order to obtain physically meaningful parameters.

### 2.3.1 Working principle

The basic working principle of impedance spectroscopy is the frequency dependent measurement of the complex AC resistance, the impedance. For monochromatic sine shaped voltage signals and linear systems the responding current also follows a sine wave shifted by the phase angle $\varphi$. The impedance can then be expressed as the ratio of voltage amplitude divided by current amplitude and a phase factor, see equation 2.18. A phase angle of 0° represents purely ohmic behavior, while phase angles of 90° and −90° characterize inductive and capacitive behavior.

$$Z(\omega) = \frac{U(\omega)}{I(\omega)} \times e^{i \times \varphi(\omega)} \tag{2.18}$$

Similar to DC measurements, Kirchhoff's laws apply to describe and characterize networks of individual resistive, capacitive and inductive elements. The total impedance of elements in series is equal to the sum of the individual impedances while for parallel elements it is equal to one over the sum of the reciprocal impedances, see equations 2.19 and 2.20. The impedance of the three basic elements of electronic engineering, resistor, inductor and capacitor is given by equations 2.21 to 2.23.

$$Z_{1-2} = Z_1 + Z_2 \tag{2.19}$$

$$Z_{1||2} = \frac{Z_1 \times Z_2}{Z_1 + Z_2} \tag{2.20}$$

$$Z_{Resistive} = R \tag{2.21}$$

$$Z_{Inductive} = i \times \omega \times L \tag{2.22}$$

$$Z_{Capacitive} = \frac{1}{i \times \omega \times C} \tag{2.23}$$

### 2.3.2 Impedance spectra

Impedance spectra can be visualized in various ways of which two are common in electrochemistry:

- Nyquist plot: In the Nyquist plot, the imaginary part of the impedance is plotted against its real part.
- Bode plot: The Bode plot is usually a combination of two graphs, one describing magnitude and the other the phase angle as a function of the logarithmic frequency.

Both plots contain the same information but emphasize different aspects and characteristic information.

### 2.3.3 Electrochemical impedance spectroscopy

In electrochemistry, various processes can be probed by impedance spectroscopy. Therefore, often multiple individual processes contribute to a single impedance spectrum and complicate quantitative interpretation.

In the most basic case, charge transport through a material (either electronic or ionic current) can be described by a resistance. In addition to this Faraday current, displacement currents can be described by a capacitance. Chemical reactions can be probed by impedance spectroscopy, if they involve a net flow of current. The reaction is then driven back and forth by the applied alternating voltage and the reaction rate can then be described as a resistance. Higher reaction rates involve higher currents and thus lower resistances. At interfaces between different phases, the charge transport across this interface can be described by a resistance. In addition interfacial capacitances often occur.

Furthermore, if there are different charge carrier species present within the material, as is the case in MIECs, the equilibrium of these charge carriers is periodically shifted by the applied

voltage signal, resulting in capacitive behavior, called the chemical capacitance. The chemical capacitance therefore describes the ability of a material to change its stoichiometry with applied voltage. Capacitances often behave non ideal, due to inhomogeneities, grain boundaries, etc. A constant phase element can be used instead of a capacitance to account for non ideal behavior. The impedance of a constant phase element is given by equation 2.24, where $P$ quantifies the nonideality , and $T$ the capacitance. The capacitance of a constant phase element is given by equation 2.25. A $P$ value of 1 describes a perfect capacitor with a capacitance of $T$, a value of zero describes a perfect resistor.

$$Z_{CPE} = \frac{1}{(i \times \omega)^P \times T} \tag{2.24}$$

$$C_{CPE} = \left(R^{(1-P)} \times T\right)^{\frac{1}{P}} \tag{2.25}$$

### 2.3.4 Measurements with DC bias

As described, in electrochemical impedance spectroscopy a reaction is driven back and forth by an alternating voltage, around its equilibrium i.e. around the voltage zero point. In bias impedance spectroscopy an additional DC voltage (bias) causes an additional net reaction rate and thus an additional net DC current. The reaction is then probed in the vicinity of a certain non-equilibrium steady state, i.e. around a certain point on the current voltage curve. Figure 2.4 shows the voltage current characteristic for an arbitrary electrochemical reaction and two ranges probed by impedance spectroscopy with and without bias.

Figure 2.5 shows the electrochemical potential distributions of oxygen $\tilde{\mu}(O)$, oxygen ions $\tilde{\mu}(O^{2-})$, and electrons $\tilde{\mu}(e^-)$ across an idealized cell. In the gas phase the electrochemical potential of oxygen is equal to the chemical potential of oxygen and defined by the partial pressure of oxygen. The gas phase is assumed to be homogenous, therefore the electrochemical potential of oxygen is constant and equal for both sides.

In an oxide electrode, there is no oxygen present, therefore the electrochemical potential of oxygen is defined by the electrochemical potentials of electrons and oxygen ions according to equation 2.26. An ideal counter electrode (CE) is always in equilibrium with the gas phase, and therefore has a fixed electrochemical potentials of oxygen, oxygen ions and electrons, irrespective of applied voltage.

$$\tilde{\mu}(O) = \tilde{\mu}(O^{2-}) - 2 \times \tilde{\mu}(e^-) \tag{2.26}$$

Between working electrode (WE) and counter electrode (CE) a voltage $U_{DC}$ (Bias), i.e. a difference in the electrochemical potential of electrons, is applied, see equation 2.27.

$$\Delta\tilde{\mu}(e^-) = F \times U_{DC} \tag{2.27}$$

As both electrodes have high electronic conductivity, these electrochemical potentials are constant within each electrode. This potential difference and the finite ionic conductivity of the electrolyte cause the electrochemical potential of oxygen ions to change across the thickness of the electrolyte, according to equation 2.28, where $I_{DC}$ is the DC current and $R_{YSZ}$ is the ionic

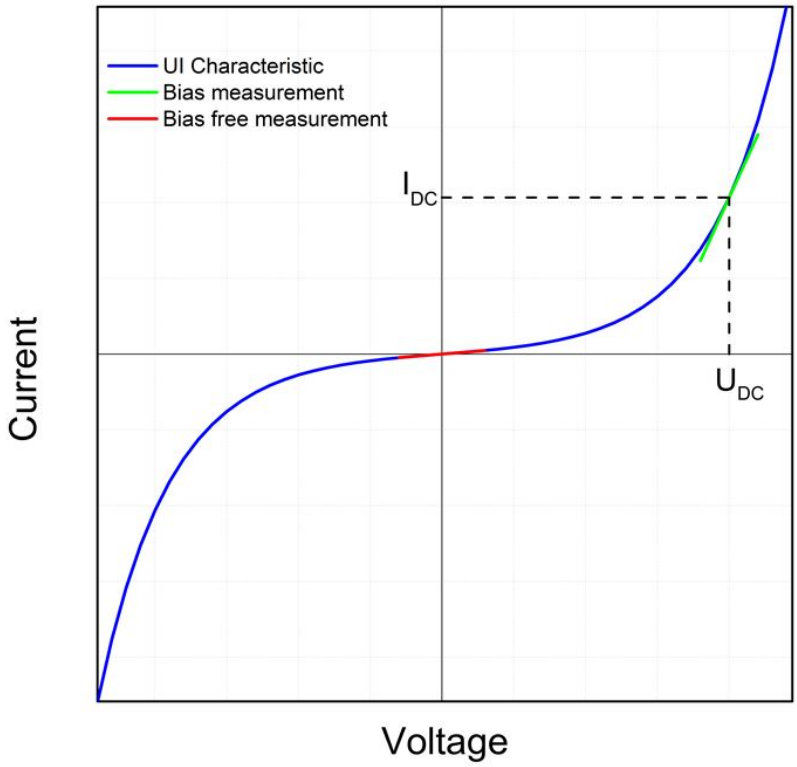


Figure 2.4: Voltage current characteristic of an arbitrary electrochemical reaction (blue) and measurement ranges for impedance spectroscopy with (green) and without (red) bias.

transport resistance of the electrolyte.

$$\Delta\tilde{\mu}(O^{2-}) = 2 \times F \times I_{DC} \times R_{YSZ} \tag{2.28}$$

This difference in electrochemical potential of oxygen ions is a part of the applied voltage, and is referred to as the Ohmic overpotential, $\eta_{YSZ}$, according to equation2.29.

$$\eta_{YSZ} = I_{DC} \times R_{YSZ} \tag{2.29}$$

In the working electrode (WE), the electrochemical potential of oxygen is also defined by the electrochemical potentials of oxygen ions and electrons respectively. As the electrochemical potentials of oxygen ions of working and counter electrode differ by the electrolyte loss $\Delta\tilde{\mu}(O^{2-})$, the difference in the electrochemical potentials of oxygen of both electrodes is lower than the electronic electrochemical potential difference, see equation 2.30. This difference in electrochemical potential of oxygen can also be expressed as a fraction of the applied voltage, referred to as electrode overpotential $\eta$, according to equation 2.31.

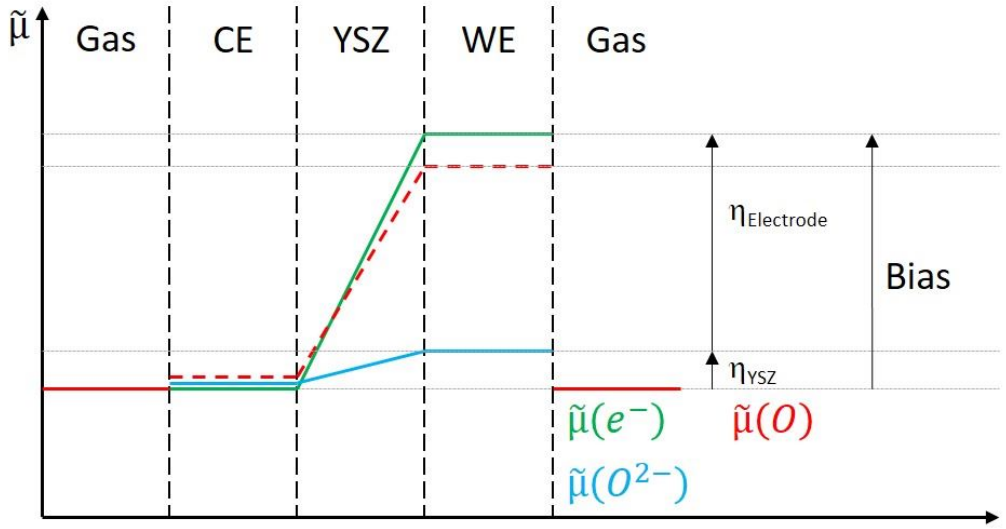


Figure 2.5: Electrochemical potentials of oxygen (red), oxygen ions (blue) and electrons (green) in an idealized electrochemical cell.

$$\Delta\tilde{\mu}(O) = \Delta\tilde{\mu}(O^{2-}) - 2 \times \Delta\tilde{\mu}(e^{-}) \tag{2.30}$$

$$\eta = U_{DC} - I_{DC} \times R_{YSZ} \tag{2.31}$$

Therefore, the polarized working electrode is no longer in equilibrium with the oxygen partial pressure of the gas phase. According to Nernst's equation (2.32), the electrode overpotential can be converted into an oxygen partial pressure ratio ($p_1/p_2$). Hence, an equivalent oxygen partial pressure can be defined, see equation 2.33. The defect chemical state of the working electrode is then defined by this equivalent oxygen partial pressure, independent of whether it is governed by the actual atmospheric oxygen partial pressure or the applied bias voltage.

$$\eta = \frac{R \times T}{z \times F} \times ln\left(\frac{p_1}{p_2}\right) \tag{2.32}$$

$$p_{equivalent} = p_{actual} \times e^{-\frac{\eta \times z \times F}{R \times T}} \tag{2.33}$$

## 2.4 Equivalent circuit models

### 2.4.1 Basic model circuit for mixed ionic electronic conducting electrodes

Figure 2.6a shows the basic basic model circuit for mixed ionic electronic conducting electrodes provided by Jamnik and Maier [35], which can be simplified and adapted to LSF. In their model, a three point measurement with a reference electrode in close proximity to the MIEC|YSZ interface is assumed, therefore neglecting ionic transport resistance through the YSZ and the impedance of the counter electrode. For two point measurements the ionic transport resistance

through the electrolyte also contributes to the total impedance. A single resistance $R_{YSZ}$ is therefore introduced.

For microelectrode measurements the impedance of the counter electrode can often be completely neglected, as it is generally much lower compared to the working electrode impedance due the much larger surface area of the counter electrode. In the case of identical working and counter electrodes the corresponding equivalent circuits are also identical and thus cause identical impedance responses. As both electrodes are in series, the total impedance without bias is given by the sum of the impedances of both electrodes.

Assuming high electronic conductivity the electronic transport resistance $r_{eon}$ can be ignored and the electronic rail is short circuited. Furthermore, if the reaction is limited by the surface exchange resistance $R_{Surf}$ as it is in LSF, the ionic transport resistance $r_{ion}$ can be neglected, and the chemical capacitors $c_{Chem}$, being parallel now, can be summed up to a single chemical capacitance $C_{Chem}$. Therefore a simplified equivalent circuit is obtained without any differential elements, see figure 2.6b. In this circuit the surface capacitance $C_{Surf,ion}$ is in parallel to the usually big chemical capacitance $C_{Chem}$ and thus is not visible in impedance spectra. $R_{LSF|YSZ}$ is the interface resistance and $C_{LSF|YSZ}$ is the interface capacitance.

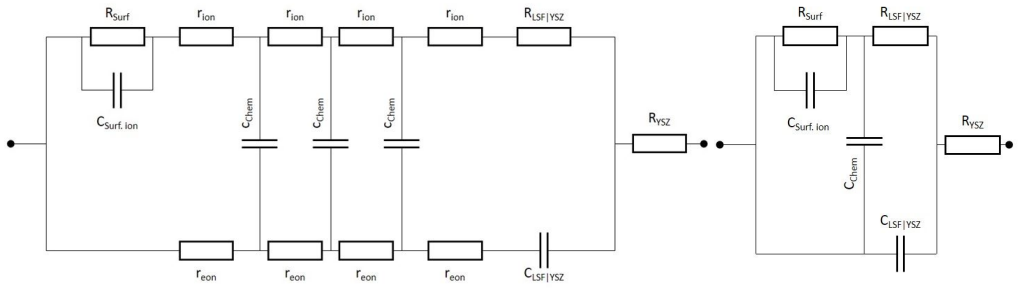


(a) General transmission line (b) Simplified circuit

Figure 2.6: General transmission line according to [35] with additional electrolyte resistance, and a simplified equivalent circuit assuming high electronic and ionic conductivity and oxygen surface exchange as limiting step.

## 2.4.2 Position of current collector

If an additional current collector is used to guarantee high electronic conductivity, the simple equivalent circuit in figure 2.6 has to be adapted. Two different 2-dimensional circuits are obtained depending on whether the current collector is placed above or below the working electrode, as shown in figure 2.7a and 2.7b according to [36].

### Current collector above the electrode - Top geometry

**Oxidizing conditions** In oxidizing conditions, the electronic transport resistance $r_{eon}$ is low and can thus be neglected. Furthermore, the interfacial resistance $R_{YSZ|LSF}$ is neglected as it is small compared to the surface exchange resistance $R_{Surf}$. The chemical capacitances $C_{Chem}$ and the interfacial capacitance $C_{YSZ|LSF}$ are then in parallel, and thus can be summarized by a

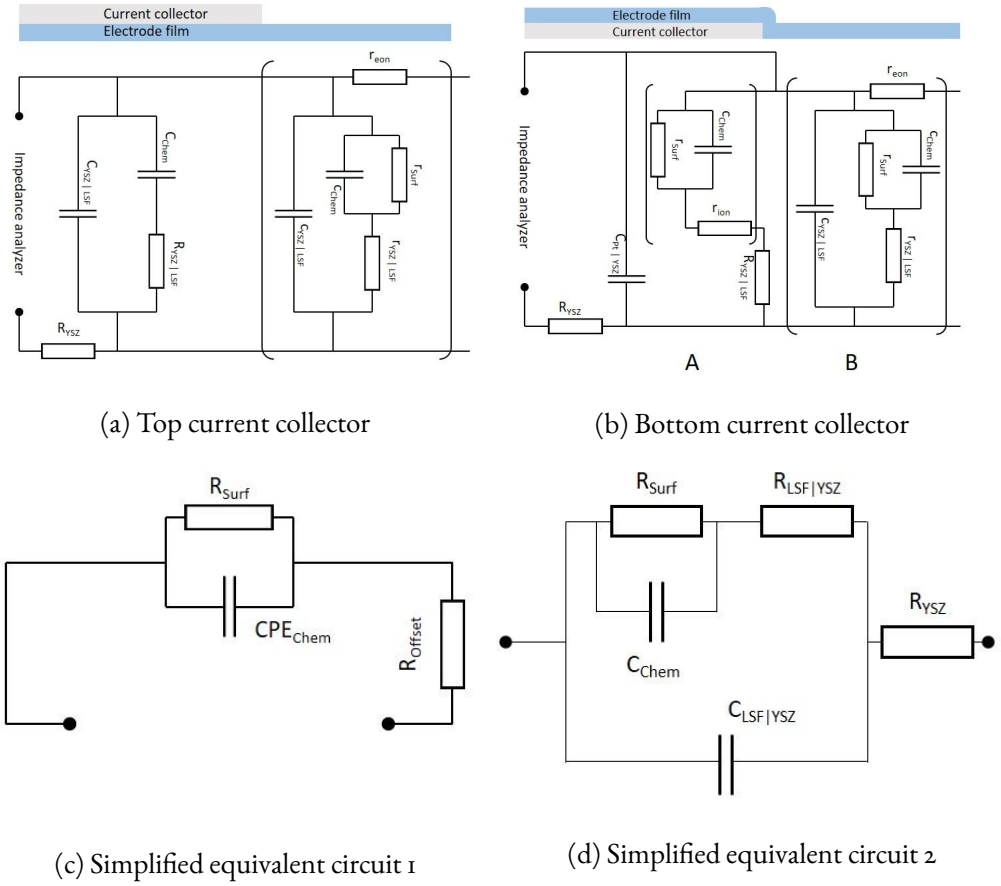


(a) Top current collector

(b) Bottom current collector

(c) Simplified equivalent circuit 1

(d) Simplified equivalent circuit 2

Figure 2.7: Equivalent circuits for MIEC electrodes, according to [36], for current collectors above or beneath the electrode film. General circuits (2.7a and 2.7b), and simplified circuits (2.7c and 2.7d).

single capacitance, which is dominated by the large chemical capacitance of the entire electrode volume. The surface exchange resistance is then in parallel to the chemical capacitance and thus a simplified circuit can be obtained, see figure 2.7c

Reducing conditions In reducing conditions, the electronic transport resistance $R_{eon}$ is high. This causes a complex transmission line which results in a Warburg type slope feature in the intermediate frequency range, see figure 2.8. The low frequency domain however is dominated by the chemical capacitance $C_{Chem}$ in parallel to the surface exchange resistance $R_{Surf}$. Thus, the simple equivalent circuit, figure 2.7c can be used to describe large parts of the low frequency semicircle.

Current collector below the electrode - Bottom geometry

Oxidizing conditions In oxidizing conditions the lateral ionic transport resistance $R_{ion}$ is high compared to the surface resistance $R_{Surf}$. Therefore, the left branch (A) is blocked by this resistance and doesn't contribute to surface exchange and chemical capacitance. Furthermore, the

electronic conductivity in oxidizing conditions is again high and can therefore be neglected in the right branch (B). The circuit can then be simplified, see figure 2.7d.

Reducing conditions In reducing conditions, the lateral ionic transport resistance is low. Therefore both branches (A and B) contribute to surface exchange and chemical capacitance. The low electronic conductivity again causes a Warburg type slope feature in the impedance spectrum, while the low frequency domain is again dominated by the surface exchange resistance in parallel to the chemical capacitance. Thus, the equivalent circuit shown in figure 2.7c can again be used to describe the low frequency semicircle.

Figure 2.8 shows simulated spectra for the right branch (B) of figure 2.7a and 2.7b respectively. As can be seen, if the surface resistance is sufficiently high compared to the electronic transport resistance, the transmission line results in a semicircle. Lower ratios of surface exchange resistance to electronic transport resistance cause a slope feature.

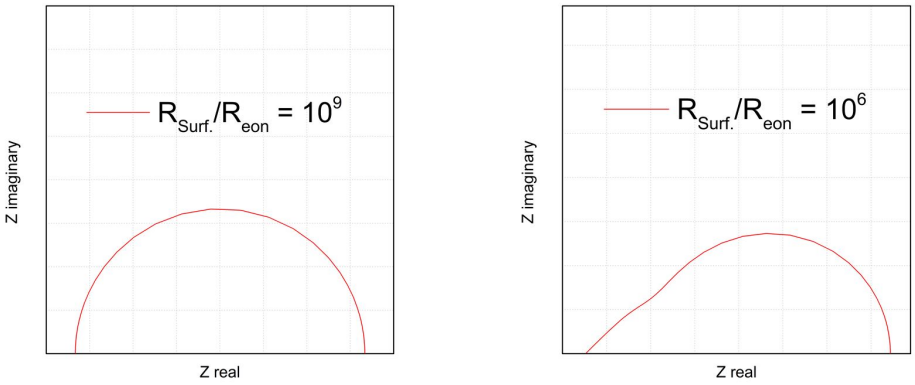


(a) High electronic conductivity (b) Low electronic conductivity

Figure 2.8: Simulated spectra for the right branch of the circuits shown in figure 2.7. Simulation is done with 1000 repetitions of the element in brackets, with different ratios of surface exchange resistance to electronic transport resistance. Interfacial resistances and capacitances are neglected.

# 3 Experimental

## 3.1 Sample preparation

### 3.1.1 Degradation experiments

Different electrode geometries were investigated, to determine the optimal geometry with regards to the stability of the surface resistance. Symmetrical square 5 mm × 5 mm thin film macroelectrodes and circular microelectrodes with a diameter of 200 µm were tested. To minimize the sheet resistance, current collector grids were deposited either on top of or below the electrode films. Figure 3.1 shows a sketch of the tested sample geometries.

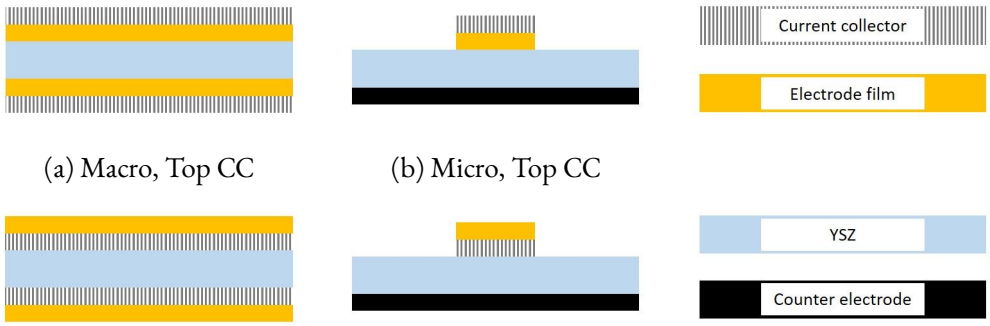


(a) Macro, Top CC (b) Micro, Top CC

(c) Macro, Bottom CC (d) Micro, Bottom CC

Figure 3.1: Schematics of different electrode geometries used for impedance measurements.

LSF thin film electrodes of 200 nm thickness were prepared by pulsed laser deposition. Films were deposited on YSZ (100) single crystals (9.5 mol% $Y_2O_3$ , Crystec Germany) of 5 mm side length and 0.5 mm thickness, polished on either one side for microelectrodes or both sides for macroelectrodes, either onto the YSZ substrate or onto a predeposited current collector grid. A target prepared from LSF powder (Sigma Aldrich) by cold isostatic pressing (150 MPa) and sintering (12 h, 1200 °C) was used for ablation by a KrF excimer laser (Complex Pro 201F). Table 3.1 shows the parameters used for deposition.

Platinum grids with a height of 100 nm, a strip width of 15 µm and a mesh size of 35 µm were used as current collectors. They were produced via lift-off photolithography and magnetron sputtering. To improve bonding between the substrate and the platinum grid, a titanium layer of 5 nm thickness was deposited. For lithography, the sample was coated with a photoresist (N-1430 MicroResist Technology, Germany) by a spin-coater (SCC-200 KLM, Germany), dried

| PLD parameters | |
|---|---|
| laser wave length | 248 nm |
| deposition time | 30 min |
| laser energy per pulse | 400 mJ |
| pulse frequency | 5 Hz |
| depostition temperature | 600 °C |
| oxygen partial pressure | $4 \times 10^{-2}$ mbar |
| target distance | 6 cm |

Table 3.1: Paramteres used for deposition the electrode films.

and the polymer was cross linked by UV exposure (350W, USHIO 350DP Hg,Ushio, Japan). Developing of the structures was done by bathing the sample in developer solution (MicroResist Technology, Germany). The current collectors were deposited either onto the electrode film (top geometry) or onto the YSZ substrate (bottom geometry). A MED 020 Coating System machine (BAL-TEC Germany) was used for deposition. The parameters for photolithography and sputtering are shown in table 3.2.

| Photolithography | | Sputtering | | |
|---|---|---|---|---|
| photoresist | 100 µl | | Titanium | Platinum |
| spincoater speed | 100 rpm | sputter time | 27 s | 125 s |
| prebaking | 2 min at 100 °C | argon pressure | $7 \times 10^{-3}$ mbar | $2 \times 10^{-2}$ mbar |
| developing time | 40 to 60 s | sputter current | 100 mA | 100 mA |
| exposure time | 60 to 90 s | target distance | 6 cm | 6 cm |

Table 3.2: Parameters used in the application of the current collector grids.

Structuring of the microelectrodes was done via photolithography and consecutive ion beam etching (tectra GmbH, ionEtch Sputter Gun). For both, top and bottom current collectors, these steps were done after deposition of the electrode films and current collectors. Parameters for these steps are shown in table 3.3.

| Photolithography | | Ion beam etching | |
|---|---|---|---|
| photoresist | 2 times 100 µL | etching time | 20 to 25 min |
| spincoater speed | 70 rpm | argon pressure | $9.8 \times 10^{-5}$ to $1.2 \times 10^{-4}$ mbar |
| spincoater time | 30 s | plasma current | 1.8 to 2.3 mA |
| exposure time | 60 s | beam voltage | 3 kV |
| developing time | 50 s | extractor voltage | 2 kV |
| prebaking | 2 min at 100 °C | magnetron current | 25 mA |

Table 3.3: Parameters used for microstructuring

As counter electrodes, porous platinum electrodes were prepared by brushing platinum paste. To minimize high temperature exposure of the electrode film, the platinum paste was only dried at 130 °C for about 5 min.

### 3.1.2 First set of bias experiments

Samples for the first set of bias experiments were prepared as described above (section 3.1.1), but a finer current collector grid of 10 µm mesh width and strip width was used. This was done to minimize the sheet resistance, and thus to ensure that the entire LSF film is polarized.

### 3.1.3 Counter electrodes

After the first set of bias experiments, new counter electrodes had to be investigated, see chapter 3.2.4. Three different types of electrodes were considered: dried porous platinum electrodes, annealed porous platinum electrodes and porous combined LSF/platinum electrodes. Platinum electrodes were prepared by brushing platinum paste on a 5 mm × 5 mm, both side polished YSZ substrate, and either dried at 130 °C for several minutes or annealed at 850 °C for 2 h. The combined Pt/LSF electrode was prepared by brushing LSF paste onto the YSZ substrate, drying it at 130 °C, followed by brushing a layer of platinum paste and annealing at 850 °C for 2 h.

### 3.1.4 Second set of bias experiments

For the second set of bias experiments counter electrodes of porous LSF/Pt were used. The counter electrode was prepared first, by brushing LSF paste and Pt paste onto a YSZ crystal, and annealing at 850 °C for 2 h. Subsequently the current collector grid was sputtered on the free YSZ surface on the back side using the parameters in table 3.2. Then the electrode film was deposited on top of the current collector, see table 3.1, and microstructured, see table 3.3.

### 3.1.5 Investigation of the surface resistance

Since for the second set of bias experiments unexpectedly high surface resistances were found in oxidizing atmospheres, various samples were prepared by different routes to determine the detrimental preparation step. The following types of samples were prepared:

- Microelectrodes without current collector: Preparation of counter electrodes (section 3.1.4), followed by deposition of the LSF film (table 3.1) and microstructuring (table 3.3).
- Macroelectrodes with bottom current collector: Preparation of current collector grids by lift-off lithography (table 3.2), followed by deposition of the electrode films (table 3.1).
- Macroelectrodes with bottom current collector: Preparation of current collector grids by sputter deposition (table 3.2) and ion beam etching (table 3.3), followed by deposition of the electrode films (table 3.1).
- Macroelectrodes with top current collector: Deposition of the electrode films (table 3.1), followed by application of the current collector grids via lift-off lithography (table 3.2).
- Microelectrodes with thin film counter electrode: Preparation of the current collector grid by lift-off lithography (table 3.2) followed by deposition of the electrode film (table 3.1) and structuring of microelectrodes and counterelectrode from the same electrode film (table 3.3).

- Microelectrodes from measured macroelectrodes: Preparation of macroelectrodes with bottom current collector by lift-off lithography (table 3.2) or ion beam etching (table 3.3), followed by microstructuring (table 3.3).

### 3.1.6 3-point measurements

Samples for 3 point measurements were prepared on 5 mm × 5 mm × 1 mm slabs of YSZ (100) which had a notch carved around their circumference. Platinum paste was brushed into this notch and annealed at 850 °C for two hours. Then the current collector grids were prepared on both sides by lift-off photolithography and sputtering, see table 3.2. Finally 200 nm of LSF were deposited on both sides by PLD, see table 3.1.

## 3.2 Impedance spectroscopy

### 3.2.1 Description of the measuring apparatus

The measuring setup consists of two parts, a measuring apparatus on which the sample was mounted and contacted (see figure 3.2) and a tube furnace. The measuring apparatus consists of the following elements:

- A plank of fused silica (A) was used as base.
- The counter electrode (B) consisted of a sheet of platinum, folded tightly around the tip of the base.
- Pt wires(C) in a housing of fused silica.
- A type K thermocouple (D) mounted in a fused silica housing.
- A platinum needle (E) was used to contact the working electrode. The needle was attached to the tip of a fused silica cantilever, which also served as housing for the electrical wiring.
- The base was mounted onto a stainless steel flange (F)
- Gas inlet and outlet (G)
- Feedthroughs for the electrical and thermocouple wires (H)
- A fused silica tube was inserted into a tube furnace, which was mounted on guide rails.

Samples were contacted using the following procedure:

- The tube furnace was moved to the right, to give access to the counter electrode.
- The sample was placed with the counter electrode face down on the platinum sheet (B).
- The contacting needle was positioned onto a microelectrode of the sample

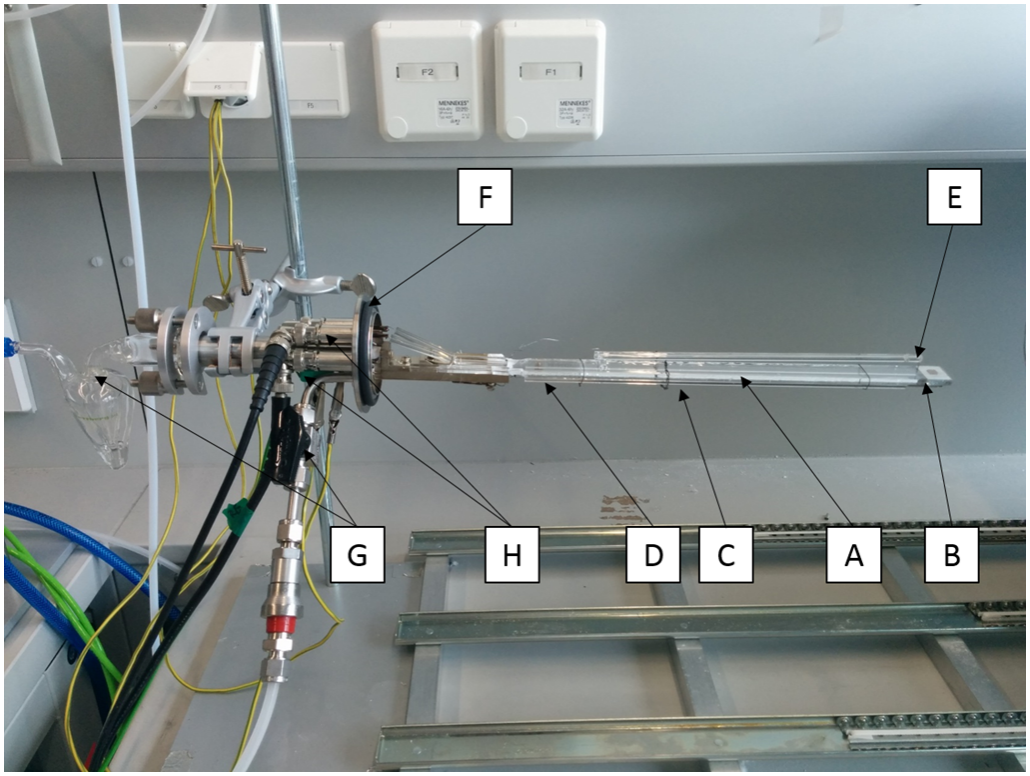


(a) Measuring apparatus, open

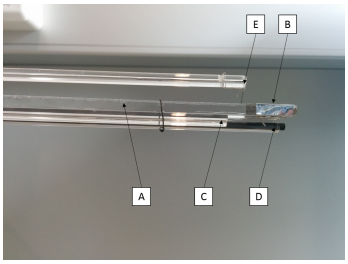


(b) cantilever tip, side view

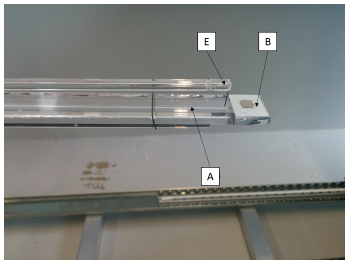


(c) cantilever tip, top view

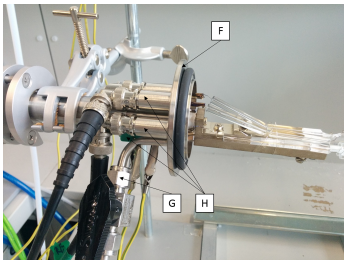


(d) flange with feedthroughs

Figure 3.2: Measuring apparatus used in the impedance spectroscopy measurements. A) fused silica base, B) platinum sheet, C) electrical wiring, D) thermocouple, E) needle mounted on cantilever for contacting the working electrode, F) flange, G) gas in- and outlet, H) feedthroughs for thermocouple and electrical contacts

- The tube furnace was moved very gently back over the fused silica cantilever to prevent the needle from slipping off and decontacting.
- The fused silica tube was then fixated on the flange.
- The sealed apparatus was purged with the desired gas mixture for at least 30 min.
- The oven was heated to measuring temperature.

### 3.2.2 Degradation experiments

The prepared samples were measured with impedance spectroscopy, using an Novocontrol Alpha A High Performance Frequency Analyzer, in the setup described above. The samples were mounted on a sheet of platinum, thus contacting the counter electrode. The working electrode was contacted using a platinum tip.

Measurements were carried out either in synthetic air or in humidified hydrogen. The humidified hydrogen was provided by letting a mixture of 2.5 % $H_2$ in Argon bubble through distilled water at room temperature, to ensure saturation with water. This corresponds to an effective oxygen partial pressure of about $9.5 \times 10^{-24}$ bar at measuring conditions, see section 3.2.8. Measurements were carried out at 600 °C for about 16 to 18 h per sample.

The samples were mounted in the cold apparatus, which was then sealed and purged with the respective gas mixture for at least 30 min. The oven was heated to the measuring temperature of 600 °C. This way, reactions between the samples and possible contamination in the lab air at elevated temperatures were eliminated.

Measurements were taken in a frequency range of 1 MHz to 10 mHz with 5 points per decade, going to lower frequencies when necessary, and a voltage of 10 mV was used. Each frequency was measured for either one second or one period, which corresponds to about one spectrum every three minutes.

### 3.2.3 First set of bias experiments

In the first set of bias experiments a similar sample mounting procedure was used. Measurements were done at 625 °C in synthetic air and humidified hydrogen. At the start of the measurements a couple of bias free spectra were measured, to estimate the initial state and degradation behavior of the samples. Bias was applied stepwise in 25 mV and 50 mV steps, up to the maximum bias, and thereafter lowered back to 0 V bias in the same way.

In humidified hydrogen, experiments with maximum bias voltages of up to 1200 mV cathodic and anodic bias were done. In synthetic air experiments were done with up to 500 mV cathodic and anodic bias. At each bias level two spectra were recorded. After each second bias step, two bias free spectra were measured, to observe irreversible changes in the sample caused by the applied bias.

### 3.2.4 Counter electrodes

For investigation of suitable counter electrode materials samples were mounted and measured by EIS as described above, at a temperature of 625 °C with varying oxygen partial pressures from

1000 to 0.25 mbar.

### 3.2.5 Second set of bias experiments

In the second set of bias experiments a similar procedure of sample mounting was used. Measurements were again done at 625 °C in humidified hydrogen, synthetic air and different mixtures of oxygen and nitrogen. Bias was applied stepwise as described in section 3.2.3. In humid hydrogen maximum bias voltages of ±1200 mV were used in anodic and cathodic direction, in oxidizing conditions cathodic bias of up to −1200 mV was used. For the different mixtures of oxygen and nitrogen cathodic bias of up to −500 mV was used.

### 3.2.6 Investigations on the high surface resistance

Since the samples in the second set of bias measurements showed unexpectedly high surface resistances in oxidizing atmospheres, measurement parameters were varied to ascertain the origin of this effect. The following sample preparation and measurement parameters were considered as causative:

- Target used in the PLD deposition
- Presence of a current collector grid
- Placement of the current collector grid
- Influences from the counter electrode
- Microstructuring process
- Measurement apparatus

To determine the crucial parameter a multitude of samples with different parameters regarding measurement and preparation condition was prepared, as described in section 3.1.5. Measurements were done in synthetic air at 625 °C. No bias was applied since these measurements only served to determine the crucial step that lead to the unexpectedly high surface resistances encountered in the second set of bias experiments.

### 3.2.7 3-point measurements

For three point measurements samples were clamped between to sheets of platinum to contact working and counter electrode. The reference electrode was contacted with a noose of fine platinum thread around the circumference of the sample chip. The impedance analyzer was connected in 4-point mode, as sketched in figure 3.3. Measurements were done in different oxygen/nitrogen mixtures at 625 °C.

Bias voltages of −600 to 600 mV were applied between counter and working electrode, which corresponds to overpotentials of about ±300 mV at each electrode side. In the first experiment, working and counter electrode were measured both against the reference electrode and against each other to detect possible parasitic currents paths. In later experiments only one electrode was measured against the reference electrode.

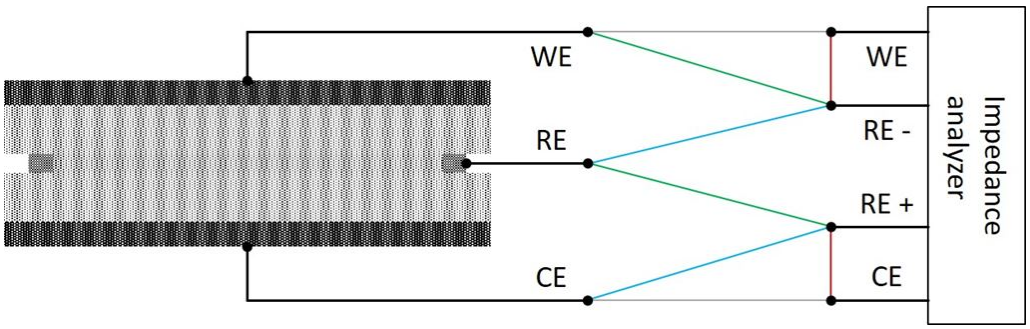


Figure 3.3: Sketch of sample contacting used for three point measurements. The gray lines are connected in all three modes, colors represent different measurement modes "working electrode versus reference electrode" (green), "counter electrode versus reference electrodes" (blue) and "working electrode versus counter electrode" (red).

### 3.2.8 Calculation of the oxygen partial pressure in humidified hydrogen

Humidified hydrogen was used as reducing atmosphere during EIS experiments. In order to achieve saturation with water, a mixture of 2.5 % hydrogen in argon was bubbled through water. At laboratory temperatures of 21 °C the vapor pressure of water is about 25 mbar [37], therefore the resulting gas mixture consists of roughly 25 mbar hydrogen ($p_0(H_2)$), 25 mbar water ($p_0(H_2O)$) and 963 mbar argon, with a total pressure P of about 1013 mbar. At measurement temperature of 625 °C this defines an oxygen partial pressure according to the oxyhydrogen equilibrium and the corresponding mass action law, see equations 3.1 and 3.2.

$$H_2 + 1/2\, O_2 \rightleftharpoons H_2O \tag{3.1}$$

$$K = \frac{p(H_2O) \times \sqrt{P}}{p(H_2) \times \sqrt{p(O_2)}} \tag{3.2}$$

Based on thermodynamic data from [37], the equilibrium constant at 625 °C was calculated according to equation 3.3.

$$K = e^{-\frac{\Delta_r G^0}{R \times T}} \tag{3.3}$$

Since for every mole of oxygen two moles of hydrogen are formed and two moles of water are consumed, equations 3.4 and 3.5 apply, where the index zero indicates partial pressures in the initial cold gas mixture.

$$p(H_2) = p_0(H_2) + 2 \times p(O_2) \tag{3.4}$$

$$p(H_2O) = p_0(H_2O) - 2 \times p(O_2) \tag{3.5}$$

Using equations 3.2 to 3.5 the oxygen partial pressure in humidified hydrogen is calculated to $9.5 \times 10^{-24}$ mbar.

# 4 Results

## 4.1 Sample preparation

Using lift-off photolithography and sputtering, well defined platinum grid structures were produced on the electrode film as well as on the YSZ substrate, as shown in figure 4.1. Circular microelectrodes were produced by photolithography and ion beam etching, see figure 4.2.

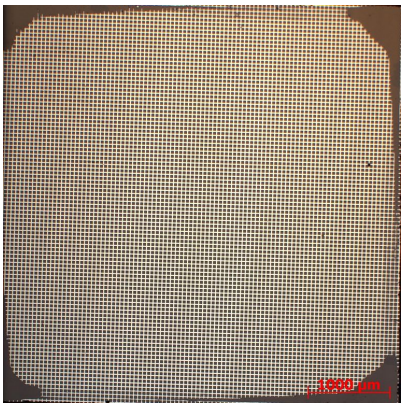

(a) Coarse current collector on LSF

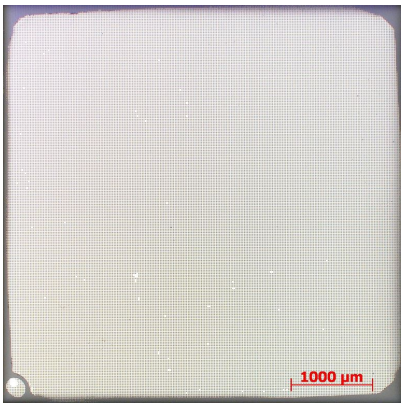


(b) Fine current collector grid on YSZ

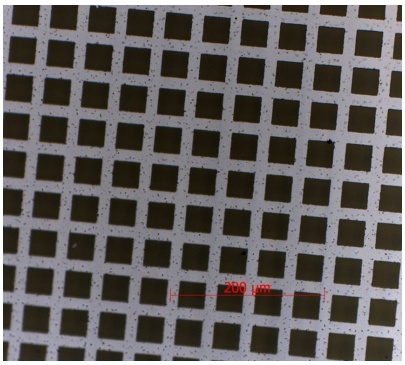


(c) Coarse current collector grid, detail

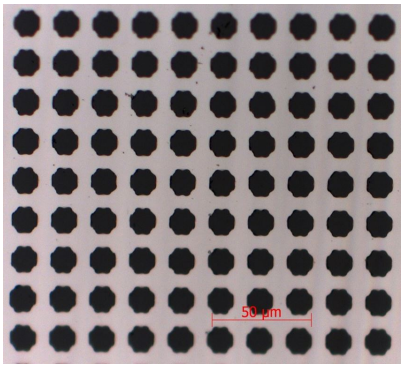


(d) Fine current colelctor grid, detail

Figure 4.1: Current collector grids on YSZ substrate (4.1b and 4.1d) and on the LSF electrode film (4.1a and 4.1c). Grids are 35 µm/35 µm (4.1a and 4.1c) and 10 µm/10 µm (4.1b and 4.1d).

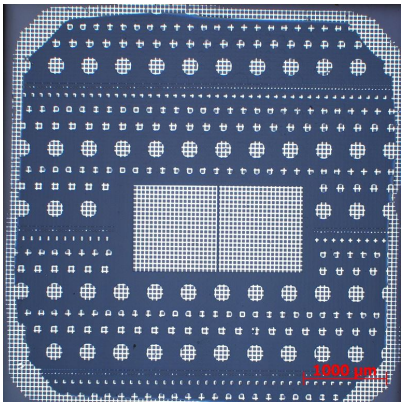


(a) Top current collector

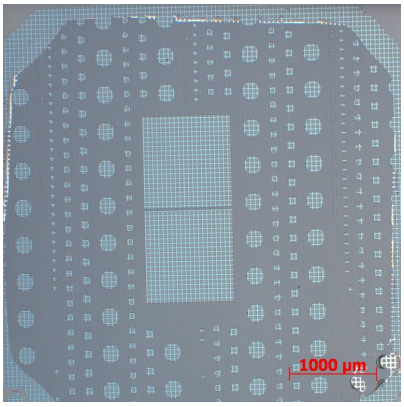


(b) Bottom current collector

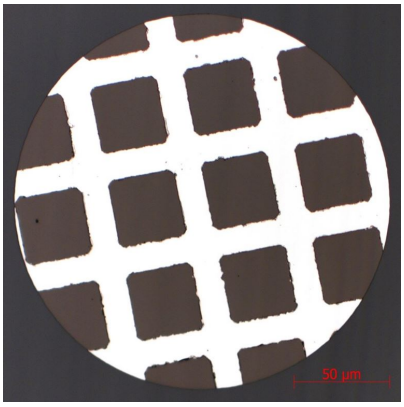


(c) Microelectrode with top current collector

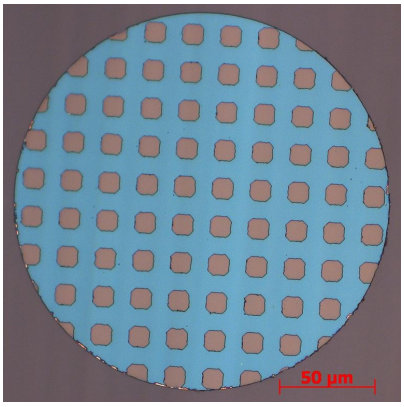


(d) Microelectrode with bottom current collector

Figure 4.2: Microelectrodes with top an bottom current collectors. Grids are 35 µm/35 µm (4.2a, 4.2b and 4.2c) and 10 µm/10 µm (4.2d)

## 4.2 Degradation experiments

### 4.2.1 Measurements in synthetic air

In synthetic air all impedance spectra consisted of an x-axis intercept and a dominant low frequency semicircle, see figure 4.3. Spectra of macroelectrodes showed an additional shoulder in the high frequency region of the semicircle. A simple equivalent circuit consisting of one R||CPE element and resistance in series has been chosen to fit the spectra. This circuit can be deduced from the equivalent circuits described in section 2.4.2, by neglecting contributions from the YSZ|LSF interface and the Pt|LSF interface. Since earlier measurements suggest that they are much smaller than the exchange resistance and the chemical capacitance, features attributed to these elements are only expected in the high frequency region of the spectrum. Deviations from a semicircle in the high frequency range were therefore excluded from the fitting range, only a serial offset resistance was used to cover all high frequency effects. Furthermore the lateral electronic transport resistance can be neglected in oxidizing conditions. Thus a simplified equivalent circuit (figure 4.4) can be used for fitting.

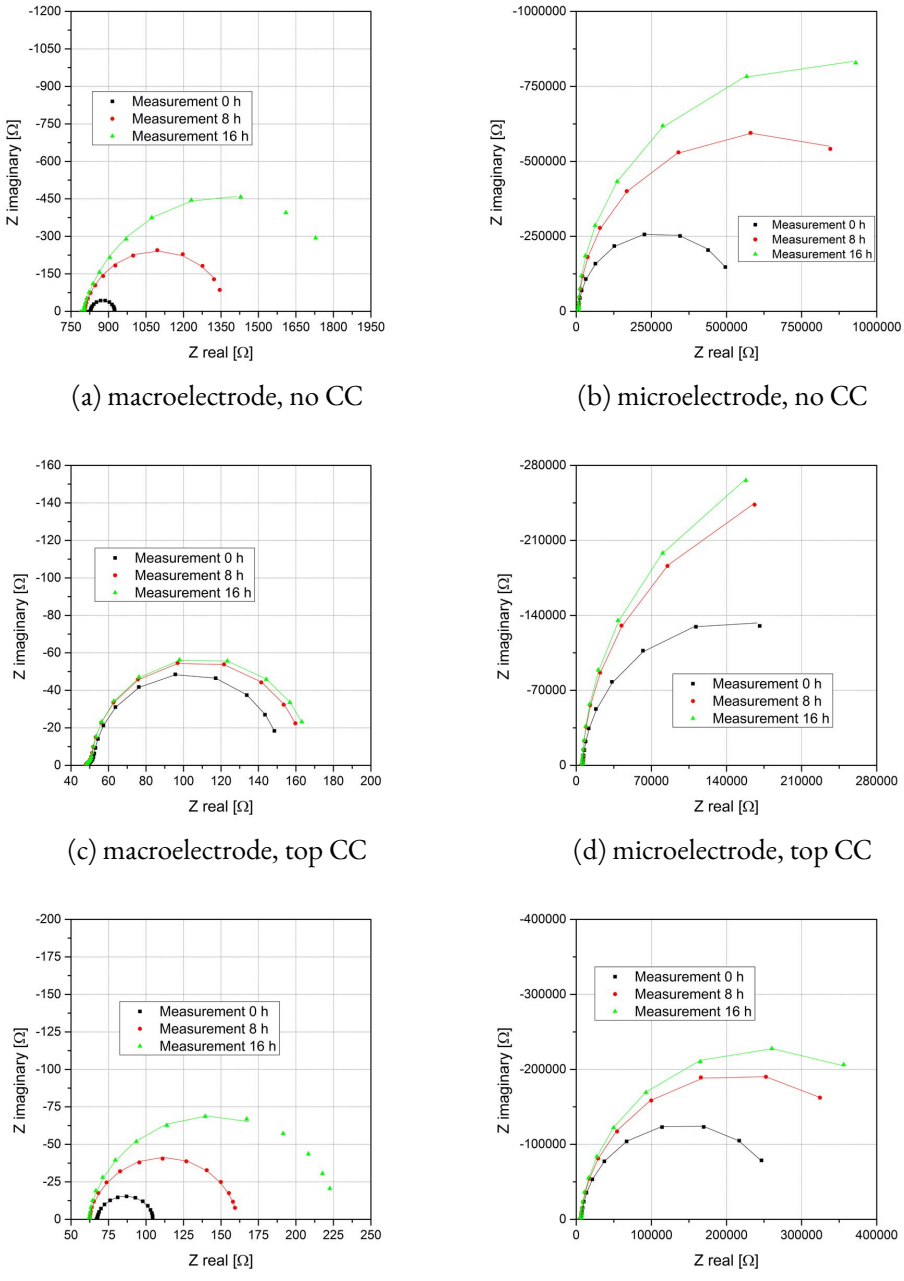


(a) macroelectrode, no CC

(b) microelectrode, no CC

(c) macroelectrode, top CC

(d) microelectrode, top CC

(e) macroelectrode, bottom CC

(f) microelectrode, bottom CC

Figure 4.3: Impedance spectra of different electrode geometries and current collector placement, measured in synthetic air. Each figure shows the initial spectrum as well as spectra after 8 and after 16 h of degradation. Data points represent measured values and the solid line the corresponding fit according to figure 4.4. Measurements were done at 600 °C.

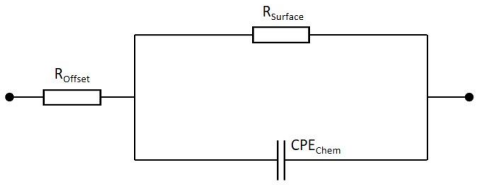


Figure 4.4: Equivalent circuit used to fit impedance spectra.

### 4.2.2 Measurements in humidified hydrogen

In reducing atmosphere, the impedance also showed an x-axis offset and a dominant semicircle. For samples with bottom current collectors an additional slope of approximately 45° at the high frequency onset of the semicircle was visible, see figure 4.5. This slope is most likely caused by a complex in plane transmission line, due to an increased electronic transport resistance in reducing conditions [26]. However, spectra were again fitted using the equivalent circuit shown in figure 4.4. Accordingly, also the in plane electronic transport resistance is neglected, as the feature of interest is the dominant semicircle, interpreted as the surface exchange resistance in parallel to the chemical capacitance. Hence, fitting was done in the low frequency range of the semicircle, while the slope feature was excluded. Therefore the offset resistance is not only caused by the electrolyte resistance and some interfacial effects but also accounts for the electronic transport resistance.

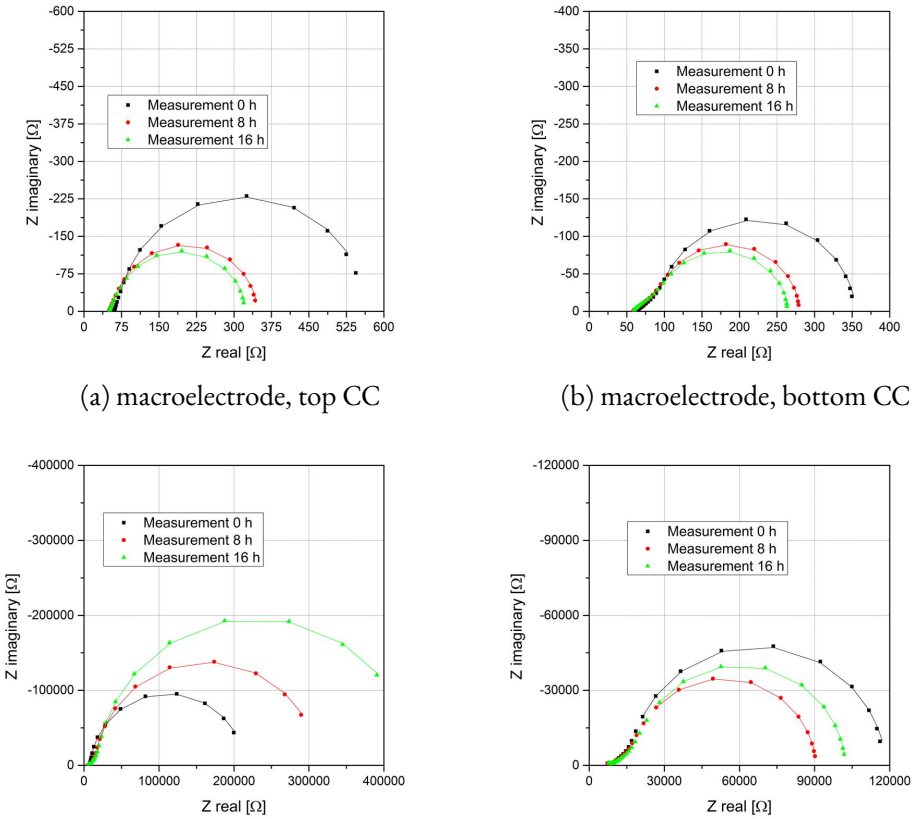


(a) macroelectrode, top CC

(b) macroelectrode, bottom CC

(c) microelectrode, top CC

(d) microelectrode, bottom CC

Figure 4.5: Impedance spectra of different electrode geometries and current collector placement, measured in humidified hydrogen. Each figure shows the initial spectrum as well as spectra after 8 and after 16 h of degradation. Data points represent measured values and the solid line the corresponding fit according to figure 4.4. Measurements were done at 600 °C.

### 4.2.3 Comparison of electrode geometries

To compare different electrode geometries, surface resistance and chemical capacitance were normalized to the active electrode surface and the active electrode bulk volume respectively, see equations 4.1 and 4.2 for macroelectrodes and equations 4.3 and 4.4 for microelectrodes. Here $d$ is the electrode diameter, $\mathcal{A}$ is the electrode area and $h$ the film thickness. For top current collector geometry, part of the area is blocked by the dense platinum grid and thus cannot take part in the oxygen exchange reaction, thus an active area factor $f_A$ of 0.49 was used for the surface resistance. However, the electrode volume beneath the current collector still contributes to the chemical capacitance, thus an active volume factor $f_V$ of 1 was used.

For bottom current collector geometry there is a difference between oxidizing and reducing atmosphere. In oxidizing atmosphere the high resistance of the lateral ion transport prevents the area above the current collector grid from being polarized, thus $f_A$ and $f_V$ are 0.49. In reducing atmospheres, the ionic transport resistance decreases accordingly as the concentration of oxygen vacancies increases [26] and the areas above the current collector thus contribute to surface exchange and chemical capacitance, therefore $f_A$ and $f_V$ are 1. Figure 4.6 and table 4.1 show the progressions of surface resistance and chemical capacitance thus obtained.

$$R_{SurfaceExchange} = R_{Surface} \times \mathcal{A} \times f_A \tag{4.1}$$

$$C_{Chem} = \left(T \times R_{Surface}^{(1-P)}\right)^{\frac{1}{P}} \times \frac{2}{\mathcal{A} \times h} \times f_V \tag{4.2}$$

$$R_{SurfaceExchange} = R_{Surface} \times \frac{d^2 \times \pi}{4} \times f_A \tag{4.3}$$

$$C_{Chem} = \left(T \times R_{Surface}^{(1-P)}\right)^{\frac{1}{P}} \times \frac{4}{d^2 \times \pi \times h} \times f_V \tag{4.4}$$

In synthetic air, the initial values of the surface resistance are lower for macroelectrodes. The surface resistance increases significantly over time. This effect is most visible for samples without current collector but is not clearly correlated to any electrode geometry or current collector placement. The chemical capacitance is also quite independent of the current collector placement and is slightly lower for microelectrodes. The samples without current collector show significantly lower chemical capacities and higher surface resistances, which indicates that only a part of the electrode is polarized because of the sheet resistance within the electrode. This is consistent with the offset resistance being much higher than expected for those samples. Based on the known ionic conductivity of YSZ values of about 5000 Ω are expected for microelectrodes of 200 µm diameter at 600 °C. [38] In humidified hydrogen the surface resistance shows higher initial values for macroelectrodes and similar initial values for microelectrodes compared to synthetic air. With exception of the microelectrode with top current collector, the surface resistance decreases over time.

Considering these data, microelectrodes with bottom current collector grids were chosen for consecutive experiments, as they showed more stable surface resistances than top current collectors. Moreover microelectrodes provide the advantage, that the counter electrode can be com-

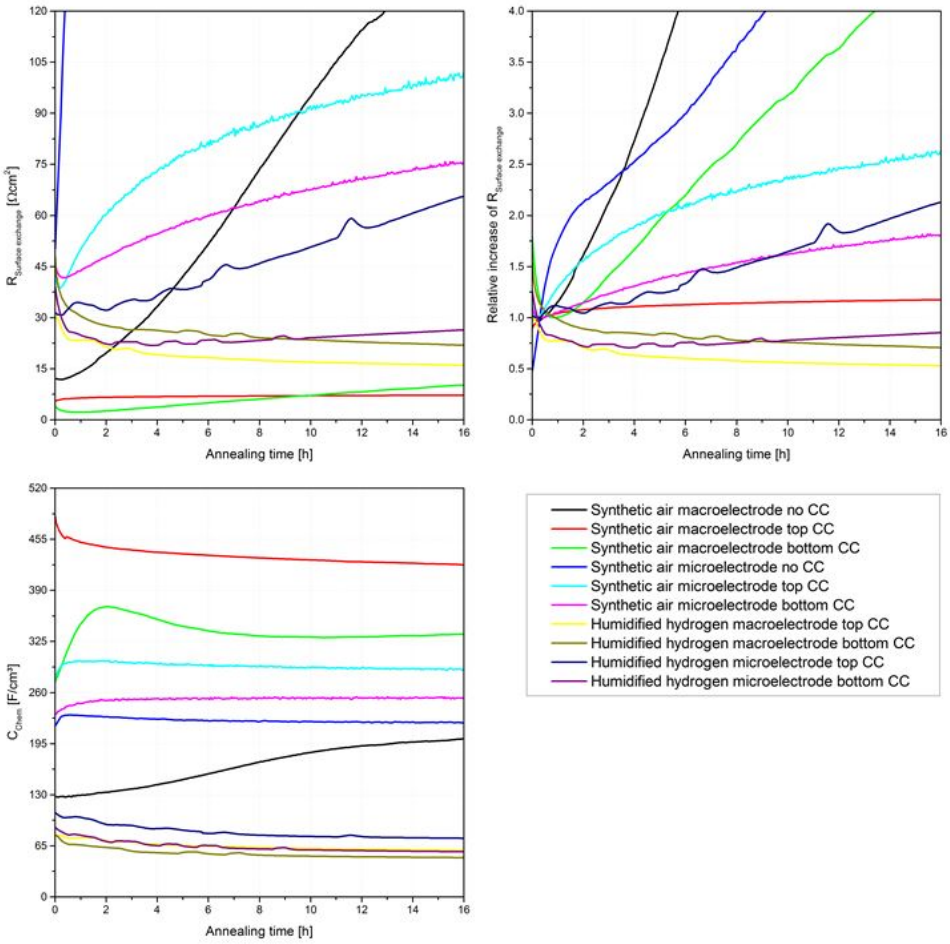


Figure 4.6: Progression of the surface resistance and chemical capacitance of different electrode geometries over 16 h of degradation at 600 °C. The small peaks present on some lines are caused by temperature fluctuations.

| Parameters | | | Surface resistance | | | Chemical capacitance | |
|---|---|---|---|---|---|---|---|
| Size | CC | Atm. | Start $\Omega\,cm^2$ | After 16 h $\Omega\,cm^2$ | Rel. Increase | Start $F\,cm^{-3}$ | After 16 h $F\,cm^{-3}$ |
| Macro | None | S. air | 12 | 146 | 12 | 128 | 201 |
| Macro | Top | S. air | 6.1 | 7.2 | 1.2 | 457 | 422 |
| Macro | Bottom | S. air | 2.3 | 10 | 7.7 | 342 | 334 |
| Micro | None | S. air | 105 | 545 | 5 | 230 | 221 |
| Micro | Top | S. air | 39 | 102 | 2.6 | 290 | 290 |
| Micro | Bottom | S. air | 42 | 76 | 1.8 | 243 | 253 |
| Macro | Top | $H_2/H_2O$ | 30 | 16 | -0.5 | 78 | 59 |
| Macro | Bottom | $H_2/H_2O$ | 31 | 22 | -0.7 | 66 | 50 |
| Micro | Top | $H_2/H_2O$ | 31 | 66 | 2.1 | 103 | 75 |
| Micro | Bottom | $H_2/H_2O$ | 31 | 26 | -0.8 | 84 | 57 |

Table 4.1: Surface exchange resistance and chemical capacitance of different electrode geometries (5 mm × 5 mm macroelectrodes, or circular microelectrodes of 200 µm diameter), different positions of the current collector grid (no current collector, above the electrode film (top) or below the electrode film (bottom) and different atmospheres (synthetic air or humidified hydrogen), measured at 600 °C.

pletely neglected as it has a much smaller impedance than the microelectrode and the electrolyte. Finally, the placement of the current collector below the electrode film rules out catalytic activity from the platinum.

## 4.3 First set of bias experiments

### 4.3.1 Measurements in reducing atmosphere

#### Cathodic Polarization

Cathodic bias experiments were done with bias cycles of up to −500 mV in steps of 25 mV and up to −1200 mV in steps of 50 mV. Figures 4.7 and 4.8 show corresponding spectra. At low bias voltages spectra showed a high frequency offset and a low frequency semicircle, with an additional slope feature in the high frequency onset of the semicircle.

The first notable feature is the offset resistance being about 15 000 Ω (for experiments with up to −500 mV bias) and 11 000 Ω (for experiments with up to −1200 mV bias), contrary to an expected offset resistance of about 5000 Ω based on the known ionic conductivity of YSZ [38]. Comparison of chemical capacitances with previous results from the degradation experiments (see section 4.2.2) also show values lower than the expected value of about 60 F/cm³. One possible explanation is a displacement of the contacting needle onto a neighboring smaller microelectrode due to vibrations during the sealing of the tube. When normalizing the chemical capacitance and the offset resistance to smaller electrodes (100 µm and 80 µm for measurements with up to −500 mV bias and up to −1200 mV bias respectively, both chemical capacitance and offset resistance match expectations, thereby supporting this assumption. Microscopic images

yielded visual confirmation, since marks from the contacting needle were found on electrodes with 100 µm and 80 µm respectively.

With increasing polarization, the high frequency slope feature changes into a distinguishable semicircle, which upon further increase of bias gets more and more pronounced, while staying roughly the same size. If this slope feature originates from a low electronic conductivity as suggested by Kogler et al. [26], it is then most reasonable for it to disappear under cathodic bias. As with cathodic polarization the concentration of electronic charge carriers increases, a decrease of the electronic transport resistance can be assumed. Furthermore, if the electronic transport resistance decreases, other features of similar peak frequency originating from the interface might become visible. This was indeed observed, as with increasing cathodic bias, a second small semicircle became visible.

The low frequency semicircle decreases significantly in size upon polarization, which fits expectations as nonlinear current voltage characteristics are assumed. This vast decrease down to about 5000 to 10 000 Ω can be potentially disadvantageous as the impedance of the counter electrode might influence the impedance spectra. A more detailed investigation on counter electrodes is given in section 4.4.

For bias voltages up to −500 mV spectra were fitted using an equivalent circuit consisting of a resistance, followed by one R||CPE element, while limiting the fit range to the low frequency semicircle, see figure 4.9a. For higher bias voltages,the entire spectrum was fitted using the equivalent circuit shown in figure 4.9b. The surface resistance was normalized to an electrode of 100 µm and 80 µm diameter respectively using equation 4.3 with an active area factor $f_A$ of 1. Since part of the applied bias is lost at the electrolyte, at the interface or through electronic transport, the effective overpotential at the electrode surface has been calculated according to equations 4.5 and 4.6 respectively.

$$\eta = U_{\mathrm{DC}} - I_{\mathrm{DC}} \times R_{\mathrm{Offset}} \tag{4.5}$$

$$\eta = U_{\mathrm{DC}} - I_{\mathrm{DC}} \times \left(R_{\mathrm{YSZ}} + R_{\mathrm{YSZ|LSF}}\right) \tag{4.6}$$

The values thus obtained for surface exchange resistance and effective electrode overpotential are shown in the following figure 4.10. The initial surface exchange resistance at 625 °C, about 10 Ω cm$^2$, is lower than in the degradation experiments, see section 4.2.2, by a factor of three. This is at least partly because the temperature was 25 °C lower in the degradation experiments. In both bias experiments degradation of the oxygen exchange kinetics was observed on the bias free spectra, whereby with polarization of up to −1200 mV these effects were far more pronounced. As such negative potentials are beyond the thermochemical stability range of LSF (approximately $1 \times 10^{-27}$ bar oxygen partial pressure, [17]), irreversible effects are realistic. Furthermore a vast reversible decrease of the surface resistance with increasingly negative polarization is notable.

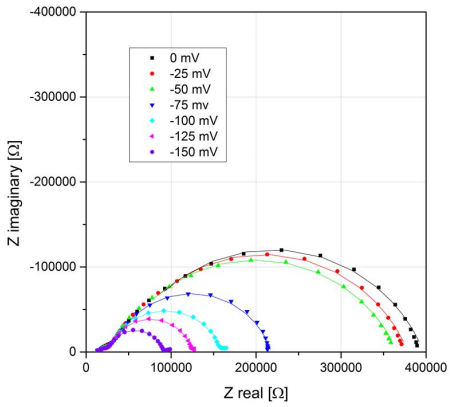


(a) 0 to −150 mV bias

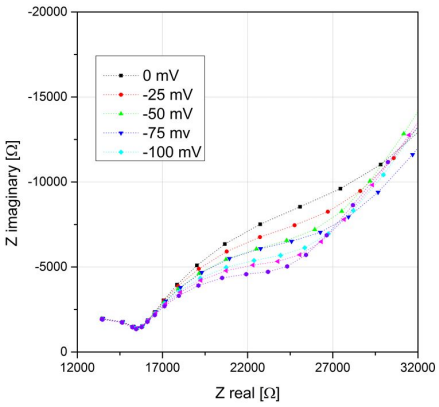


(b) 0 to −150 mV bias, zoom

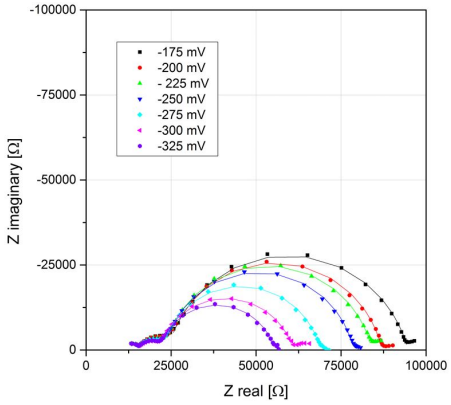


(c) −175 to −325 mV bias

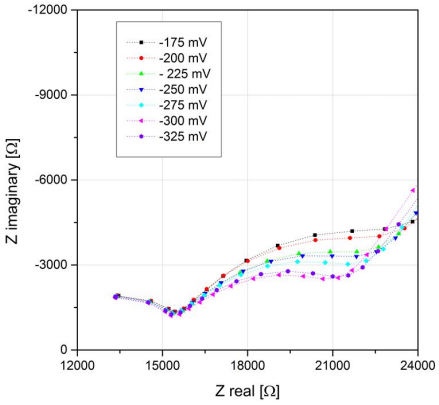


(d) −175 to −325 mV bias, zoom

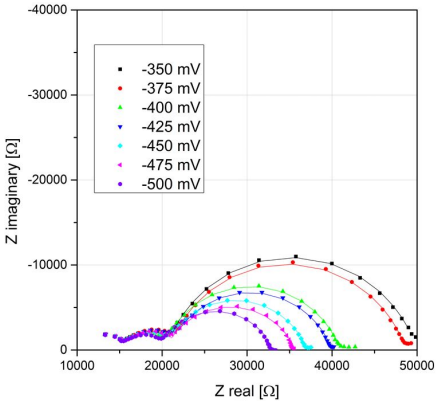


(e) −325 to −500 mV bias

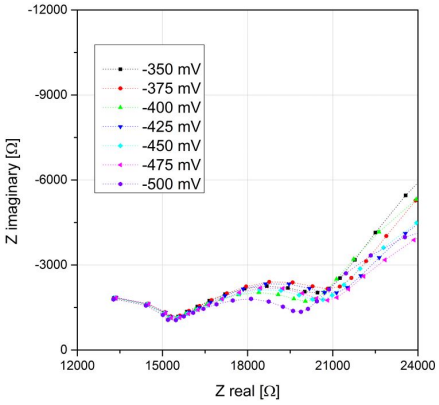


(f) −325 to −500 mV bias, zoom

Figure 4.7: Impedance spectra of a microelectrode with 80 µm diameter and bottom current collector under cathodic bias measured in humidified hydrogen at 625 °C. Data Points are measured values, fits according to figure 4.9 are represented by solid lines. Dotted lines are drawn as guide to the eye.

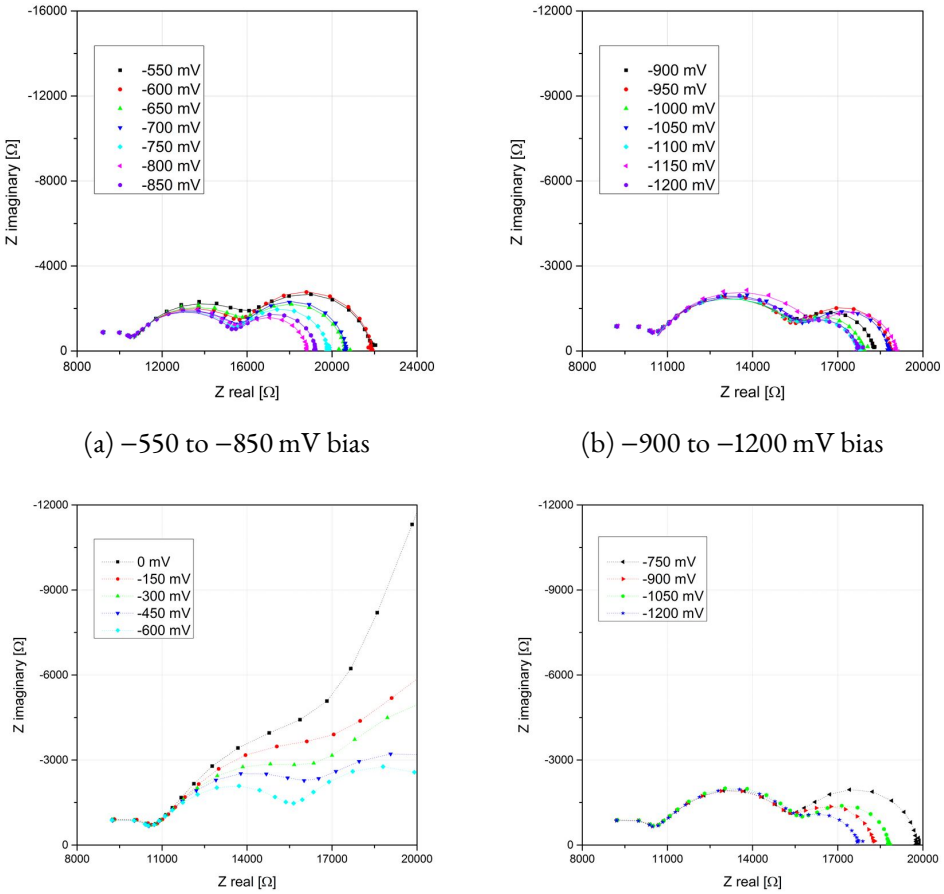


(a) −550 to −850 mV bias

(b) −900 to −1200 mV bias

(c) 0 to −600 mV bias

(d) −750 to −1200 mV bias

Figure 4.8: Impedance spectra of a microelectrode with 100 µm diameter and bottom current collector under cathodic bias measured in humidified hydrogen at 625 °C. Figures4.8a and 4.8b are entire spectra, figures4.8c to 4.8d show the intermediate frequency region. Data Points are measured values, fits according to figure 4.9 are represented by solid lines. Dotted lines are drawn as guide to the eye.

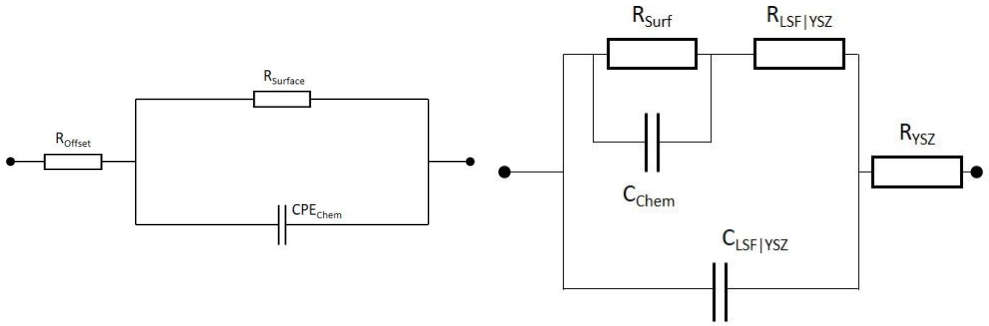


(a) Used for bias of 0 to −500 mV

(b) Used for bias of −500 to −1200 mV

Figure 4.9: Equivalent circuits used for fitting in reducing atmospheres with cathodic polarization.

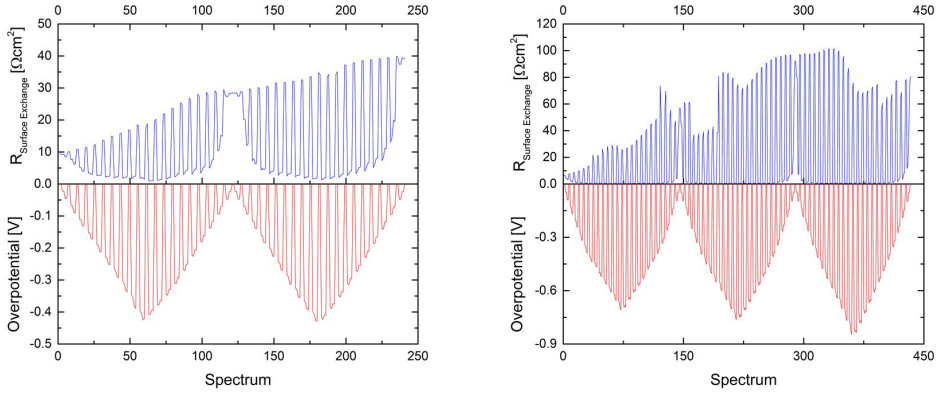


(a) 0 to −500 mV bias

(b) to −1200mV bias

Figure 4.10: Progression of surface exchange resistance and overpotential over the course of cathodic bias cycles. Measurements were taken in humidified hydrogen at 625 °C on microelectrodes with diameters of 100 µm (4.10a) and 80 µm (4.10b) and bottom current collector.

Anodic bias measurements

Anodic bias measurements were done with bias cycles of up to 500 mV in steps of 25 mV and up to 1200 mV in steps of 50 mV. Spectra are shown in figures 4.11 and 4.12. At low polarization a high frequency resistive offset, a low frequency semicircle and a slope feature at intermediate frequencies, similar to previous measurements in reducing atmosphere were found.

This slope feature again shows bias dependent behavior. With increasing anodic polarization up to about 400 mV bias, this slope gets slightly more pronounced. With further increase of polarization the slope changes into a small depressed semicircle. Considering that anodic bias first decreases the electronic charge carrier concentration, by decreasing electrons down to a minimum after which further decrease in electron concentration is overcompensated by an increase in hole concentration, this behavior is not unlikely. A comparison of the potentials at which the first notion of an underlying semicircle can be observed in the spectra yields potentials of about −300 mV for cathodic polarization and about 850 mV for anodic polarization. These values correspond to electrode overpotentials of roughly −250 mV and 650 mV respectively. From the Brouwer diagram, see section 2.2.1 the concentration of electronic charge carriers at these potentials can be estimated, and comparison shows similar values for both potentials in question. This again supports the assumption that this slope is connected to a limited electronic conductivity. Again the surface exchange resistance shows a vast decrease upon polarization, which can be disadvantageous in terms of influences of the counter electrode, as described above.

Spectra were fitted, using the equivalent circuit described in figure 4.9a. From the fit results the overpotential and the surface resistance were calculated as described above. The progression thus obtained is shown in figure 4.13. In both experiments, the initial surface exchange resistance is higher than in previous experiments (40 Ω cm and 60 Ω cm compared to 10 Ω cm) by a factor of 4 and 6 respectively, which is due to thermal history of the sample, caused by previous experiments. However, no further degradation could be observed during the two 500 mV anodic bias cycles. In the second experiment with bias of up to 1200 mV a drastic decrease in surface exchange resistance is notable upon the first application of higher bias voltages. This decrease is irreversible as bias free spectra taken within consecutive cycles show. A more detailed discussion on this effect is given in section 4.5.1.

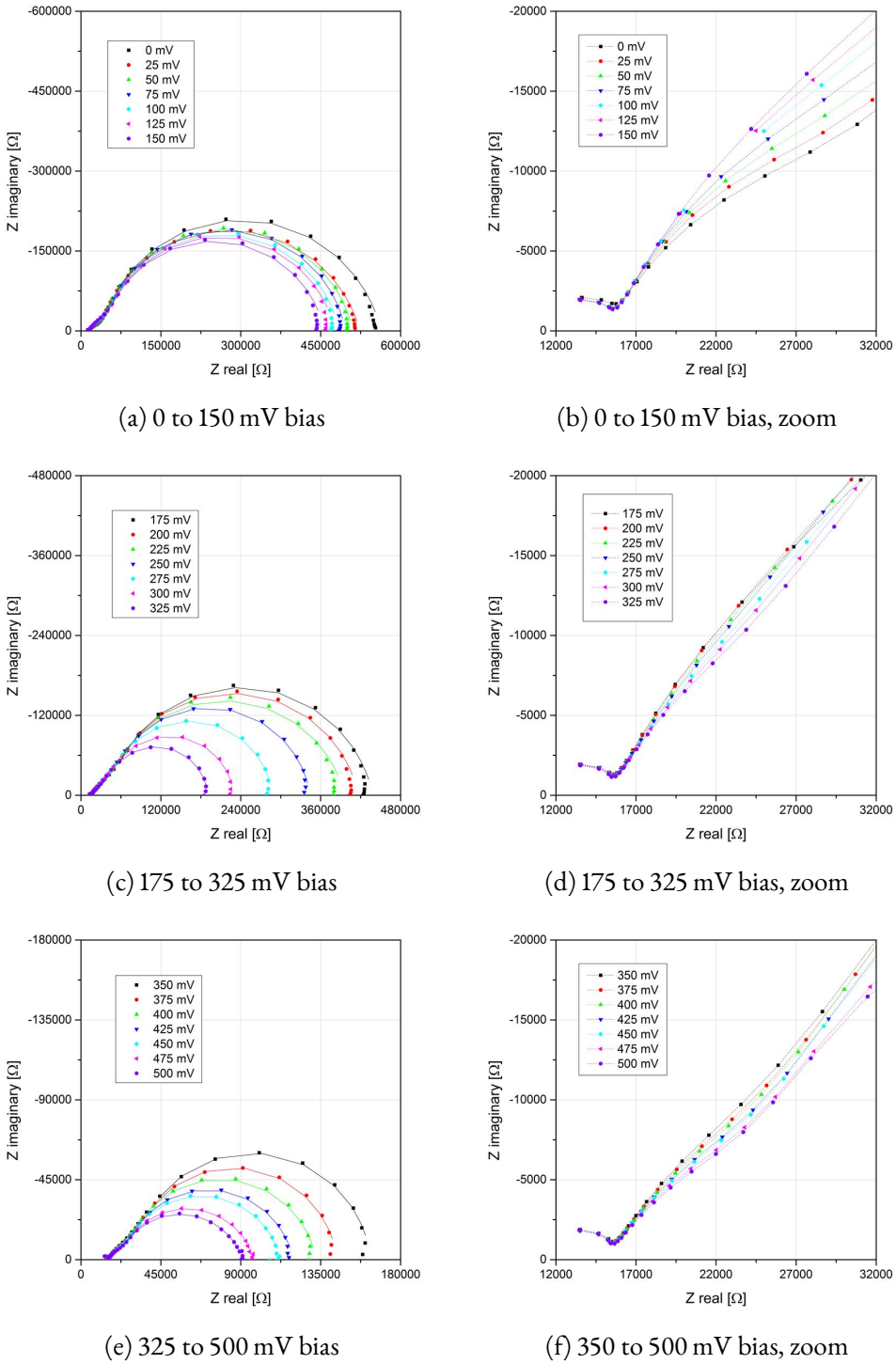


(a) 0 to 150 mV bias

(b) 0 to 150 mV bias, zoom

(c) 175 to 325 mV bias

(d) 175 to 325 mV bias, zoom

(e) 325 to 500 mV bias

(f) 350 to 500 mV bias, zoom

Figure 4.11: Impedance spectra of a microelectrode with 80 µm diameter and bottom current collector under anodic bias measured in humidified hydrogen at 625 °C. Data points are measured values, fits according to figure 4.9a are represented by solid lines. Dotted lines are drawn as guide to the eye.

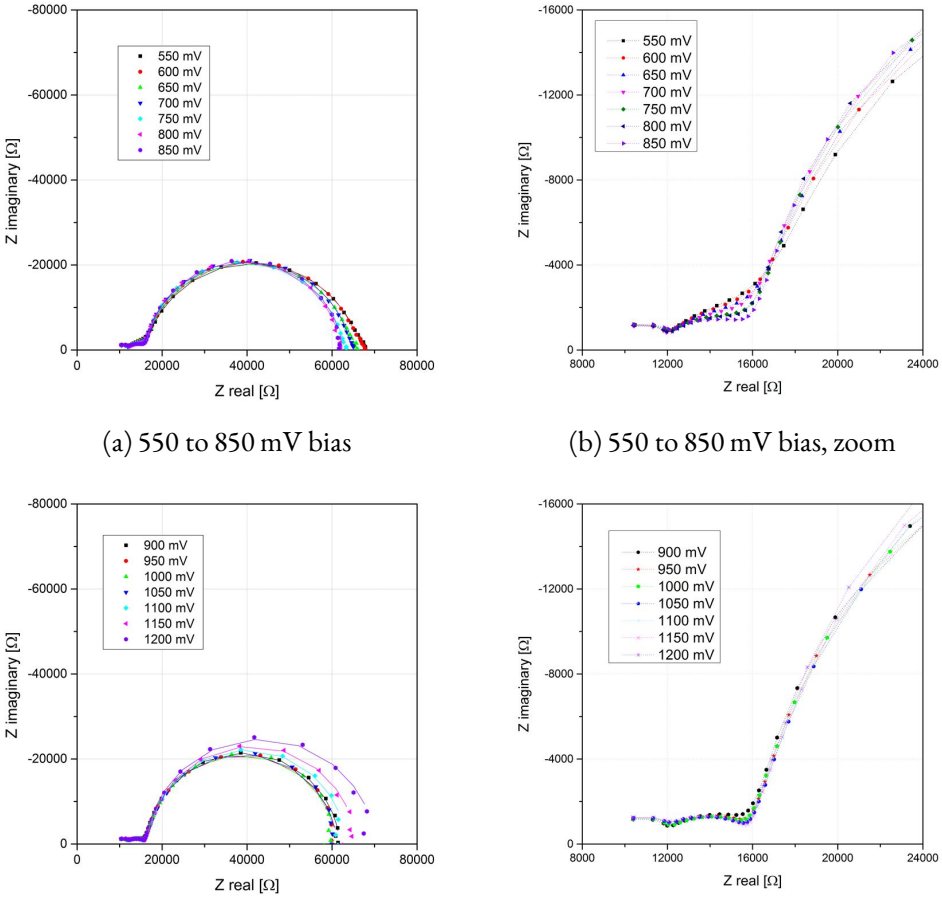


(a) 550 to 850 mV bias

(b) 550 to 850 mV bias, zoom

(c) 900 to 1200 mV bias

(d) 900 to 1200 mV bias, zoom

Figure 4.12: Impedance spectra of a microelectrode with 100 µm diameter and bottom current collector under anodic bias measured in humidified hydrogen at 625 °C. Data points are measured values, fits according to figure 4.9a are represented by solid lines. Dotted lines are drawn as guide to the eye.

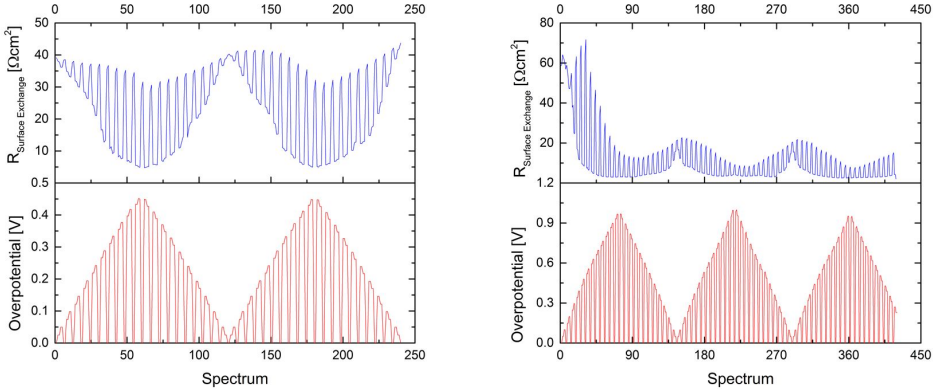


(a) 0 to 500 mV bias

(b) 0 to 1200 mV bias

Figure 4.13: Progression of surface exchange resistance and overpotential over the course of anodic bias cycles. Measurements were taken in humidified hydrogen at 625 °C on microelectrodes with diameters of 80 µm (figure 4.13a) and 100 µm (figure 4.13b) and bottom current collector.

## 4.3.2 Measurements in oxidizing atmosphere

### Cathodic polarization

In synthetic air, cathodic bias measurements were performed with bias cycles of up to −500 mV in steps of 25 mV. At low bias voltages the spectra showed a high frequency offset, a small depressed semicircle at intermediate frequencies, and a dominant semicircle at low frequencies. With increasing bias, the dominant semicircle decreases in size, whereas the intermediate semicircle roughly maintains its size, while getting better resolved.

The low frequency semicircle of the spectra was fitted using the equivalent circuit shown in figure 4.15a. From the fit results normalized surface exchange resistance and overpotential were calculated, see equations 4.3 and 4.5, with an active surface factor of $f_A$=0.25, since the area of the electrode film above the current collector is believed to be inactive. The progression thus obtained is shown in figure 4.15b. Initial values of the surface resistance (25 Ω cm$^2$) are within reasonable deviation from previous experiments (45 Ω cm$^2$). Again the surface exchange resistance decreases upon polarization, and additionally shows irreversible degradation effects.

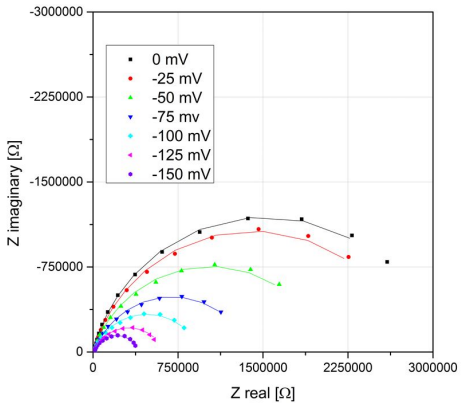


(a) 0 to −150 mV bias

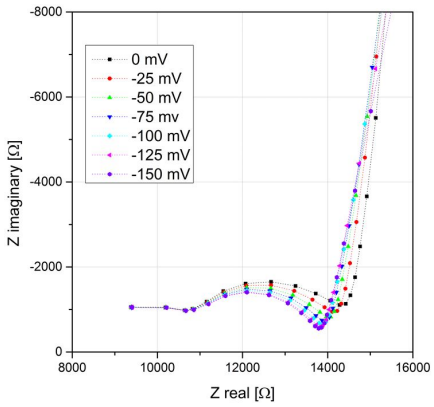


(b) 0 to −150 mV bias

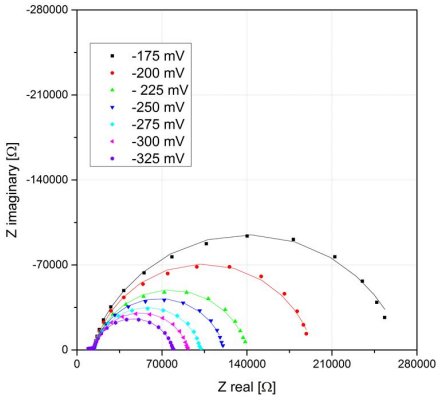


(c) −175 to −325 mV bias

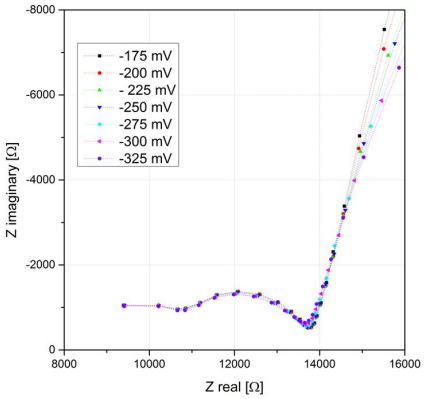


(d) −175 to −325 mV bias

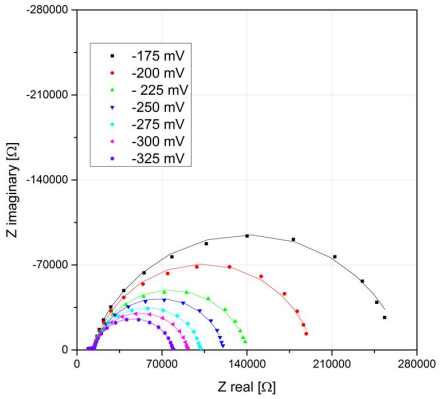


(e) −350 to −500 mV bias

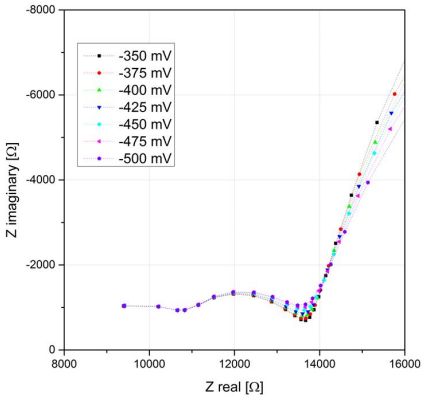


(f) −350 to −500 mV bias

Figure 4.14: Impedance spectra of a microelectrode with 100 µm diameter and bottom current collector under cathodic bias from 0 to −500 mV, measured at 625 °C in synthetic air. Points are measured values, fits are represented by solid lines. Dotted lines are drawn as guide to the eye.

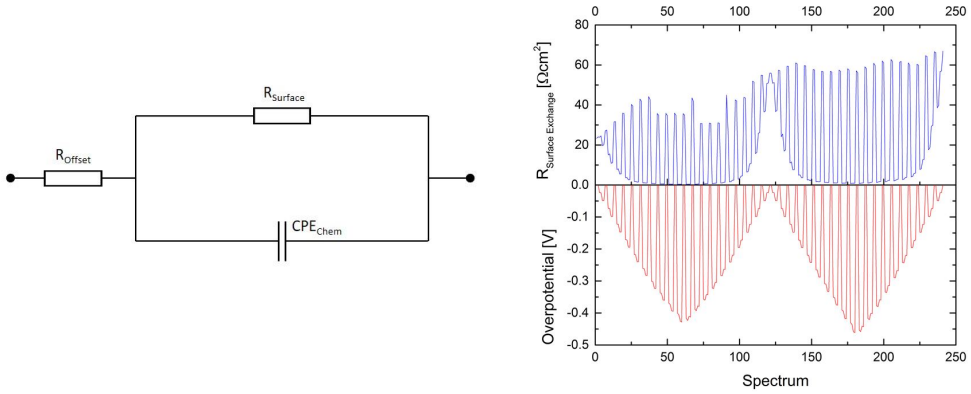


(a) Equivalent circuit used for fitting (b) Progression of surface exchange resistance

Figure 4.15: Left: Equivalent circuit used for fitting of measurements in oxidizing atmosphere. Right: Progression of surface exchange resistance and overpotential over the course of two bias cycles.

### Anodic polarization

Anodic bias measurements were taken with bias cycles of up to 500 mV in steps of 25 mV. Figure 4.16 shows the corresponding impedance spectra. At low bias voltages, the spectra showed a high frequency offset, a small depressed semicircle at intermediate frequencies, and a dominant semicircle at low frequencies.

With increasing anodic polarization this intermediate feature evolves into a slope feature, and might indicate a charge carrier transport limitation. The electronic conductivity is expected to be high, due to the large hole concentration. Therefore a transport limitation of electronic charge carriers is unlikely. However, the ionic conductivity decreases under anodic polarization because of the decreasing oxygen vacancy concentration. Consequently, the transport of the ionic charge carriers might turn into the rate limiting step of the exchange reaction. At around 150 mV the dominant semicircle becomes stretched out towards higher resistances at low frequencies, which indicates degradation of the surface exchange resistance during the measurement. With further increase of bias, the dominant semicircle changes into a depressed complex feature.

It should be noted, that due to the decrease of the surface resistance and the complex shape of the spectra, some features of the spectra might be caused by the counter electrode. A more detailed investigation on the impedance of counter electrodes is given in section 4.4.

For low polarizations, spectra were fitted in the low frequency range with the equivalent circuit described above (see figure 4.15a). At bias voltages over 300 mV spectra could not be evaluated quantitatively by simple fit models, and values for electrolyte resistance and surface resistance were simply estimated by eye. Surface exchange resistances were normalized and overpotentials were calculated according to equations 4.3 (with $f_A$=0.25) and 4.5, see figure 4.17.

In analogy to reducing atmosphere an irreversible decrease in surface resistance was observed upon first application of anodic bias. The relative decrease by a factor of three regarding the

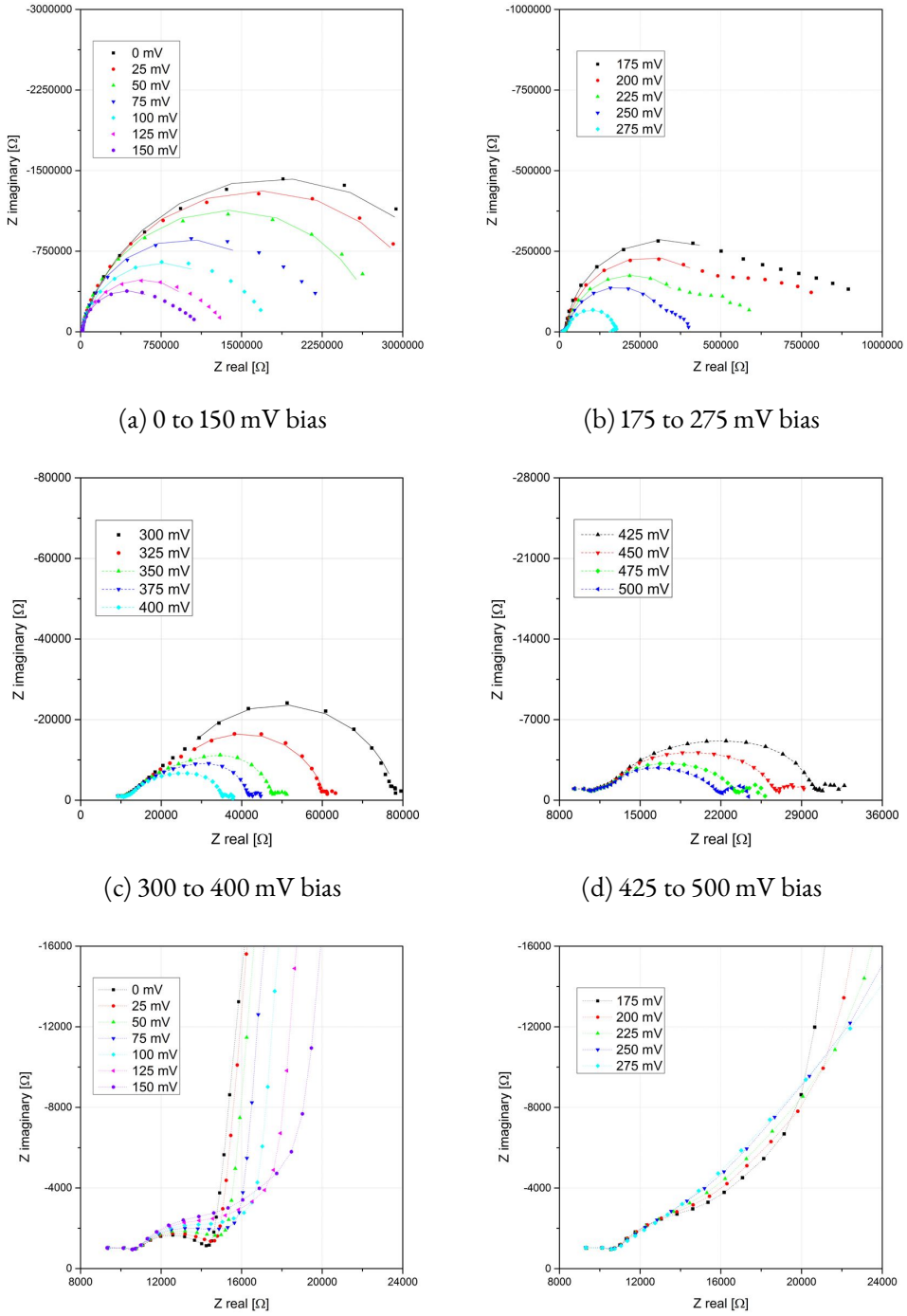


(a) 0 to 150 mV bias

(b) 175 to 275 mV bias

(c) 300 to 400 mV bias

(d) 425 to 500 mV bias

(e) Zoom on intermediate region

(f) Zoom on intermediate region

Figure 4.16: Impedance spectra of a 100 µm microelectrodes with bottom current collectors under anodic bias from 0 to 500 mV measured in synthetic air at 625 °C. Symbols represent measured data points, fits are represented by solid lines. Dotted lines are drawn as visual guides.

bias free spectra is comparable to the effect under reducing atmospheres. However, this decrease happens at lower potentials (bias of up to 500 mV) compared to measurements in humidified hydrogen, where this effect was only observable at polarization with up to 1200 mV bias. An explanation for this effect is thoroughly discussed in section 4.5.1.

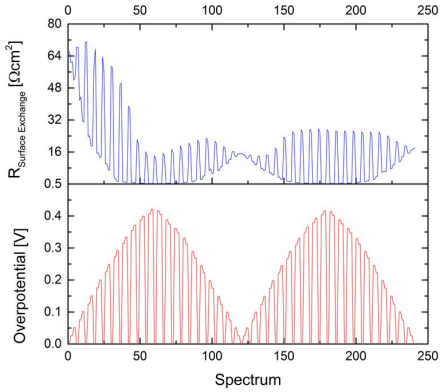


Figure 4.17: Surface exchange resistance and electrode overpotential under anodic bias, measured on a microelectrode with with 100 µm diameter and bottom current collector in synthetic air at 625 °C.

## 4.4 Counter electrodes

As the first set of bias experiments exhibited very low surface resistances under polarization as well as additional features, the influence of the counter electrode on the overall impedance had to be examined. Therefore different counter electrodes were investigated with regards to their resistance in different oxidizing atmospheres.

### 4.4.1 Porous platinum paste, dried

The first electrodes tested were porous platinum electrodes, produced by brushing platinum paste, and drying it at 130 °C. Figure 4.18 shows the respective impedance spectra. The electrode resistance shows a very strong degradation, therefore no clear dependency on the oxygen partial pressure could be observed. It can, however, be assumed, that the electrode resistance decreases at lower oxygen partial pressures, which is overshadowed by the massive degradation over the course of the experiment. As the electrode resistance (see figure 4.19), ranging from 1000 to 16 000 Ω, is within the same order of magnitude as the electrode resistance of the LSF microelectrodes under bias, alternative counter electrodes or preparation routes had to be taken into account.

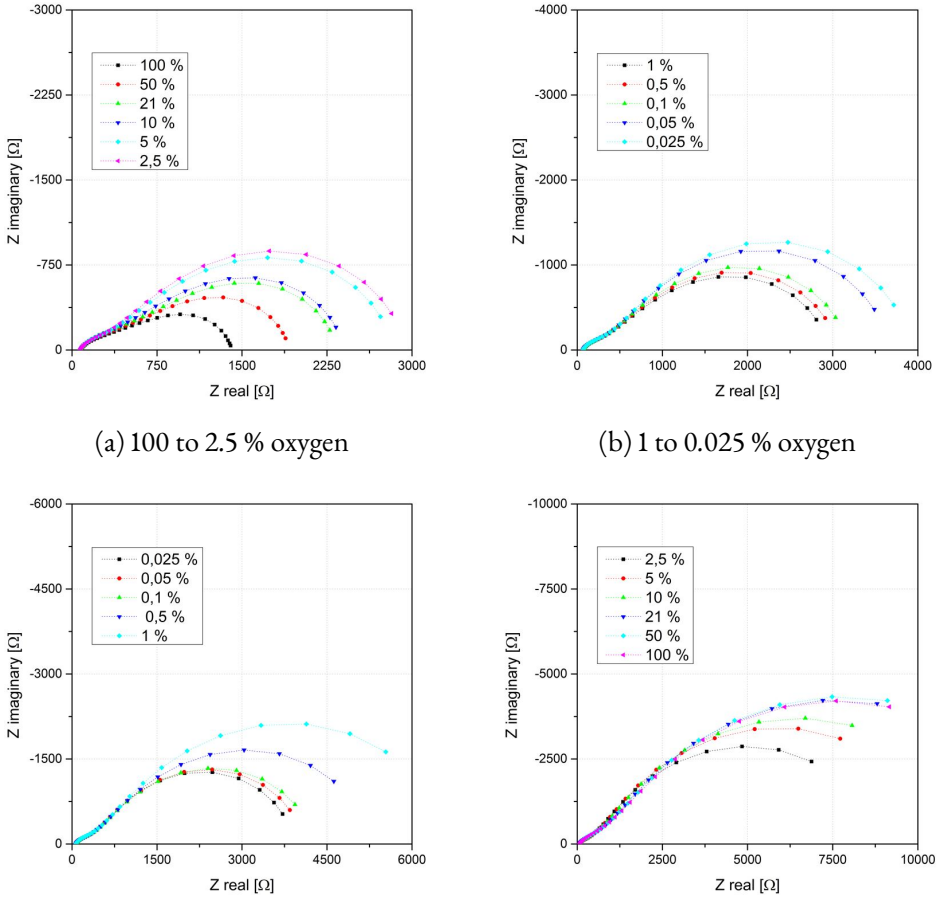


(a) 100 to 2.5 % oxygen

(b) 1 to 0.025 % oxygen

(c) 0.025 to 1 % oxygen

(d) 2.5 to 100 % oxygen

Figure 4.18: Impedance spectra of 5 mm × 5 mm symmetrical macroelectrodes, of dried platinum paste, measured at 625 °C, with oxygen percentage decreasing stepwise from 100 to 0.025 % (4.18a and 4.18b), then increasing again from 0.025 to 100 % (4.18c and 4.18d).

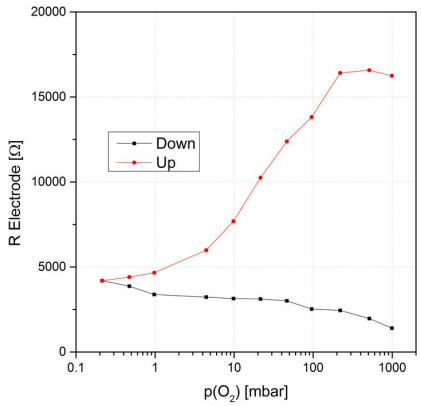


Figure 4.19: Estimated electrode resistance at 625 °C and oxygen partial pressures decreasing from 100 to 0.1 % (black line), and increasing back to 100 %(red line).

## 4.4.2 Porous platinum, annealed

In a second approach, counter electrodes of annealed platinum paste were examined. Spectra (see figure 4.20) showed complex depressed features, from which the total electrode resistances were estimated. In comparison with the dried platinum paste electrodes, the annealed ones showed much higher resistances from 10 000 to 60 000 Ω, see figure4.21. Although no degradation of the electrode resistance was observed, annealed porous platinum electrodes were not considered as convenient counter electrodes due to their high impedance.

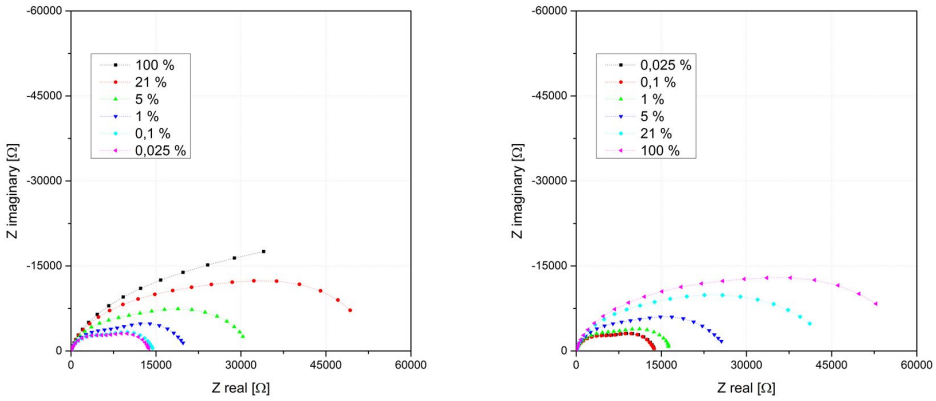


(a) 100 to 0.025 % oxygen

(b) 0.025 to 100 % oxygen

Figure 4.20: Impedance spectra of 5 mm × 5 mm symmetrical annealed platinum paste macroelectrodes, measured at 625 °C, with oxygen percentage decreasing stepwise from 100 to 0.025 % (4.20a), and increasing again from 0.025 to 100 % (4.20b).

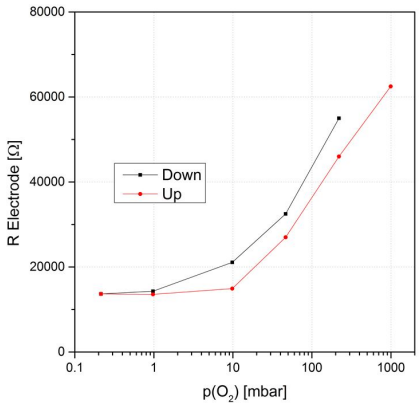


Figure 4.21: Estimated total electrode resistance of 5 mm × 5 mm symmetrical annealed platinum paste macroelectrodes at 625 °C for oxygen partial pressure decreasing from 100 to 0.025 % (black line), and increasing again from 0.025 to 100 % (red line).

### 4.4.3 Porous LSF and platinum combined

Next, a counter electrode made of a combination of LSF paste and platinum paste, see section 3.1.3, was investigated. Spectra (figure 4.22) showed depressed features, which could be resolved into a 45° slope and a dominant low frequency arc at lower oxygen partial pressures. The electrode resistance (figure 4.23) showed comparatively low values from 50 to 250 Ω, and only slight degradation effects. Therefore, porous LSF and platinum were used as counter electrode for further bias experiments.

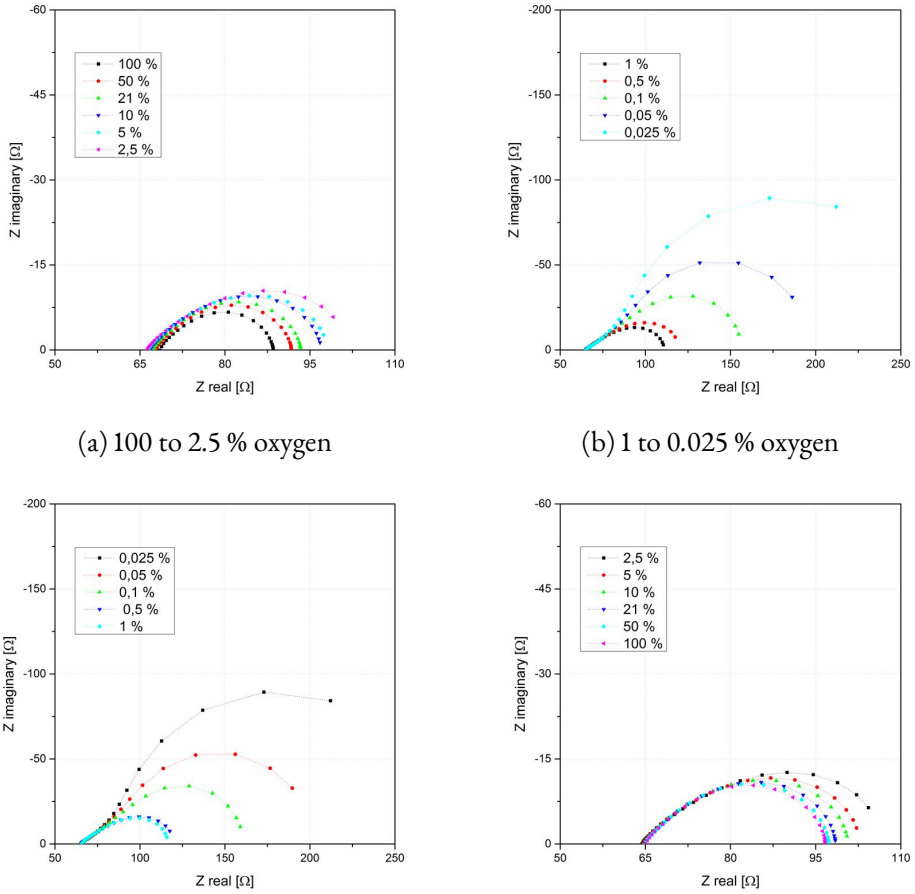


(a) 100 to 2.5 % oxygen

(b) 1 to 0.025 % oxygen

(c) 0.025 to 1 % oxygen

(d) 2.5 to 100 % oxygen

Figure 4.22: Impedance spectra of 5 mm × 5 mm symmetrical porous LSF and platinum macro-electrodes, measured at 625 °C, with oxygen percentage decreasing stepwise from 100 to 0.025 % (4.22a and 4.22b), then increasing again from 0.025 to 100 % (4.22c and 4.22d).

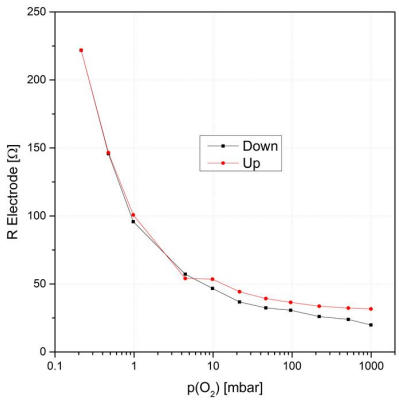


Figure 4.23: Total electrode resistance of 5 mm × 5 mm symmetrical porous LSF and platinum macroelectrodes at 625 °C for oxygen partial pressure decreasing from 100 to 0.025 % (black line), and increasing again from 0.025 to 100 % (red line).

## 4.5 Second set of bias experiments

The first set of bias experiments showed a massive decrease of the surface exchange resistance under polarization, down to values within the order of magnitude of the resistance of the counter electrodes. Moreover, measurements in oxidizing atmospheres exhibited complex features under anodic polarization which could not be evaluated by any of the simplified equivalent circuits presented in this work. Therefore counter electrodes with lower resistance were used in consecutive experiments. This also had the benefit of eliminating any contamination from the formerly used (non annealed) platinum paste.

### 4.5.1 Measurements in reducing atmosphere

#### Cathodic polarization

Figures 4.24 and 4.25 show spectra measured on microelectrodes of 200 µm diameter and with bottom current collector in humid hydrogen. Spectra show of a high frequency offset, a slope at intermediate frequencies and a dominant low frequency semicircle. With increasing bias, beginning at about −200 to −300 mV, the slope gets less and less pronounced and gives way to a small semicircle that gets more and more distinguishable with increasing bias, while maintaining the same size. This feature is again attributed to the electronic transport resistance, as discussed in section 4.3.1. The dominant semicircle decreases in size with increasing bias, down to a resistance of about 250 Ω (0.07 Ω cm$^2$) under very high polarization. Therefore a significant portion of the applied bias is lost in the electrolyte, and at the interface resistance.

Spectra were fitted using either of the circuits shown in figure 4.9 for bias voltages of up to −500 mV and from −500 to −1200 mV respectively. From the fit results the area specific surface resistance, and the chemical capacitance were calculated, see equations 4.3 and 4.4, both normalized to the entire electrode ($f_A = 1$ and $f_V = 1$). Since part of the applied bias is lost at the electrolyte resistance, or at the interface, the effective overpotential at the electrode was

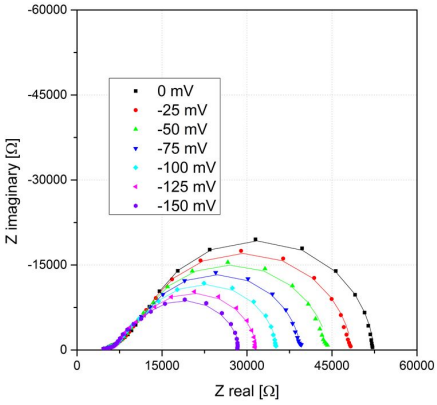


(a) 0 to −150 mV bias

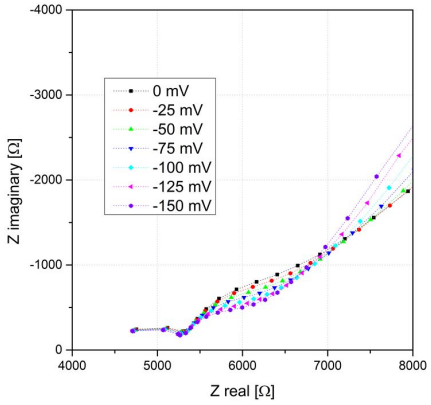


(b) 0 to −150 mV bias, zoom

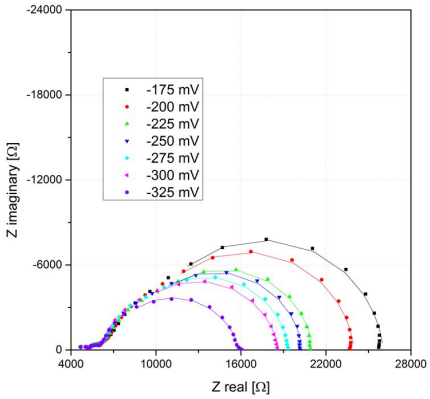


(c) −175 to −325 mV bias

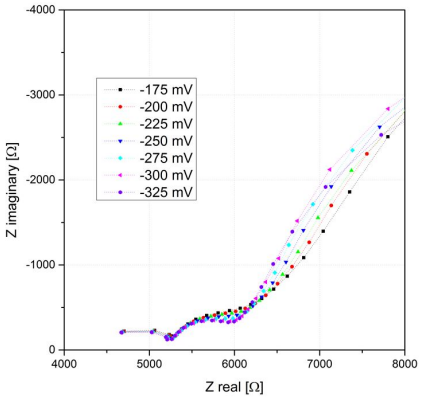


(d) −175 to −325 mV bias, zoom

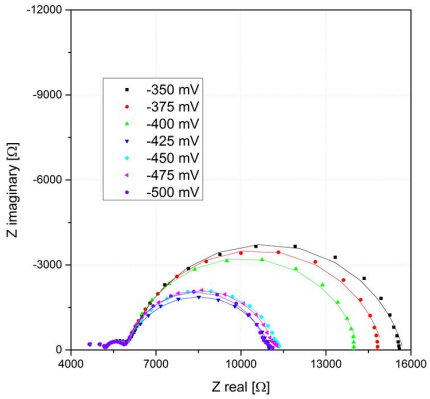


(e) −325 to −500 mV bias

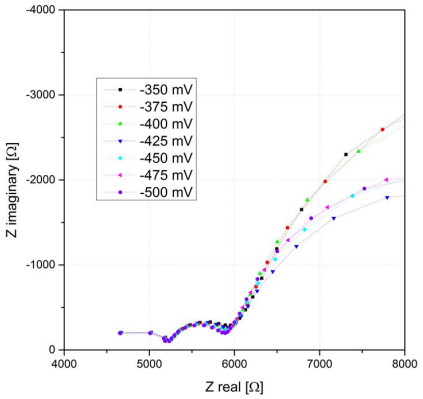


(f) −350 to −500 mV bias, zoom

Figure 4.24: Impedance spectra of microelectrodes with 200 µm diameter and bottom current collectors under cathodic bias from 0 to −500 mV measured in humidified hydrogen at 625 °C. Entire spectra (4.24a, 4.24c and 4.24e) and magnifications of the intermediate frequency region (4.24b, 4.24d and 4.24f).

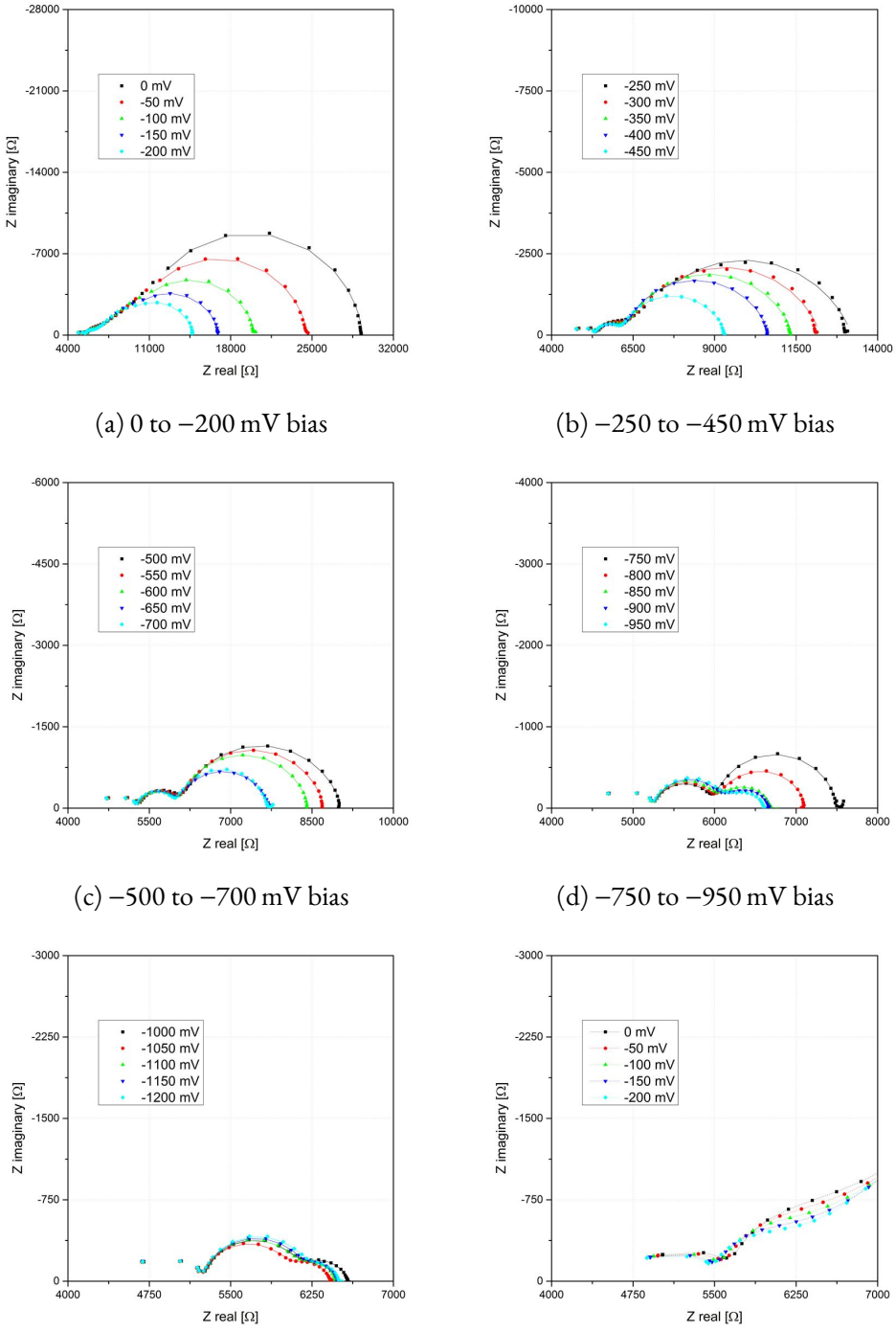


(a) 0 to −200 mV bias

(b) −250 to −450 mV bias

(c) −500 to −700 mV bias

(d) −750 to −950 mV bias

(e) −1000 to −1200 mV bias

(f) 0 to −200 mV bias, zoom

Figure 4.25: Impedance spectra of microelectrodes with 200 µm diameter and bottom current collectors under cathodic bias from 0 to −1200 mV measured in humid hydrogen at 625 °C. Entire spectra (4.25a, 4.25b, 4.25c, 4.25d and 4.25e) and a magnifications of the intermediate frequency region (4.25f).

calculated, see equations 4.5 and 4.6 respectively. Hence, surface exchange resistance, chemical capacitance and effective electrode overpotential over the course of several bias cycles were obtained, see figures 4.26a and 4.26b.

The initial values of the surface resistance (5 Ω cm$^2$ and 13 Ω cm$^2$) are within reasonable deviation from previous experiments. Under bias, the surface resistance showed a vast decrease. Furthermore a continuous degradation of the surface resistance in the bias free spectra could be observed over the course of the experiment. In the first experiment, with bias up to −500 mV, the chemical capacitance increased with increasing bias while for the bias free spectra it showed minor scattering, and a continuous slight decrease over the course of the experiment. When applying higher bias voltages of up to −1200 mV, the chemical capacitance showed a similar increase with rising bias, although after the first bias cycle, an irreversible decrease of the chemical capacitance could be observed. Furthermore the bias free spectra showed strong variations. These irreversible changes on the electrode properties might be explained by the strong cathodic bias that causes reducing conditions that are out of the stability range of LSF.

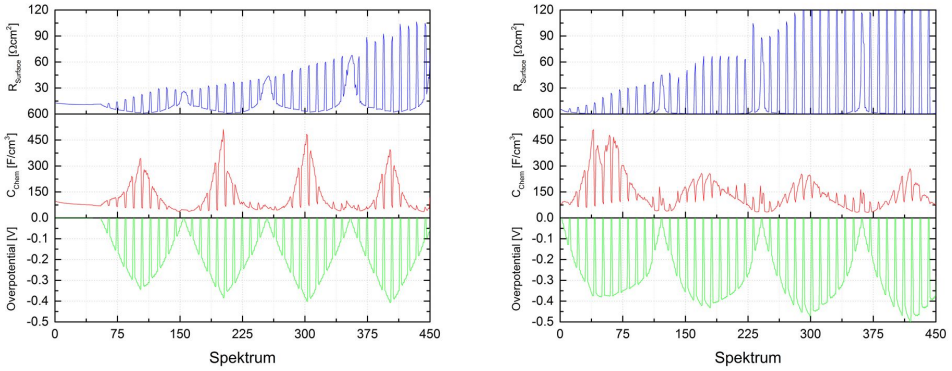


(a) 0 to −500 mV bias

(b) 0 to −1200 mV bias

Figure 4.26: Progression of the area specific surface exchange resistance, the chemical capacitance and the effective electrode overpotential over the course of several bias cycles, from 0 to −500 mV (figure 4.26a) and from 0 to −1200 mV (figure 4.26b) cathodic bias. All data were obtained from measurements on 200 µm microelectrodes with bottom current collector, in humid hydrogen at 625 °C.

Figure 4.27 shows the chemical capacitance (on a logarithmic scale) versus the electrode overpotential. In the experiment with up to −500 mV cathodic bias, the chemical capacitance within the first phase of increasing bias shows significant deviations from the other cycles, both in the absolute values and also in the slope. Furthermore a continuous decrease of the chemical capacitance over the course of the experiment could be observed. The curves were fitted using an exponential equation (see equation 4.7), which yielded an average slope b of -9.7 for chemical capacitance (logarithmic) versus overpotential which corresponds to a slope of -0.19 versus the logarithmic oxygen partial pressure. This is slightly smaller than the slope expected from the defect model (-0.24), as described in section 2.2.

$$C_{\mathrm{Chem}} = A \times e^{b \times \eta} \tag{4.7}$$

In the experiment with up to −1200 mV bias, differences between the cycles are much more distinctive. The chemical capacitance decreases over the course of the experiment. Is in the previously described experiment, there is a notable difference between the first phase and the remaining phases, and a continuous decrease of the chemical capacitance over the course of the experiment is again visible. The curves were again fitted using equation 4.7, where possible. This yielded an average slope of -7.8 vs the overpotential and -0.15 versus the logarithmic oxygen partial pressure respectively, again this is lower than expected from defect model calculations (-0.24).

Figure 4.28 shows images of two electrodes from the same sample, one after applying a cathodic bias of up to −500 mV, the other being subject to the same measuring conditions (atmosphere and temperature) but without any polarization. The only notable feature on the polarized electrode is a slightly darker spot, where the electrode was contacted with the platinum needle. Aside from this, no further further differences could be observed in the microscopic images. In figure 4.29 images of two microelectrodes are shown. Again the top row depicts the polarized electrode, whereas the bottom row represents a not measured electrode from the same sample. Similar to the previous experiment, a dark spot can be seen where the needle contacted the electrode. Compared to the former experiment, the spot is more pronounced here. Additionally the area between the current collector grid is slightly darker for the polarized electrode, which might be due to irreversible changes in the electrode, i.e. a exsolution of metallic iron [39] or phase decomposition of the LSF.

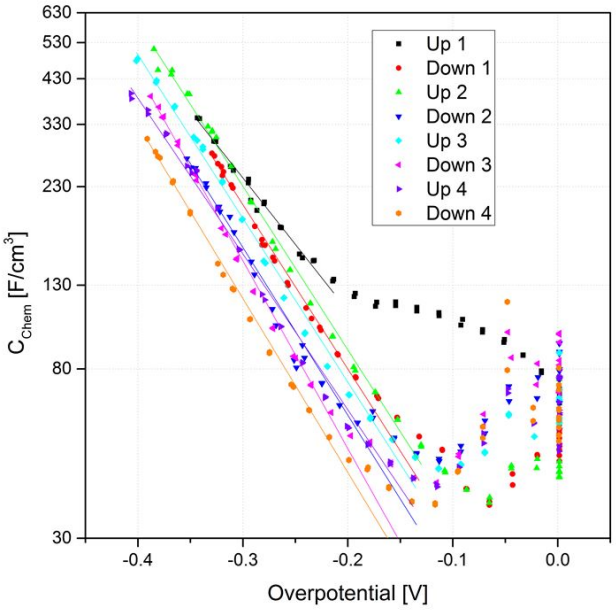


(a) 0 to −500 mV bias

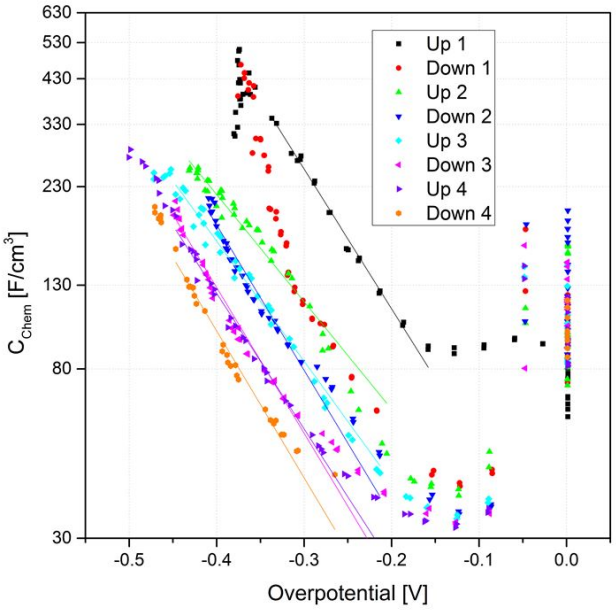


(b) 0 to −1200 mV bias

Figure 4.27: Chemical capacitance as a function of the effective electrode overpotential, from 0 to −500 mV (figure 4.27a) and from 0 to −1200 mV (figure 4.27b) cathodic bias. All data obtained from measurements on 200 µm microelectrodes with bottom current collector, in humid hydrogen at 625 °C. Measured values are shown as markers, the lines represent exponential fits.

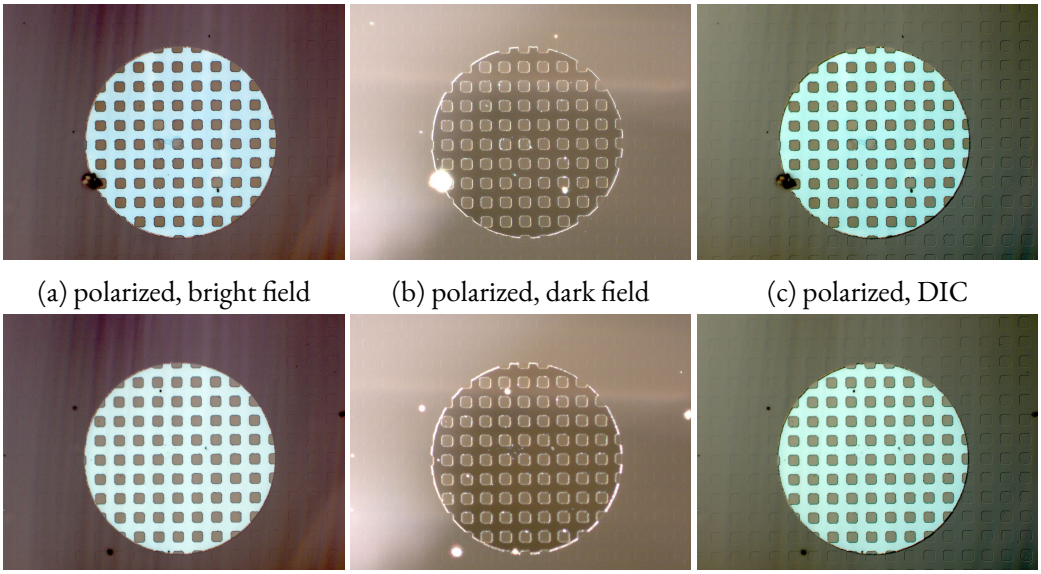

(a) polarized, bright field (b) polarized, dark field (c) polarized, DIC

(d) not polarized, bright field (e) not polarized, dark field (f) not polarized, DIC

Figure 4.28: Bright field images (4.28a and 4.28d), dark field images (4.28b and 4.28e), and differential interference contrast images, DIC (4.28c and 4.28f) of two microelectrodes (200 µm diameter) from the same sample. The electrode in the top row was polarized, while the one in the bottom row was subjected to the same atmosphere and temperature but not polarized. Measurements were taken in humidified hydrogen at 625 °C with cathodic bias of up to −500 mV applied.

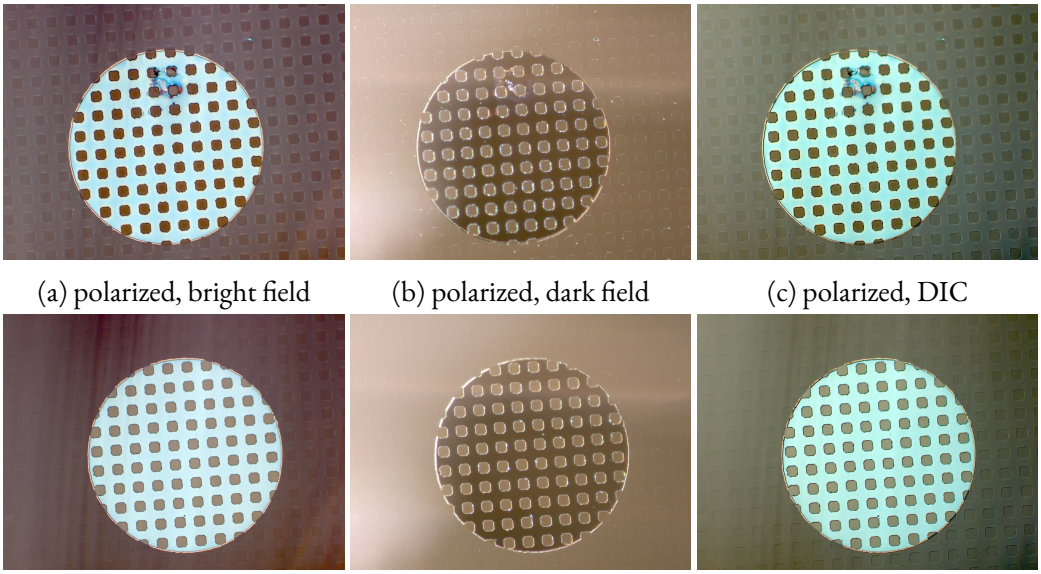

(a) polarized, bright field (b) polarized, dark field (c) polarized, DIC

(d) not polarized, bright field (e) not polarized, dark field (f) not polarized, DIC

Figure 4.29: Bright field images (4.29a and 4.29d), dark field images (4.29b and 4.29e), and differential interference contrast images, DIC (4.29c and 4.29f) of two microelectrodes (200 µm diameter) from the same sample. The electrode in the top row was polarized, while the one in the bottom row was subjected to the same atmosphere and temperature but not polarized. Measurements were taken in humidified hydrogen at 625 °C with cathodic bias of up to −1200 mV applied.

Anodic polarization

Figures 4.30 and 4.31 show spectra of microelecetrodes (200 µm diameter) under anodic polarization. Measurements were taken in humidified hydrogen at 625 °C. Spectra consisted of a high frequency intercept, a slope at intermediate frequencies and a dominant semicircle at low frequencies. This slope increases slightly with rising bias up to about 150 mV. With further increasing bias, the slope gets smaller. At about 600 to 700 mV a small semicircle becomes visible and gets more and more pronounced at higher bias voltages. This behavior fits the expectations, as the slope is believed to occur due to limited electronic conductivity. The dominant semicircle, which is attributed to the surface exchange reaction, increases with rising bias up to a maximum at about 150 mV. Thereafter it continuously decreases with increasing bias.

Spectra were fitted using the equivalent circuit shown in 4.9a. From the fit results surface exchange resistance and the chemical capacitance of the low frequency semicircle were calculated, each normalized to the entire electrode ($f_A = 1$ and $f_V = 1$), see equations 4.3 and 4.4. Since part of the applied bias drops at the electrolyte resistance or at the interface, the effective overpotential at the electrode was calculated according to equation 4.5. This yielded the progression of area specific surface exchange resistance and chemical capacitance over the course of the experiments.

The initial value of the surface exchange resistance (8.5 $\Omega\,cm^2$) of the first experiment is within expectations from previous experiments, the second experiment shows a higher initial value (36 $\Omega\,cm^2$) due to thermal history of the sample, caused by previous experiments. The experiment with bias from 0 to 500 mV (figure 4.32a) showed a reversible increase of the surface exchange resistance with increasing anodic polarization, up to a maximum followed by a decrease at higher bias voltages. Over the course of the experiment this effect gets progressively overshadowed by the degradation of the electrode resistance. In the second experiment (figure 4.32b), this effect is only slightly visible at the start of the first cycle. However, after applying anodic bias the electrode resistance shows a irreversible decrease. The chemical capacitance exhibits very similar properties in both experiments. With increasing bias, it first decreases to a minimum at about 350 mV after which it continuously increases again. Additionally a slight continuous decrease of the chemical capacitance could be observed over the course of the whole experiment. In the experiment with 1200 mV bias, the chemical capacitance shows only minor changes after the first bias cycle, which is quite contrary to the drastic decrease of the electrode resistance. Since the chemical capacitance is a bulk property whereas the surface exchange resistance is a surface property on the surface, it is likely that high anodic polarization causes irreversible changes to the electrode surface.

In figure 4.33 the chemical capacitance (on a logarithmic scale) is plotted versus the electrode overpotential.

In the experiment with 500mV bias, there is an almost perfect exponential relation between the chemical capacitance and the electrode overpotential in the region from 0 to 300 mV. At higher potentials the chemical potential reaches a minimum, and increases again afterward. Between the individual bias cycles a steady decrease of the chemical capacitance is again noticeable, however the slope stays the same for all cycles. Exponential fits (equation 4.7) yielded an average slope of -3.7, which corresponds to about -0.07 versus the logarithmic oxygen partial pressure. This slope is much shallower than expected from the Brouwer diagram (-0.22). The experiment

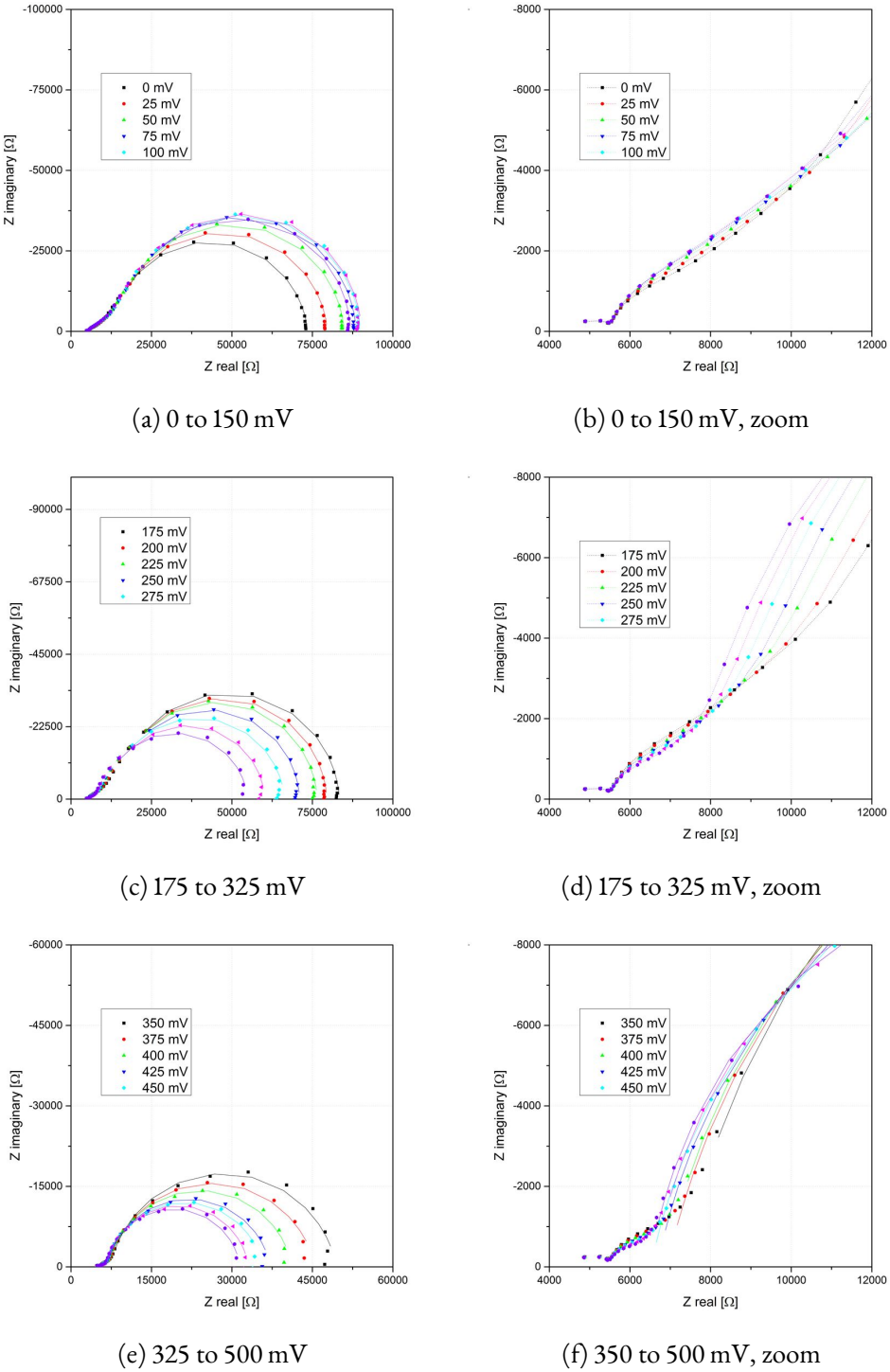


(a) 0 to 150 mV

(b) 0 to 150 mV, zoom

(c) 175 to 325 mV

(d) 175 to 325 mV, zoom

(e) 325 to 500 mV

(f) 350 to 500 mV, zoom

Figure 4.30: Impedance spectra of microelectrodes (diamteter of 200 μm) with bottom current collectors under anodic bias from 0 to 500 mV measured in humidified hydrogen at 625 °C. Full spectra (4.30a, 4.30c and 4.30e) and magnifications of the intermediate frequency region (4.30b, 4.30d and 4.30f).

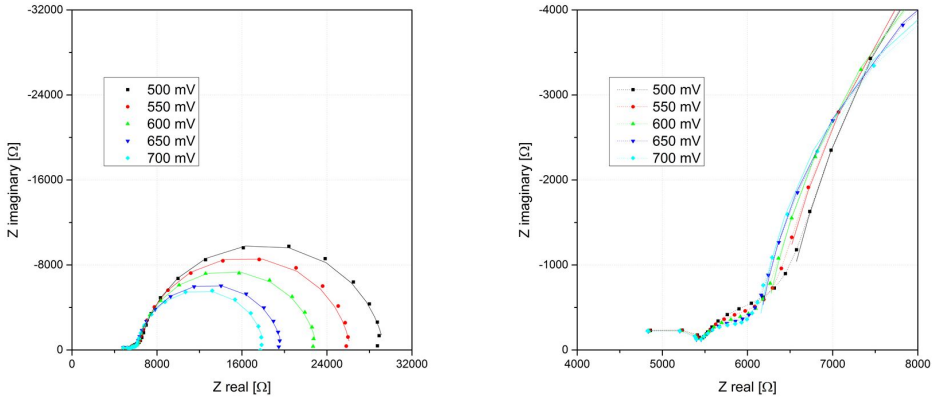


(a) 500 to 700 mV bias

(b) 500 to 700 mV bias, zoom

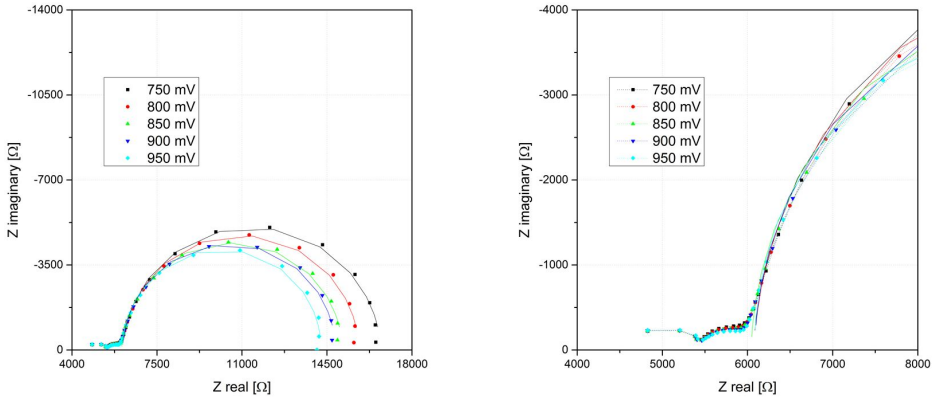


(c) 750 to 950 mV bias

(d) 750 to 950 mV bias, zoom

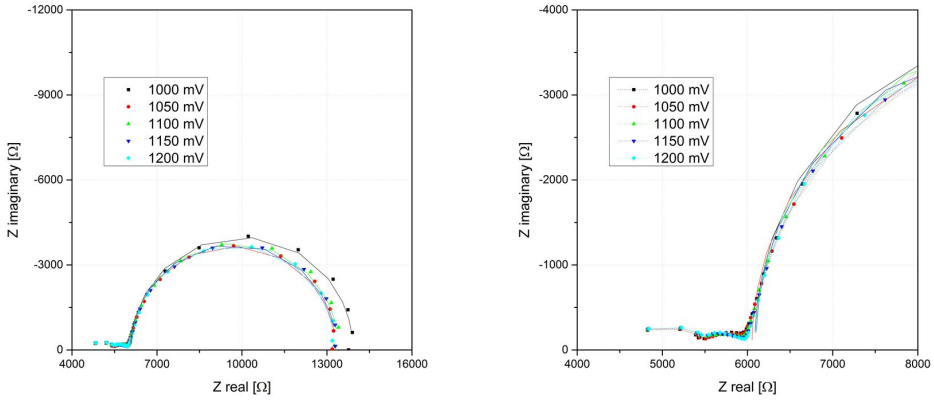


(e) 1000 to 1200 mV bias

(f) 1000 to 1200 mV bias, zoom

Figure 4.31: Impedance spectra of a microelectrode (200 µm diameter) with bottom current collectors under cathodic bias from 0 to −1200 mV measured in humidified hydrogen at 625 °C. Entire spectra (4.31a, 4.31c and 4.31e) and magnifications of the intermediate frequency region (4.31b, 4.31d and 4.31f).

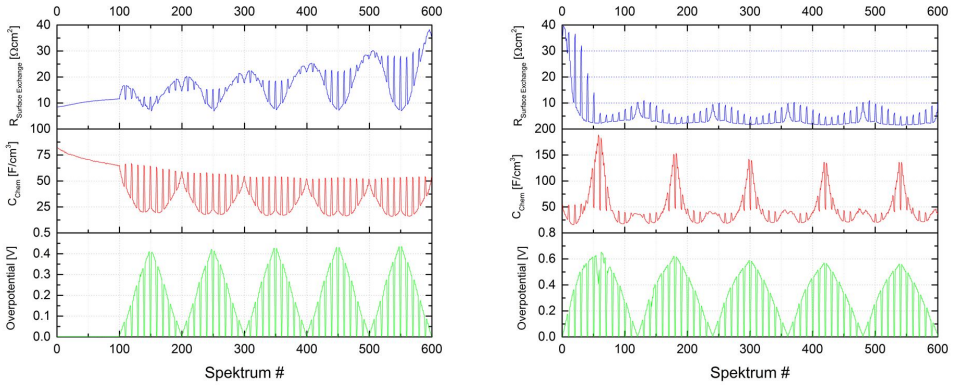


(a) 0 to 500 mV bias

(b) 0 to 1200 mV bias

Figure 4.32: Progression of the area specific total electrode resistance, the chemical capacitance and the effective electrode overpotential over the course of several bias cycles, from 0 to 500 mV (figure 4.32a) and from 0 to 1200 mV (figure 4.32b) anodic bias. Data obtained from measurements on a microelectrode (200 µm diameter) with bottom current collector, in humidified hydrogen at 625 °C.

with up to 1200 mV bias again shows an exponential relation between the chemical capacitance and the electrode potential, both left and right of the minimum. Exponential fits of the left branch again yielded an average slope of -4.3 versus the potential and -0.08 versus the logarithmic oxygen partial pressure respectively. This is again lower than expected from defect model calculations. For the right branch, from 450 to 650 mV, exponential fits yielded an average slope of 10.9 versus the potential and 0.21 versus the logarithmic oxygen partial pressure. From defect calculations a slope of 0.23 is expected, which is within reasonable agreement. Furthermore, in the experiment with up to 1200 mV bias a steady increase of the chemical capacitance over the course of the experiment is notable. This is especially pronounced at higher polarizations. A detailed discussion on the chemical capacitance with a comparison of different experiments is given in section 4.5.3.

In figure 4.34 images of two electrodes are shown. The top row represents the measured electrode, the bottom row represents another, not measured, electrode from the same sample. On the measured electrode, a change in the surface morphology is clearly visible in the area of the current collector. Furthermore, a scratch from the contacting needle is visible. During the measurement the sample was subjected to a bias of 1200 mV, of which about 650 mV drop at the LSF film. This potential difference can be converted into a pressure ratio, using Nernst's equation (equation 2.32). For 650 mV this corresponds to a pressure of about 16 orders of magnitude higher than the atmospheric pressure. Therefore, it is possible that oxygen or water is formed at the YSZ|Pt, the YSZ|LSF or the Pt|LSF interface. Hence, the resulting pressure might cause physical damage to the electrode film or the current collector grid. This also fits to the observed progression of electrode resistance and chemical capacitance. After the first application of high anodic bias, the electrode film gets physically deformed, which leads to a much larger surface and thus a much smaller surface resistance. Since the electrode appears to stay compact, meaning it doesn't completely disintegrate, but maintain a more or less cohesive structure, the chemical

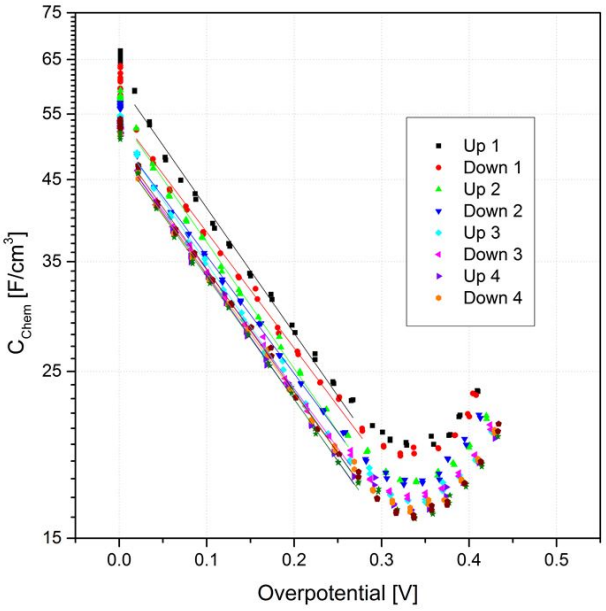


(a) 0 to −500 mV bias

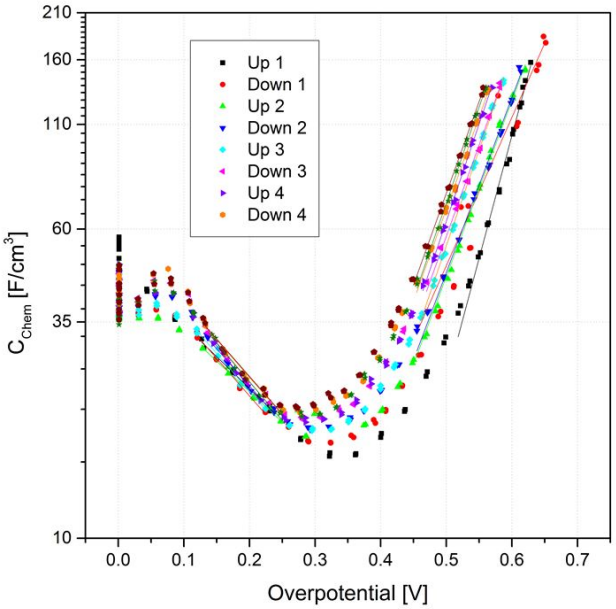


(b) 0 to −1200 mV bias

Figure 4.33: Chemical capacitance as a function of the effective electrode overpotential, from 0 to 500 mV (figure 4.33a) and from 0 to 1200 mV (figure 4.33b) anodic bias. Data obtained from measurements on a microelectrode (200 µm diameter) with bottom current collector, in humidified hydrogen at 625 °C. Data points are shown as markers, the lines represent exponential fits.

capacitance, being a bulk property, shows only minor changes. At lower bias of up to 500 mV neither surface resistance nor microscopic pictures suggested any structural damage to the LSF film.

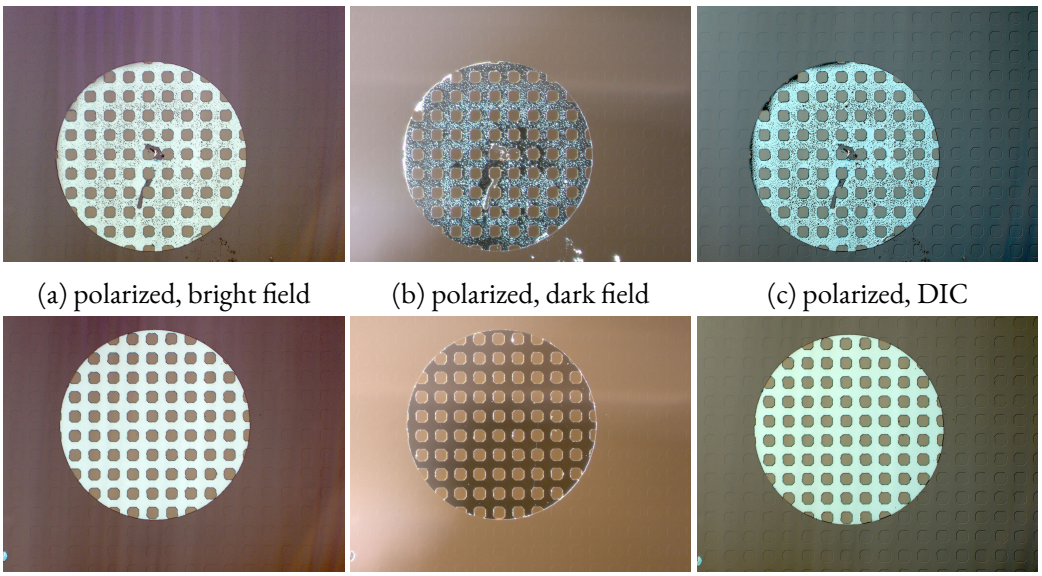

(a) polarized, bright field (b) polarized, dark field (c) polarized, DIC

(d) not polarized, bright field (e) not polarized, dark field (f) not polarized, DIC

Figure 4.34: Bright field images (4.34a and 4.34d), dark field images (4.34b and 4.34e), and differential interference contrast images (4.34c and 4.34f) of two microelectrodes (200 µm diameter) from the same sample. The electrode in the top row was polarized, while the one in the bottom row was subjected to the same atmosphere and temperature but not polarized. Measurements were taken in humidified hydrogen at 625 °C with anodic bias of up to 1200 mV applied.

## 4.5.2 Measurements in oxidizing atmospheres

### Cathodic Polarization

Figures 4.35 and 4.36 show impedance spectra of a microelectrode with a diameter of 200 µm, measured in synthetic air at 625 °C with polarization of up to −500 mV. Spectra with bias of up to −1200 mV are shown in figures 4.37 and 4.38. Spectra at bias voltages of up to −700 mV show the same three features which are a small depressed semicircle at high frequencies, a second medium sized semicircle at intermediate frequencies and a very large arc at very low frequencies. The latter belongs to a semicircle that could not be measured completely in a reasonable amount of measuring time, due to its low peak frequency.

In both experiments, spectra differ significantly from spectra measured in previous experiments, see section 4.2.1 and section 4.3.2. Firstly, the total electrode resistance is much higher. Secondly, spectra show an additional semicircle in the lower intermediate frequency range, which partly overlaps with the low frequency arc. With increasing bias voltage the dominant arc and the intermediate frequency semicircle decrease in size, whereas the small semicircle at high

frequencies doesn't change its appearance upon polarization. Furthermore, at higher bias voltages (over 700 mV) the former visible high frequency semicircle and the intermediate frequency shoulder are not distinguishable, only one slope feature remains at intermediate frequencies, and one dominant low frequency semicircle was observed.

At a first glance, one might suppose an additional serial process of the oxygen exchange reaction as origin of the additional semicircle. A preliminary analysis of the spectra with 3 serial R||CPE elements (see figure 4.39b), however, reveals that both capacitances $C_2$ and $C_3$ are very high, and typical for chemical capacitances. Furthermore, both capacitances show essentially identical bias dependencies, see figure 4.40. Based on these observations, an alternative explanation is suggested, which can explain all these observations.

As discussed in section 2.4.2, for LSF electrodes with bottom current collector geometry in oxidizing atmospheres spectra are expected to show one dominant low frequency semicircle caused by surface exchange resistance in parallel to the chemical capacitance, and a small semicircle caused by the interfacial resistance and capacitance in parallel at intermediate frequencies. However, this is only valid under several assumptions. Firstly, the electronic transport has to be fast. Secondly the surface exchange resistance has to be low compared to the lateral ionic transport resistance, but high compared to the across plane ionic transport resistance. These conditions are reported to apply to LSF [26]. Then, the LSF area above the current collector does not participate in the oxygen exchange.

However, if the surface exchange resistance is sufficiently high compared to the lateral ionic transport resistance, the equivalent circuit shown in figure 2.7b can no longer be simplified to that shown in figure 2.7d by ignoring the branch above the current collector. At high frequencies the circuit (see figure 4.39a) is short circuited by the capacitance of the current collector $C_{YSZ|Pt}$ and the interface capacitance $C_{LSF|YSZ}$. The electronic transport resistance $R_{eon}$ can be neglected, because of the high electron hole concentration and the presence of a current collector grid supporting the lateral electron distribution. With decreasing frequency, the right branch (B), above the substrate becomes active, whereas the left path (A), above the current collector is unfavorable because of the high ionic transport resistance $R_{ion}$. In both cases the high surface exchange resistance $R_{Surface}$ is shorted by the chemical capacitance(s) $C_{Chem}$. With further decrease of frequency, the impedance of the chemical capacitance(s) $C_{Chem}$ increases, causing the left branch (A) above the current collector to become more and more favorable, as the impedance of both branches is now dominated by the much high surface exchange resistance $R_{Surface}$. This causes larger and larger areas to be polarized until the whole electrode area is active. Therefore, in the spectra an additional semicircle appears. The overlap between the intermediate and low frequency semicircle represents the current redistribution from one branch (B) to both branches (A and B). Furthermore at more negative potentials the concentration of oxygen vacancies increases, therefore the ionic conductivity is expected to increase too. This causes the whole electrode area to be active towards oxygen exchange even at high frequencies as is the case in reducing atmospheres. Moreover, the concentration of electronic charge carriers decreases, thereby increasing the electronic transport resistance. A non negligible electronic resistance would cause a slope feature at intermediate frequencies, which indeed can be observed in the spectra.

Because of the complex spectra and interpretation of certain features, fitting was done with an equivalent circuit of 3 serial R||CPE elements and an offset resistance shown in 4.39b over

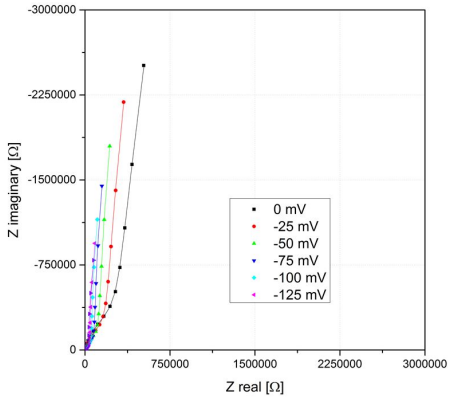


(a) 0 to −150 mV

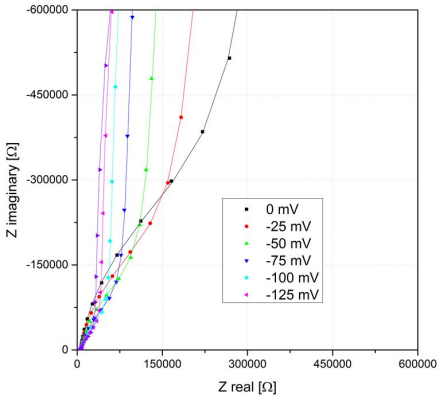


(b) 0 to −150 mV, zoom 1

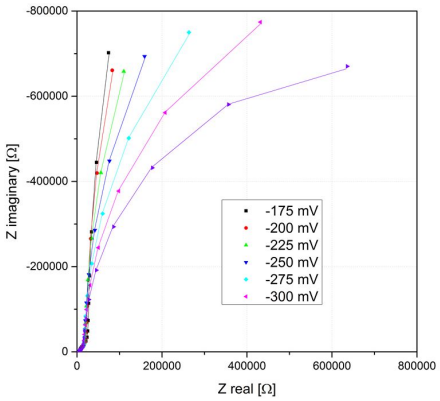


(c) −175 to −325 mV

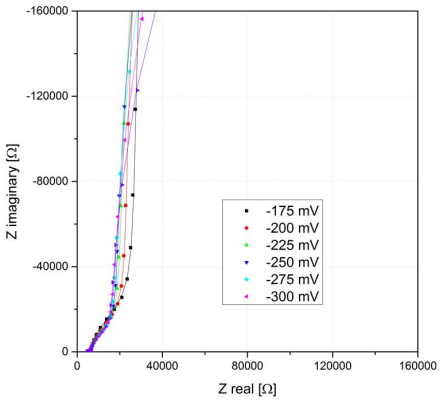


(d) −175 to −325 mV, zoom 1

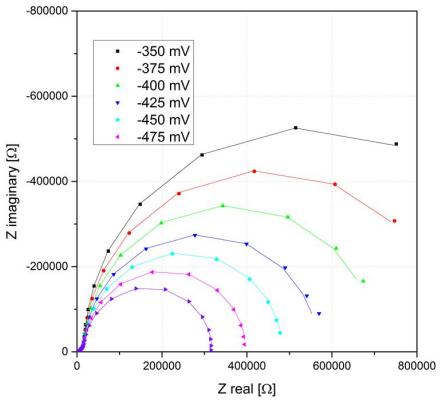


(e) 0.350 to −500 mV

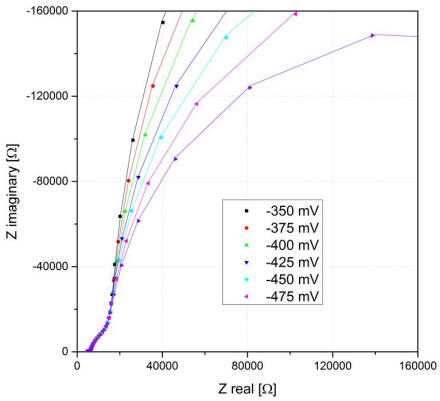


(f) −350 to −500 mV, zoom 1

Figure 4.35: Spectra of a microelectrode of 200 µm diameter measured in synthetic air at 625 °C under cathodic polarizaion. Figures 4.35a, 4.35c and 4.35e show the original spectra, figures 4.35b to 4.35f show magnifications.

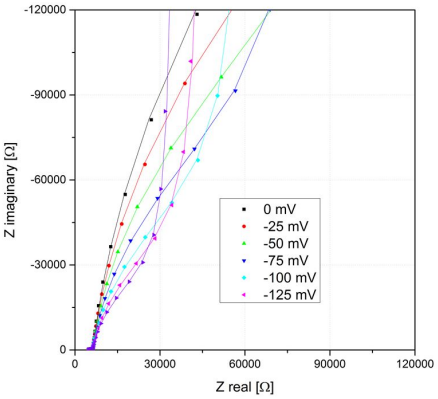


(a) 0 to −150 mV, zoom 2

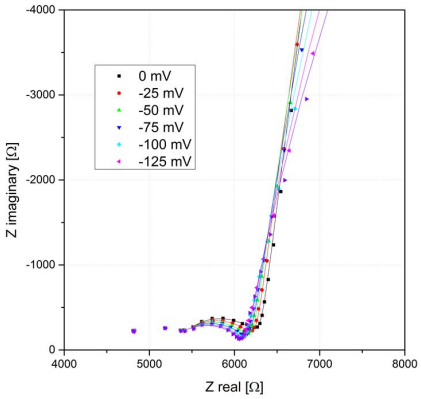


(b) 0 to −150 mV, zoom 3

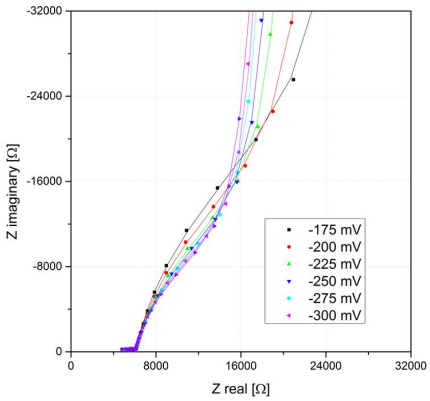


(c) −175 to −325 mV, zoom 2

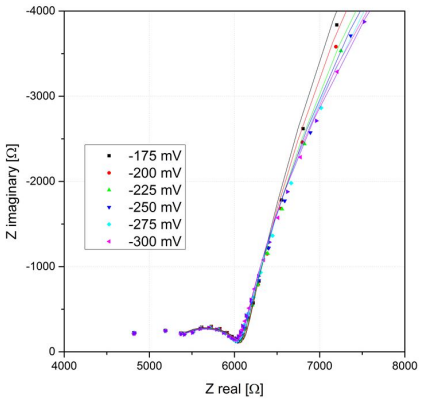


(d) −175 to −325 mV, zoom 3

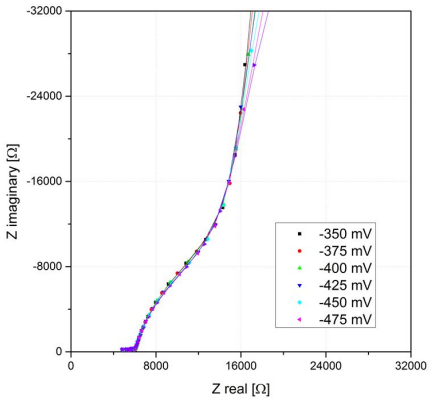


(e) −350 to −500 mV, zoom 2

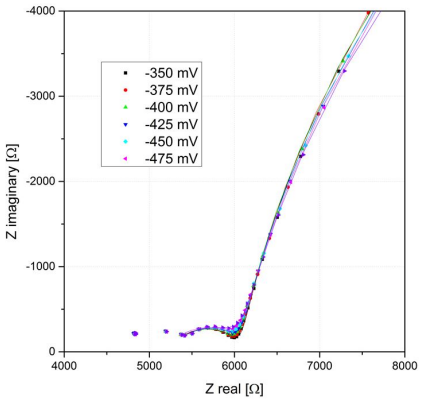


(f) −350 to −500 mV, zoom 3

Figure 4.36: Spectra of a 200 µm microelectrode measured in synthetic air at 625 °C under cathodic polarization. Figures 4.36a to 4.36e and 4.36b to 4.36f show different zoom levels of the spectra in 4.35.

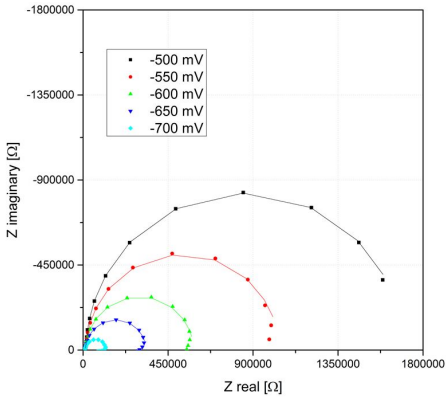


(a) −500 to −700 mV, original

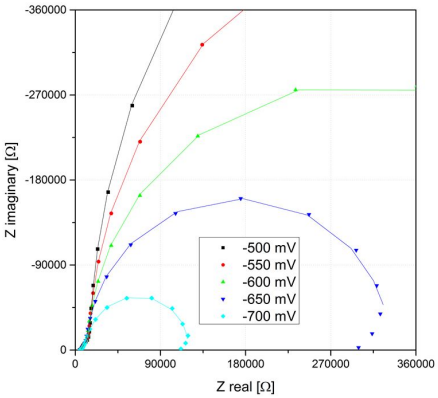


(b) −500 to −700 mV, zoom 1

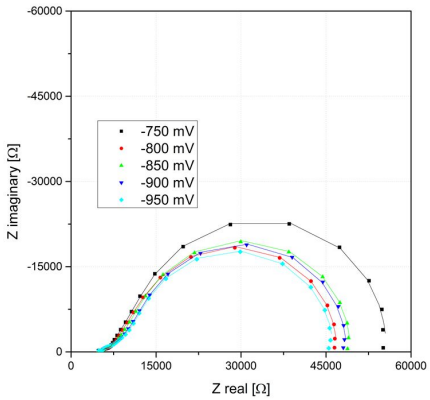


(c) −750 to −950 mV, original

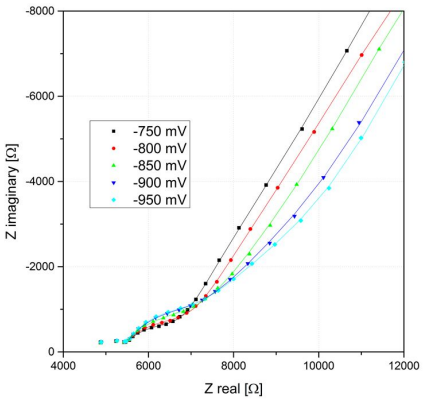


(d) −750 to −950 mV, zoom

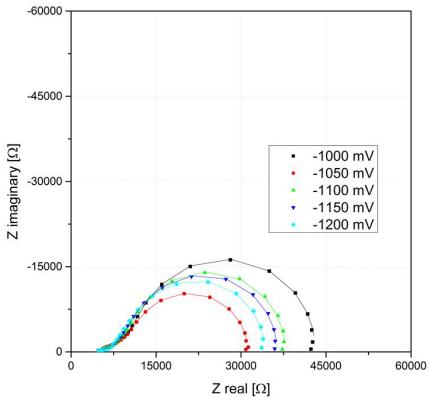


(e) −1 to −1.2 V, original

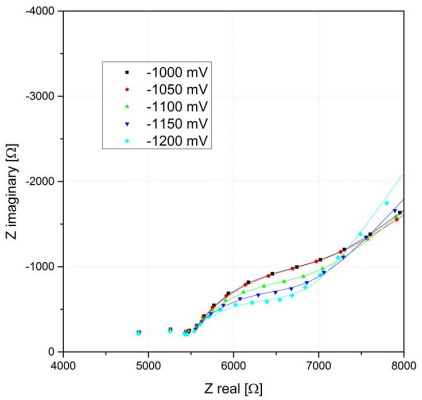


(f) −1 to −1.2 V, zoom 1

Figure 4.37: Spectra of a microelectrode of 200 µm diameter, measured in synthetic air at 625 °C under cathodic polarization. Figures 4.37a, 4.37c and 4.37e show the original spectra, the remaining spectra show magnifications.

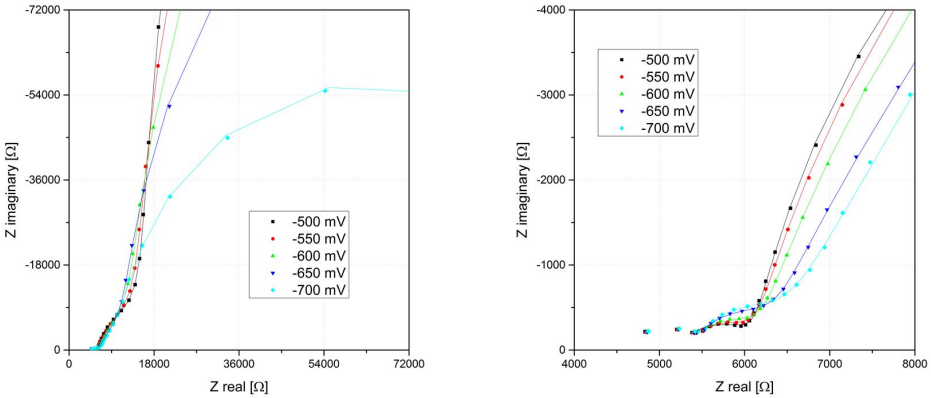


(a) −500 to −700 mV, zoom 2

(b) −500 to −700 mV, zoom 3

Figure 4.38: Spectra of a microelectrode (200 µm diameter) measured in synthetic air at 625 °C under cathodic polarization. Figures 4.38a and 4.38b show magnifications of the spectra in 4.37

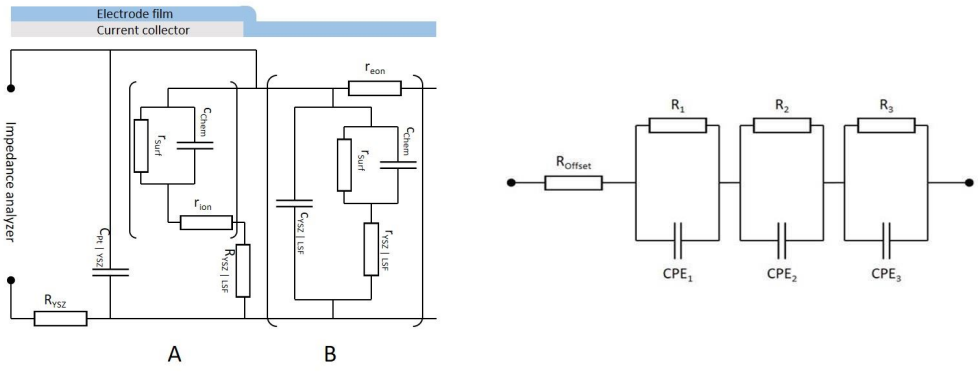


(a) General case

(b) Used for fitting

Figure 4.39: Equivalent circuit used for fitting in oxidizing atmospheres under cathodic polarization.

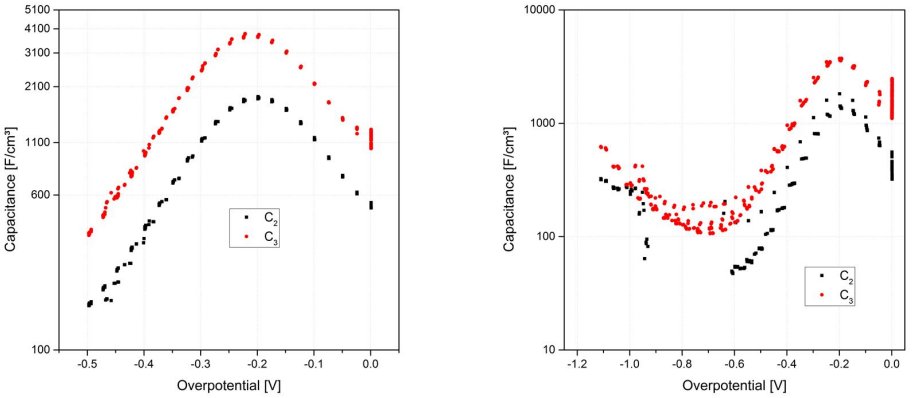


(a) 0 to −500 mV

(b) 0 to −1200 mV

Figure 4.40: Capacitances obtained from measurements on a microelectrode of 200 µm diameter, in synthetic air at 625 °C under cathodic polarization. An equivalent circuit of 3 serial R||CPE elements was used for fitting, and capacitances are normalized to the free electrode volume.

the entire frequency range. The resistance and the capacitance of the low frequency semicircle, which is attributed to the surface resistance in parallel to chemical capacitance, were used to calculate the surface exchange resistance and the chemical capacitance according to equations 4.3 and 4.4, assuming a fully polarized electrode ($f_V = 1$ and $f_A = 1$).

The chemical capacitance of the bias free spectra is in good agreement with the chemical capacitance measured on similar samples (microelectrodes with 200 µm diameter and bottom current collector) during the degradation experiments, see section 4.2. The surface exchange resistance, however, shows a drastic increase of one to two orders of magnitude compared to the measurements done during the degradation experiments. The progression of surface exchange resistance and chemical capacitance is shown in figure 4.41. As mentioned before, the surface exchange resistance is high, compared to samples measured earlier. Spectra under bias, and bias free spectra measured after every four bias spectra both show intense degradation within the first 4 cycles (bias of up to 500 mV). Again, the surface exchange resistance reversibly decreases with increasing bias. Upon the first application of higher bias voltages (up to 1200 mV), the surface exchange resistance drastically decreases for both bias free and bias measurements, and shows almost no further degradation over the following three cycles. Reduction of the surface resistance by polarization has been reported for other perovskite MIECs. [40] [41]

As described in section 4.6 this unusually high surface resistance is caused by contamination or irreversible changes to the electrode surface during microstructuring of the LSF film. Therefore, reasonable measurements on kinetic properties of LSF in its initial state are not possible on microelectrodes. However, the high surface exchange resistance offers an advantage for investigations on the chemical capacitance. As described above, for moderate surface exchange resistances at high oxygen partial pressures only the area between the current collector grid is active, as the high lateral ionic transport resistance hinders any current flow over the current collector. In reducing conditions, however, the whole electrode is active due to the low ionic

transport resistance. Therefore, when polarizing cathodically at some point larger and larger areas of the sample will become active, thereby preventing normalization to the active electrode volume. However, as due to the high surface exchange resistance the whole electrode is active at all potentials, experiments for determining the chemical capacitance can be done even at potentials where normally a change of active area is to be expected.

Reproducible results were obtained for the chemical capacitance over the course of the first 4 cycles, with bias up to 500 mV. Within the following three cycles (up to 1200 mV bias), the chemical capacitance is still quite reproducible, but strong scattering is found for bias free measurements.

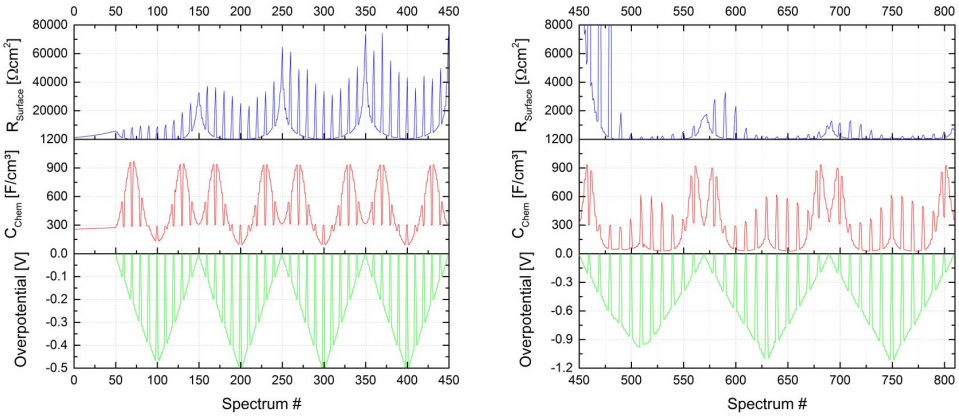


(a) Up to 500 mV cathodic bias (b) Up to 1200 mV cathodic bias

Figure 4.41: Progression of surface exchange resistance and chemical capacitance of a microelectrode (200 µm diameter) measured in synthetic air at 625 °C. The left plot shows 4 bias cycles of up to 500 mV cathodic bias, the right shows 3 consecutive bias cycles of up to 1200 mV, measured immediately after the first 4 cycles, on the same electrode.

In figure 4.42 the chemical capacitance is plotted versus the electrode overpotential, in a half logarithmic plot. During the first 4 cycles with up to 500 mV bias, the chemical capacitance is excellently reproducible. Upon application of up to 1200 mV bias, aside from the first cycle, the chemical capacitance is again very stable, indicating some irreversible effects taking place upon the first application of higher bias voltages, where also the surface resistance drastically decreases. Beginning at bias free conditions and going to more negative potentials, the chemical capacitance increases until reaching a maximum at around −200 mV. Afterward it decreases until reaching a minimum at around −750 mV. At more negative potentials the chemical capacitance first shows a shallow increase, a bend at about −1000 mV followed by a slightly steeper increase. The general characteristics fit the expectations, with regards to the Brouwer diagram. Under bias free conditions, ionic charge carriers (oxygen vacancies) are the minority charge carriers, and thus dominate the chemical capacitance. With more negative potentials the concentration of vacancies increases, causing also the chemical capacitance to increase. At around −250 mV the concentration of vacancies exceeds the electron hole concentration. Therefore the electronic charge carriers (almost exclusively electron holes at these conditions) become minority charge

carriers and thus dominate the chemical capacitance. As the electron hole concentration decreases, so does the chemical capacitance with more negative potentials. At around −700 mV the concentration of electron holes equals the concentration of electrons. Thus the total concentration of electronic charge carriers reaches a minimum, which also causes a minimum of the chemical capacitance. At even more negative potentials the chemical capacitance increases again as the concentration of electrons keeps increasing. In the regions from −1200 to −1000 mV, −900 to −750 mV, −600 to −250 and −150 to 0 mV, the $C_{Chem}$ versus overpotential curves were fitted using an exponential fit (equation 4.7). This yielded average slopes of -7.1, -3.3, 10.1 and -7.1 for the respective sections, versus the electrode overpotential. These slopes correspond to -0.14, -0.06, 0.19, -0.14 versus logarithmic oxygen partial pressure. This is shallower than expected from the defect model based on thermogravimetry and coulometric titration by Kuhn et. al. [17] (-0.24, 0.24 and 0.46). The bend at 1000 mV is not expected from the defect model at all.

Microscopic images of the electrodes, taken after the EIS measurement showed no alterations of electrode appearance, see figures 4.43 and 4.44. Compared to non measured electrode from the same sample, the one subjected to 1200 mV bias showed a slight darkening of the electrode, especially in the area between the current collector grid. A small spot near the center of the electrode where the contacting needle was placed appears slightly brighter. The electrode subjected to no more than 500 mV of cathodic bias showed no visible changes aside from a scratch which was caused by the needle in the contacting process. This darkening of the electrode was also observed on cathodically polarized electrodes in humidified hydrogen, but already at 500 mV bias. In addition to the vast decrease of the surface resistance and the slightly different chemical capacitances within the first 1200 mV bias cycle this leads to the conclusion that such a negative potential, be it induced by atmosphere or by application of voltage, leads to permanent changes of the electrode.

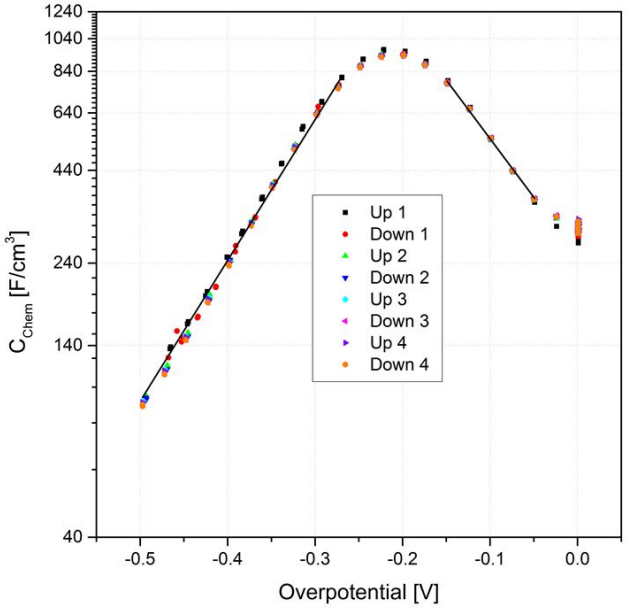


(a) Up to −500 mV bias

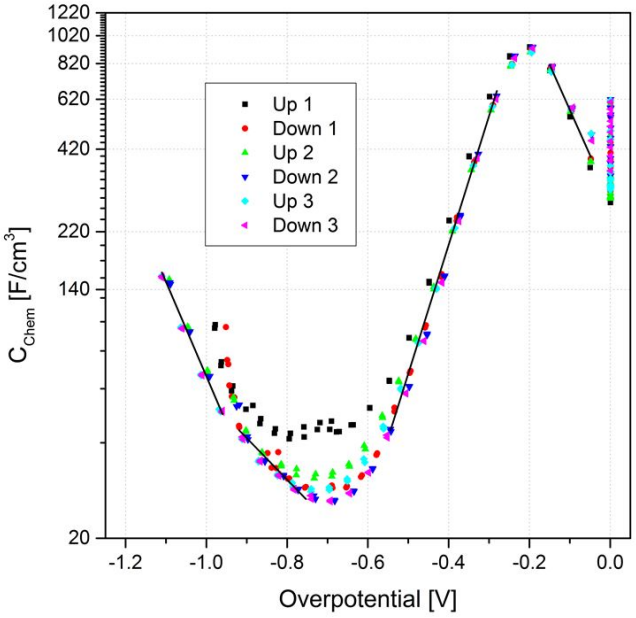


(b) Up to −1200 mV bias

Figure 4.42: Chemical capacitance versus electrode overpotential with set bias voltages from 0 to −500 mV (Figure 4.42a) and from 0 to −1200 mV (Figure 4.42a), measured on a 200 µm microelectrode with bottom current collector in synthetic air at 625 °C.

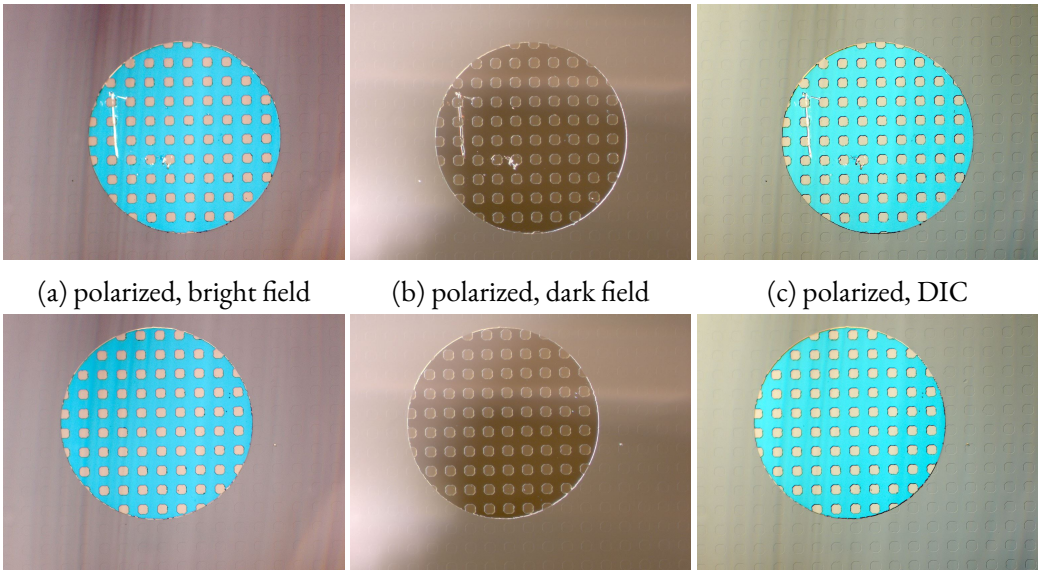

(a) polarized, bright field (b) polarized, dark field (c) polarized, DIC

(d) not polarized, bright field (e) not polarized, dark field (f) not polarized, DIC

Figure 4.43: Bright field images (4.43a and 4.43d), dark field images (4.43b and 4.43e), and differential interference contrast images (4.43c and 4.43f) of two microelectrodes (200 µm diameter) from the same sample. The electrode in the top row was polarized, while the one in the bottom row was subjected to the same atmosphere and temperature but not polarized. Measurements were taken in synthetic air at 625 °C with cathodic bias of up to 500 mV applied.

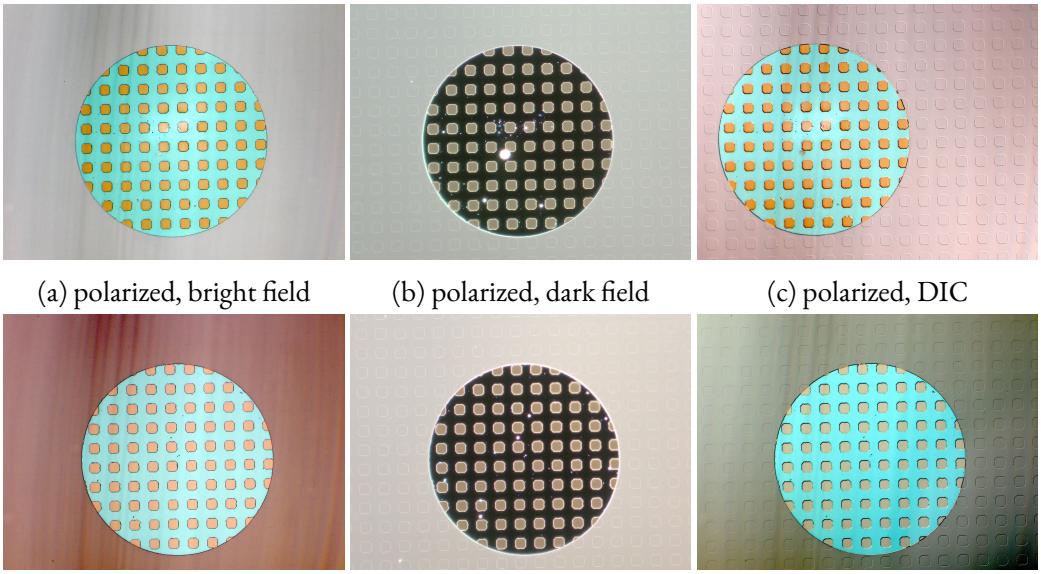

(a) polarized, bright field (b) polarized, dark field (c) polarized, DIC

(d) not polarized, bright field (e) not polarized, dark field (f) not polarized, DIC

Figure 4.44: Bright field images (4.44a and 4.44d), dark field images (4.44b and 4.44e), and differential interference contrast images (4.44c and 4.44f) of two microelectrodes (200 µm diameter) from the same sample. The electrode in the top row was polarized, while the one in the bottom row was subjected to the same atmosphere and temperature but not polarized. Measurements were taken in synthetic air at 625 °C with cathodic bias of up to 1200 mV applied.

Variation of oxygen partial pressure

In addition to measurements in synthetic air, experiments were also done in mixtures of 0.1 %, 1 % and 100 % oxygen in nitrogen. These percentages correspond to oxygen partial pressures of $1.013 \times 10^{-3}$ bar, $1.013 \times 10^{-2}$ bar and 1.013 bar. Figures 4.45 to 4.48 show the corresponding impedance spectra. All spectra are of the same general appearance as the ones measured in synthetic air. Again, the surface resistance is very high, causing an additional feature, as described in the beginning of section 4.5.2.

Spectra were fitted using an equivalent circuit of three R||CPE elements and an offset resistance in series (figure 4.39), from which surface exchange resistance and chemical capacitance were calculated using equations 4.3 to 4.4, assuming a fully polarized electrode ($f_A = 1$ and $f_V = 1$). This yielded the following progression of surface resistance and chemical capacitance over several bias cycles, see figure 4.49. In all cases, the surface resistance is extremely high, and in 1 % oxygen increases with time even further. The chemical capacitance on the other hand is very stable over the course of several cycles. Figures 4.49b to 4.49f show the chemical capacitance plotted versus the overpotential at the respective partial pressures. All three curves show a very similar appearance but are shifted on the potential axis. The maximum of the chemical capacitance is very similar to that measured in synthetic air.

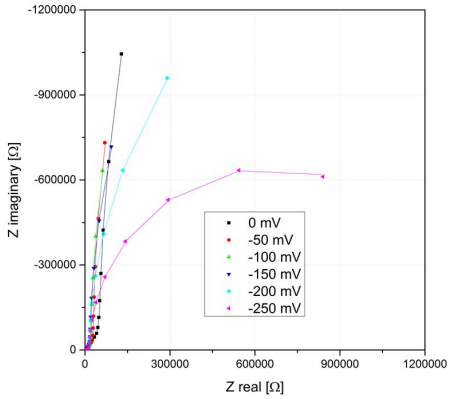


(a) 0.1 % oxygen

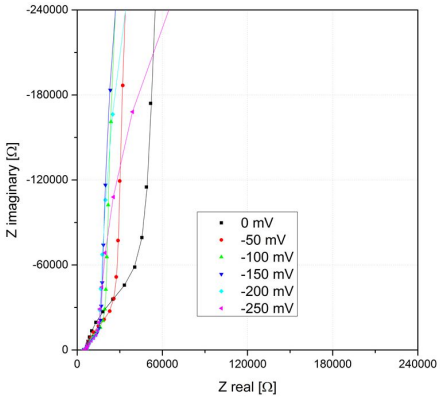


(b) 0.1 % oxygen, zoom 1

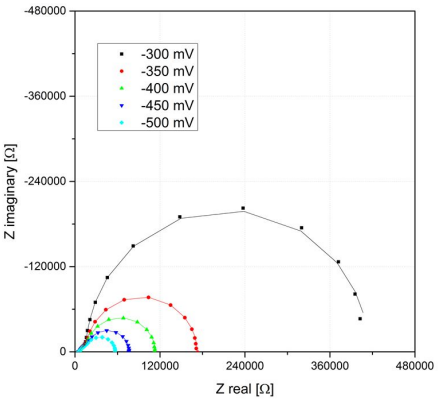


(c) 0.1 % oxygen

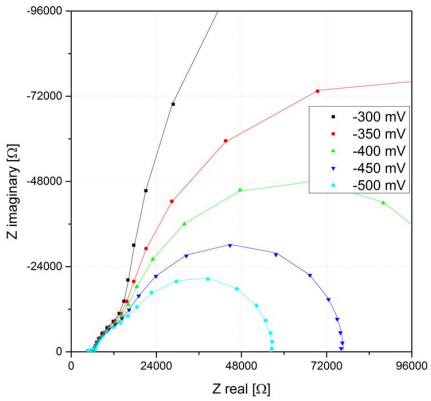


(d) 0.1 % oxygen, zoom 1

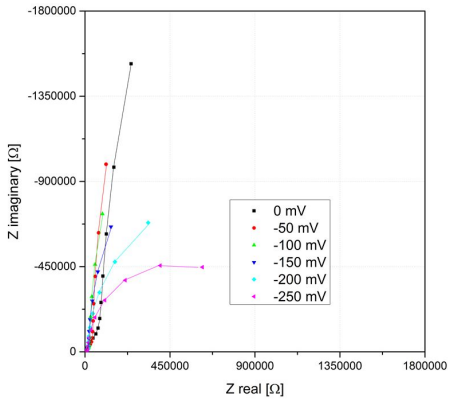


(e) 1 % oxygen

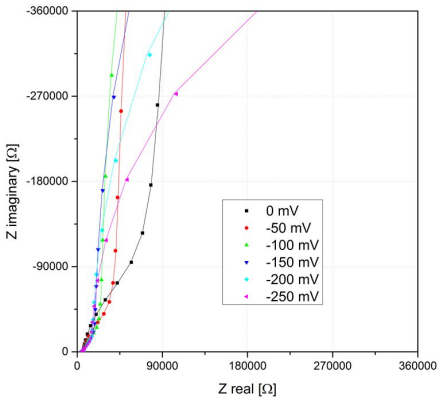


(f) 1 % oxygen, zoom 1

Figure 4.45: Spectra of microelectrodes (200 µm diameter) measured at 625 °C. 0.1 % oxygen (Figures 4.45a to 4.45d) and 1 % oxygen (Figures 4.45e and 4.45f). Entire spectra (left) and magnifications (right).

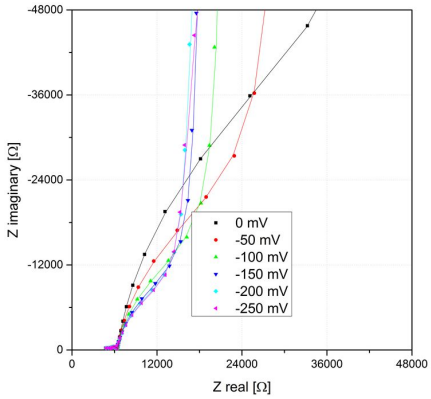


(a) 0.1 % oxygen, zoom 2

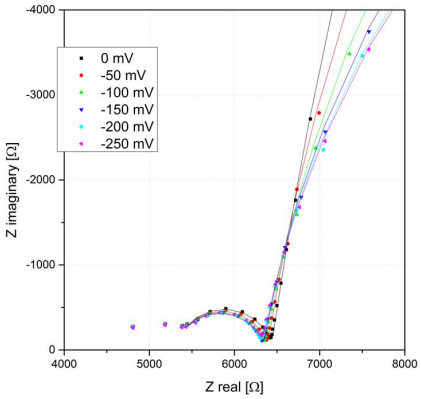


(b) 0.1 % oxygen, zoom 3

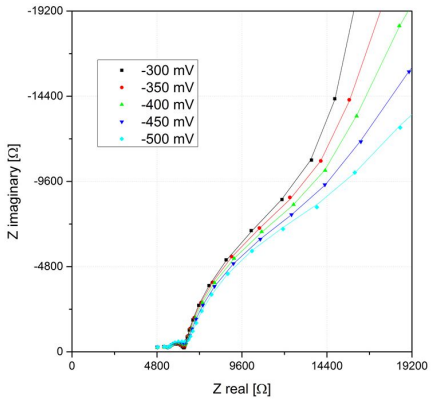


(c) 0.1 % oxygen, zoom 2

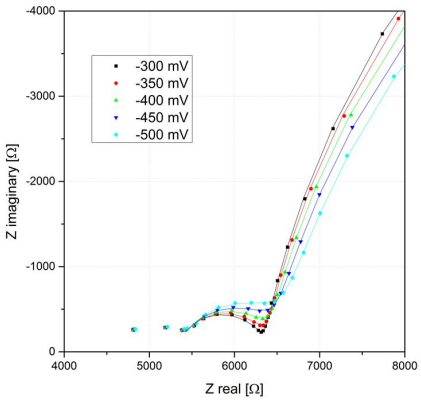


(d) 0.1 % oxygen, zoom 3

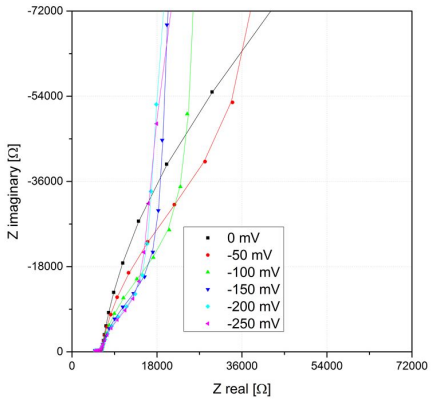


(e) 1 % oxygen, zoom 2

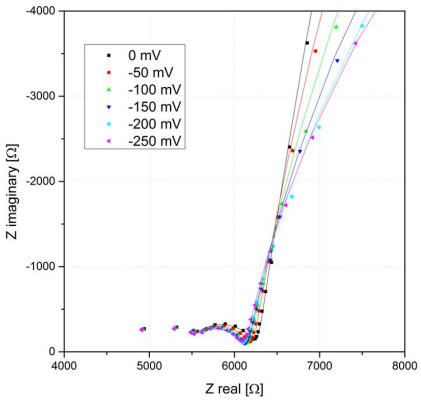


(f) 1 % oxygen, zoom 3

Figure 4.46: Spectra of microelectrodes (200 µm diameter) measured at 625 °C. 0.1 % oxygen (Figures 4.46a to 4.46d) and 1 % oxygen (Figures 4.46e and 4.46f). Further magnifications of the spectra shown in figure 4.45.

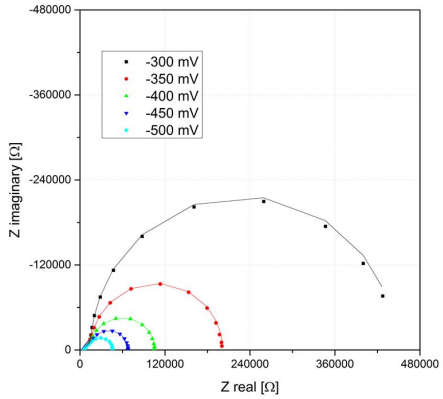


(a) 1 % oxygen

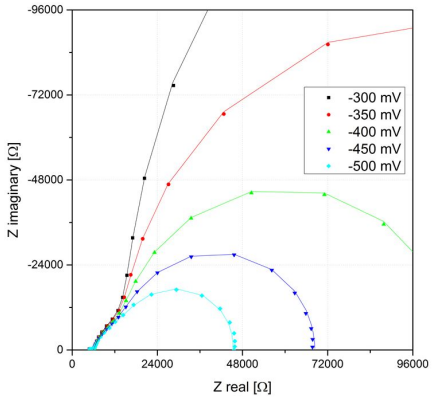


(b) 1 % oxygen, zoom 1

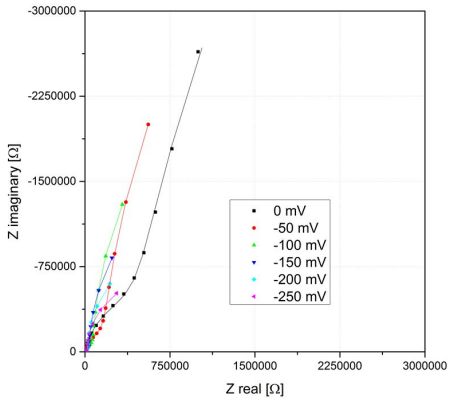


(c) 100 % oxygen

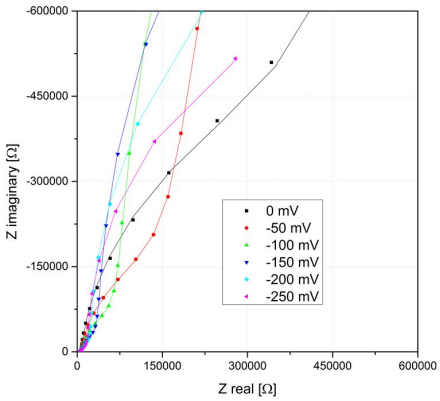


(d) 100 % oxygen, zoom 1

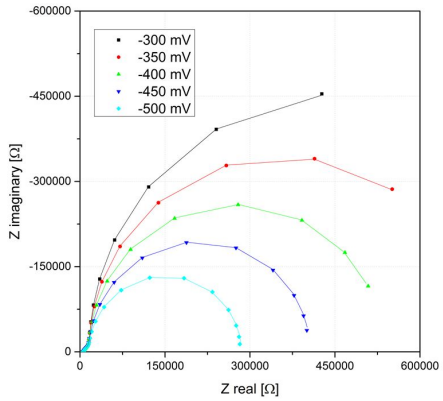


(e) 100 % oxygen

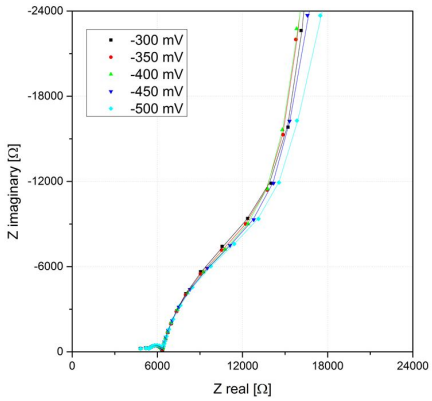


(f) 100 % oxygen, zoom 1

Figure 4.47: Spectra of microelectrodes (200 µm diameter) measured at 625 °C. 1 % oxygen (Figures 4.47a and 4.47b) and 100 % oxygen (Figures 4.47c to 4.47f). Entire spectra (left) and magnifications (right).

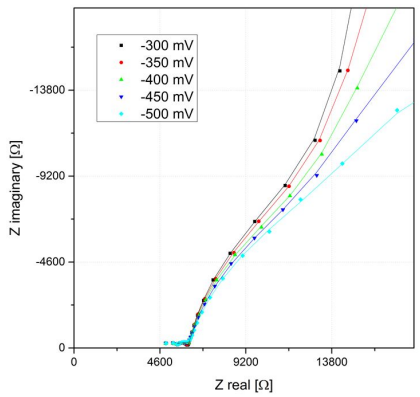


(a) 1 % oxygen, zoom 2

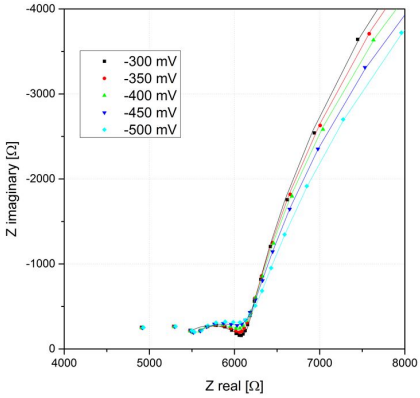


(b) 1 % oxygen, zoom 3

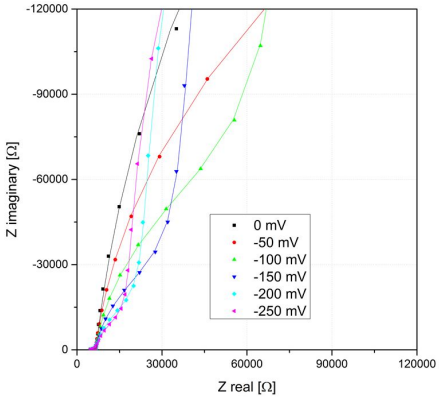


(c) 100 % oxygen, zoom 2

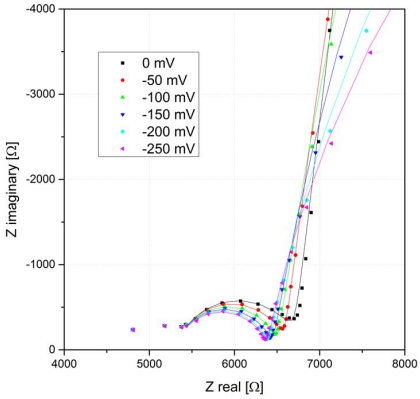


(d) 100 % oxygen, zoom 3

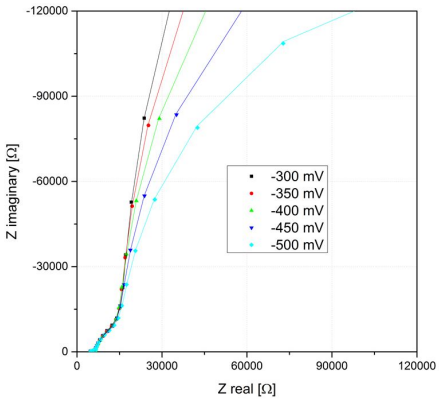


(e) 100 % oxygen, zoom 2

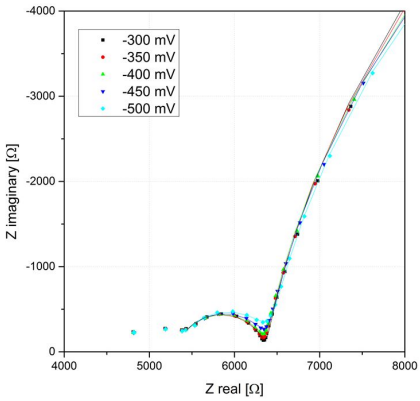


(f) 100 % oxygen, zoom 3

Figure 4.48: Spectra of microelectrodes (200 µm diameter) measured at 625 °C. 1 % oxygen (Figures 4.48a and 4.48b) and 100 % oxygen (Figures 4.48c to 4.48f). Further magnifications of the spectra shown in figure 4.47.

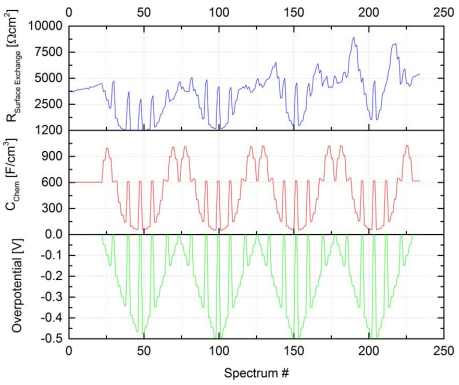


(a) 0.1 % Oxygen

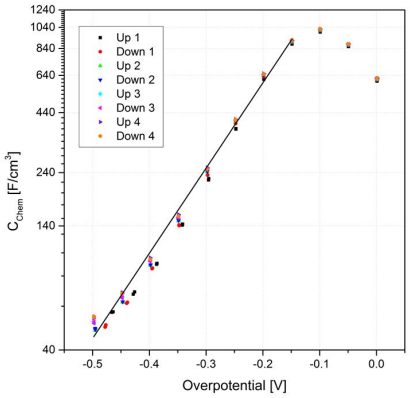


(b) 0.1 % Oxygen

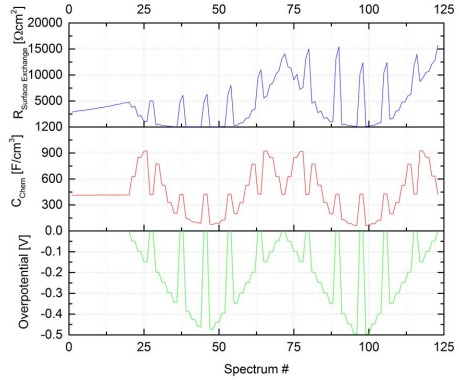


(c) 1 % Oxygen

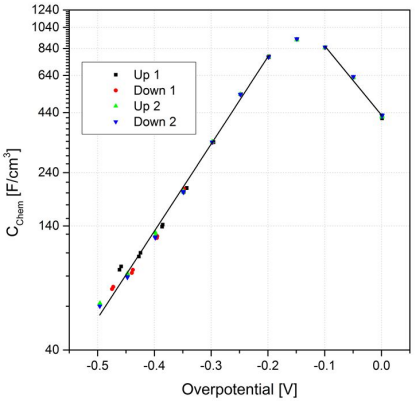


(d) 1 % Oxygen

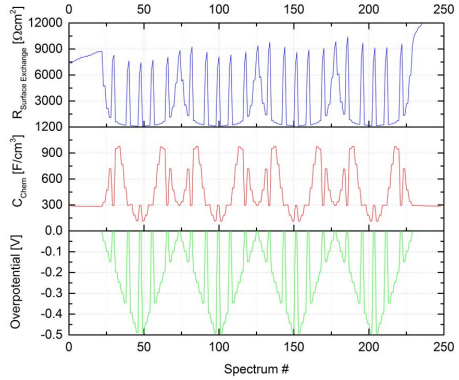


(e) 100 % Oxygen

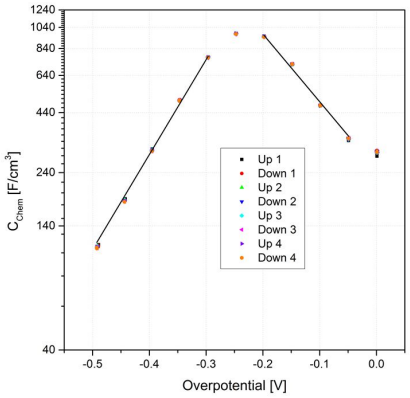


(f) 100 % Oxygen

Figure 4.49: Left: Progression of surface exchange resistance, chemical capacitance and electrode overpotential over the course of several bias cycles. Right: Chemical capacitance versus the electrode overpotential. Measurements were taken on microelectrodes of 200 µm diameter at 625 °C at different oxygen partial pressures.

### 4.5.3 Comparison of different atmospheres

According to Nernst's equation, for each experiment the equivalent oxygen partial pressure, the potential versus synthetic air and the potential versus humid hydrogen were calculated based on actual electrode overpotential and oxygen partial pressure, see equations 4.8 to 4.10.

$$\eta_{\text{vs. synthetic air}} = \eta_{\text{actual}} + \frac{R \times T}{z \times F} \times ln\left(\frac{0.21 \quad bar}{p\,(O_2)_{actual}}\right) \tag{4.8}$$

$$\eta_{\text{vs. humidified hydrogen}} = \eta_{\text{actual}} + \frac{R \times T}{z \times F} \times ln\left(\frac{9.5 \times 10^{-24} \quad bar}{p\,(O_2)_{actual}}\right) \tag{4.9}$$

$$p\,(O_2)_{equivalent} = p\,(O_2)_{actual} \times e^{\frac{z \times F}{R \times T} \times \eta actual} \tag{4.10}$$

The chemical capacitance was then plotted versus the equivalent partial pressure, to compare the $C_{Chem}$ versus overpotential curves of the individual experiments in different atmospheres, see figure 4.50. The experiments in oxidizing atmospheres exhibit a perfect match of the chemical capacitance versus overpotential curves measured at different oxygen partial pressures. Therefore the defect chemistry in the material can be influenced by a voltage independent of the outer chemical potential (oxygen partial pressure) and vice versa.

While the slopes of of theses $C_{Chem}$ versus $\eta$ curves are shallower than expected from the defect model, they are consistent with slopes obtained in experiments in reducing atmosphere. For most negative potentials from −1200 to −1000 mV a slope of -0.14 has been determined. These potentials correspond to cathodic bias when polarizing in humidified hydrogen, where slopes of -0.19 and -0.15 were found. In the area from −900 to −750 mV a slope of -0.06 was found, which is comparable to the slope of -0.07 observed in reducing atmosphere under anodic polarization. At more positive potentials, from −600 −250mV, the slope was calculated to 0.19. Under the corresponding anodic polarization in humidified hydrogen, a slope of 0.21 was determined.

Measurements done in reducing atmosphere with anodic bias show small deviations from measurements done in synthetic air, mostly because of the drift of the chemical capacitance in reducing atmosphere. While the first cycles in reducing atmosphere yielded a lower chemical capacitance than measurements in synthetic air, this differences diminish over the course of several cycles. The quantitative values from measurements in reducing atmospheres with cathodic bias are significantly lower than extrapolation from anodic polarization measurements in reducing atmosphere and cathodic polarization measurements in oxidizing atmosphere would suggest. However such negative potentials are outside the stability limit of LSF, [17]. Nevertheless, the slope of the curves is still comparable.

Finally, the measured $C_{Chem}$ versus partial pressure curves are quantitatively compared to the ones calculated from bulk defect chemical data, see section 2.2.2. The position of maximum and minimum fit quite well, despite a slight shift of the minimum to more reducing conditions for the calculated curve. Keeping in mind that calculations are based on bulk data, whereas measurements were done on thin films, differences are not unlikely. There are several differences between thin film and bulk samples which might cause lower values for thin film chemical capacitance. Firstly, stress or strain can be induced in the thin film due to different thermal expansion coefficients. Secondly, a strong bonding between substrate and thin film can also cause

stress because of different lattice parameters, or because of the chemical expansion of the thin film during oxygen release [17]. Furthermore, PLD grown thin films have much smaller grains (about 50 nm, [25]. Therefore grain boundaries, which most likely have different properties than the bulk, make up a larger fraction of the material. Preferred growth orientations might also cause different chemical capacitances.

More surprisingly are partly strong deviations of the absolute values with differences becoming large for large values of the chemical capacitance. These deviations are most probably not caused by the difference of bulk and thin film since the same maximum chemical capacitance is expected for all defect chemical data. As shown in section 2.2.2, the maximum chemical capacitance is a function of the dopant concentration alone, see equation 2.17. Reasons for these deviations are yet unknown, and a detailed investigation is beyond the scope of this work. For the related perovskite oxide $La_{1-x}Sr_xCoO_{3-\delta}$ Kawada et. al. also found that the chemical capacitance was lower in thin film electrodes compared to bulk data. [30]

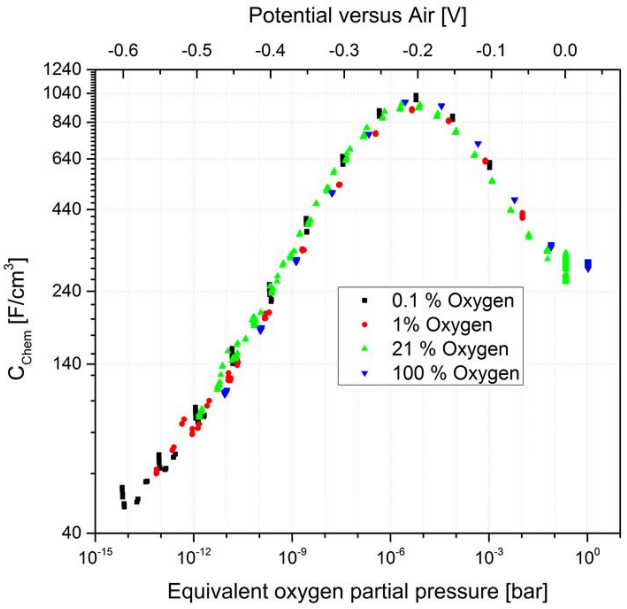


(a) 0.1 to 100 % Oxygen

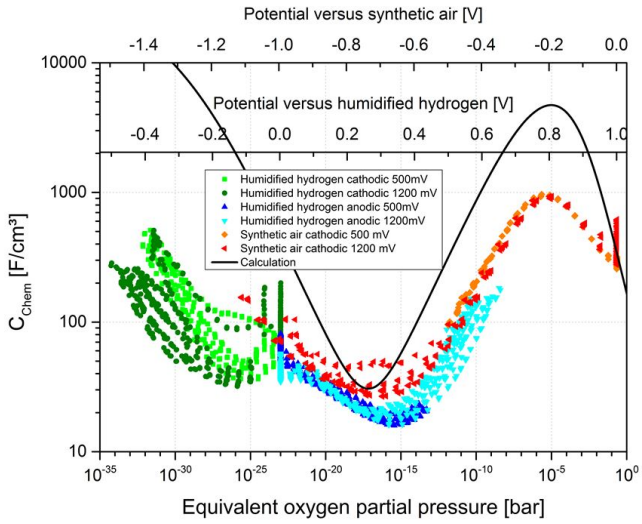


(b) Humidified hydrogen and synthetic air

Figure 4.50: Comparison of chemical capacitance measured in different atmospheres, versus the equivalent partial pressure corresponding to the actual electrode overpotential. Measurements were done at 625 °C on microelectrodes of 200 µm diameter.

## 4.6 Investigation of the surface resistance

To ascertain the origin of the unexpectedly high surface resistance encountered during the second set of bias experiments, sample preparation and measurement parameters were varied. A comparison of these samples, and samples from the degradation experiments (section 4.2), is shown in table 4.2.

Possible influences of the measurement apparatus or the target used for PLD deposition could be ruled out, as variation of these parameters does not lead to differences in surface exchange resistance. Moreover, macroelectrodes with bottom current collector consistently show surface resistances of about $(3 \pm 1)\,\Omega\,\mathrm{cm}^2$. Values in this order of magnitude are also found in literature. [25]

Microelectrodes show surface resistances of either about $(63 \pm 15)\,\Omega\,\mathrm{cm}^2$ or over $500\,\Omega\,\mathrm{cm}^2$, regardless of current collector placement. No correlation is found between the vastly degraded microelectrodes and sample preparation or measurement conditions. It is therefore conceivable, that microstructuring of the electrodes alters the oxygen surface exchange kinetics by one or over two orders of magnitude.

Measurements done on microelectrodes which were prepared from previously measured macroelectrodes show an increase of the surface exchange resistance from $(3 \pm 1)\,\Omega\,\mathrm{cm}^2$ to $(70 \pm 18)\,\Omega\,\mathrm{cm}^2$, supporting this assumption. Furthermore measurements on macroelectrodes with top current collector also yielded surface resistances of either about $60\,\Omega\,\mathrm{cm}^2$ and over $500\,\Omega\,\mathrm{cm}^2$. This again suggests the lithography as crucial step, as these electrodes were also subjected to lithography, whereas electrodes with bottom current collector, being deposited onto the grid, never came in contact with the photolithography process.

In addition, XPS measurements were done on three samples, one macroelectrode with bottom current collector, one microelectrode with a surface exchange resistance of $60\,\Omega\,\mathrm{cm}^2$ and one microelectrode with a surface exchange resistance of $500\,\Omega\,\mathrm{cm}^2$. While chromium and platinum are present on two of three samples each, no correlation with sample preparation or measurement conditions could be found. Additionally, on the two microelectrodes large amounts of sodium were found, again confirming the lithography as factor of influence regarding contamination.

Since microelectrodes were shown to exhibit unpredictable surface exchange resistance, reproducible measurements of kinetic properties was not possible on microelectrodes. Therefore, additional on macroelectrode measurements with three electrode geometry were done, see section 4.7.

| PLD-Target | Current-collector | Size | Measurement apparatus | Counter-electrode | Surface Resistance |
|---|---|---|---|---|---|
| Target 2 | Bottom | Macro | Athene | Symmetric | 2.1 Ω cm$^2$ |
| Target 1 | Bottom | Macro | Nemesis | symmetric | 2.3 Ω cm$^2$ |
| Target 2 | Bottom | Macro | Athene | Symmetric | 3.4 Ω cm$^2$ |
| Target 2 | Bottom | Macro | Athene | Symmetric | 3.5 Ω cm$^2$ |
| Target 2 | Bottom | Macro | Morpheus | Symmetric | 4.3 Ω cm$^2$ |
| Target 2 | Bottom | Macro | Athene | Symmetric | 4.4 Ω cm$^2$ |
| Target 1 | Top | 200 µm | Nemesis | Porous Pt | 45 Ω cm$^2$ |
| Target 1 | Bottom | 200 µm | Nemesis | Porous Pt | 47 Ω cm$^2$ |
| Target 2 | Top | Macro | Athene | Symmetric | 60 Ω cm$^2$ |
| Target 2 | Bottom | 200 µm* | Athene | LSF film | 60 Ω cm$^2$ |
| Target 2 | Bottom | 200 µm* | Athene | LSF film | 62 Ω cm$^2$ |
| Target 2 | Bottom | 200 µm | Athene | LSF film | 62 Ω cm$^2$ |
| Target 2 | Bottom | 200 µm* | Athene | LSF film | 63 Ω cm$^2$ |
| Target 2 | Bottom | 200 µm | Nemesis | LSF film | 69 Ω cm$^2$ |
| Target 2 | Bottom | 200 µm* | Athene | LSF film | 98 Ω cm$^2$ |
| Target 1 | Bottom | 200 µm | Morpheus | Porous LSF/Pt | >500 Ω cm$^2$ |
| Target 1 | None | 200 µm | Morpheus | Porous LSF/Pt | >500 Ω cm$^2$ |
| Target 1 | None | 200 µm | Morpheus | Porous LSF/Pt | >500 Ω cm$^2$ |
| Target 2 | Bottom | 200 µm | Morpheus | LSF film | >500 Ω cm$^2$ |
| Target 2 | Bottom | 200 µm | Nemesis | LSF film | >500 Ω cm$^2$ |
| Target 2 | Top | Macro | Athene | Symmetric | >500 Ω cm$^2$ |

Table 4.2: Comparison of the surface exchange resistance of various samples with different parameters. * Measurements done on microelectrode prepared from previously measured macroelectrodes. All measurements were done at 625 °C in synthetic air.

## 4.7 3-point measurements

### 4.7.1 Experiments in synthetic air

As described in section 3.1.6, samples with three electrode geometry consist of two similar macro electrodes, working electrode (WE) and counter electrode(CE), on either side of the substrate and a ring electrode of porous platinum around the circumference, the reference electrode (RE). Therefore the distinction between working and counter electrode is only nominal.

In a first experiment measurements were done in synthetic air at 625 °C under set bias voltages of ±600 mV between working and counter electrode. Both working and counter electrode were measured against the reference electrode (3-point measurement) and against each other (2-point measurement). This was done in order to rule out parasitic current paths to the reference electrode. Figures 4.51 and 4.52 show spectra of working and counter electrode measured against each other and versus the reference electrode.

Shapes of spectra measured between working and counter electrode are similar to previous measurements on symmetric macroelectrodes. They exhibit a high frequency offset, attributed to the electrolyte, a shoulder at intermediate frequencies, and a dominant semicircle at low frequencies, which is attributed to the surface exchange resistance and the chemical capacitance. The size of the dominant semicircle decreases and gets more and more depressed under polarization. Because of different surface exchange resistances under anodic and cathodic polarization the peak frequency of each electrode changes differently, thus causing a depressed semicircle in the impedance spectra.

When measured versus the reference electrode, both electrodes exhibit new features in the intermediate frequency region. The counter electrode shows a loop at the onset of the dominant semicircle instead of the former visible shoulder. The working electrode shows an increase in the size of this shoulder, which changes into a separate semicircle under cathodic polarization.

To check for potential parasitic current paths over the reference electrode, for each set bias value the spectra of working electrode versus reference electrode and counter electrode versus reference electrode were summed up according to equation 4.11 and compared with the spectra of counter electrode versus working electrode at the respective set bias. As shown in figures 4.53a and 4.53b for some exemplary spectra, the calculated sum spectra and the measured spectra agree within minor deviation of about 0 to 5 %, which can also be caused by degradation of the electrodes between individual measurements.

$$Z_{WE-CE}(\omega) = Z_{WE-RE}(\omega) + Z_{CE-RE}(\omega) \tag{4.11}$$

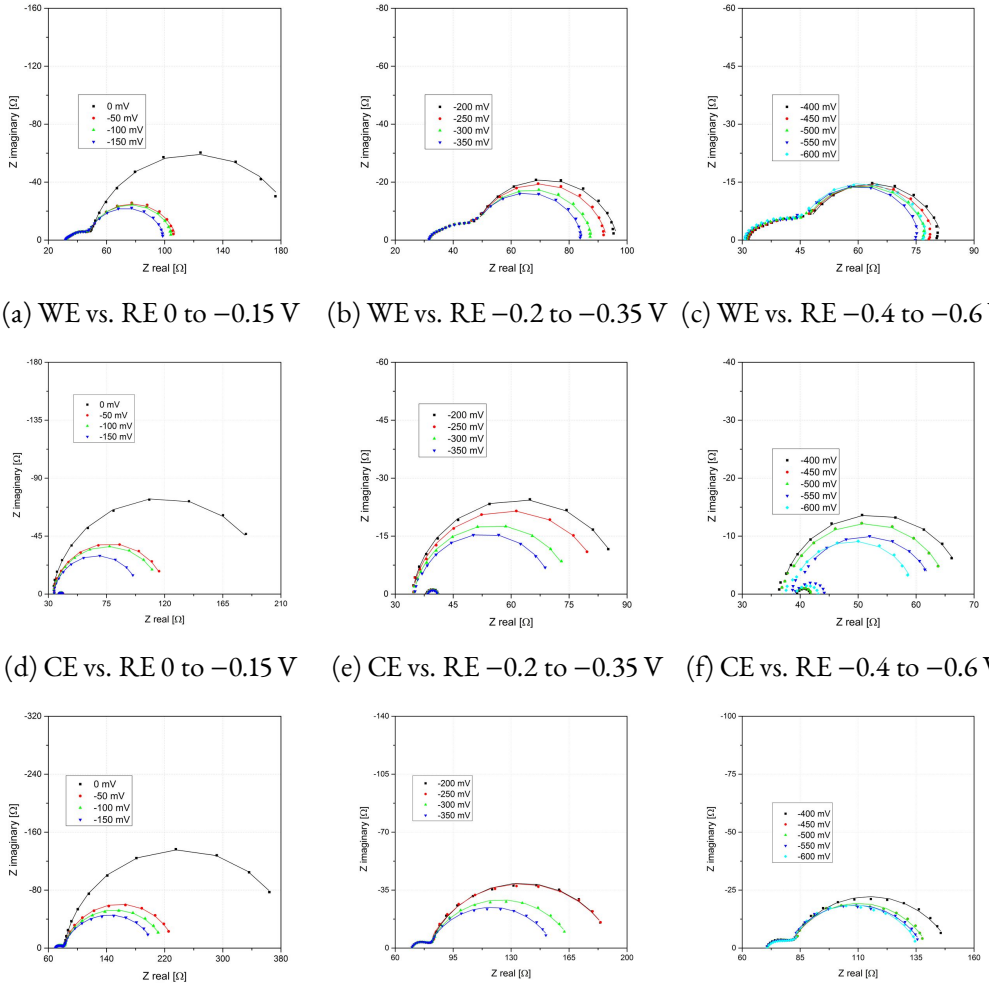


(a) WE vs. RE 0 to −0.15 V (b) WE vs. RE −0.2 to −0.35 V (c) WE vs. RE −0.4 to −0.6 V

(d) CE vs. RE 0 to −0.15 V (e) CE vs. RE −0.2 to −0.35 V (f) CE vs. RE −0.4 to −0.6 V

(g) WE vs. CE 0 to −0.15 V (h) WE vs. CE −0.2 to −0.3 V (i) WE vs. CE −0.4 to −0.6 V

Figure 4.51: Impedance spectra of 5 mm × 5 mm macroelectrodes with bottom current collector grids (10 µm mesh and strip width) measured against each other and versus a reference electrode. Measurements were taken in synthetic air at 625 °C with a set bias of 0 to −600 mV between working and counter electrode. Points represent measured spectra, lines represent fit curves, using the circuit shown in figure 4.4.

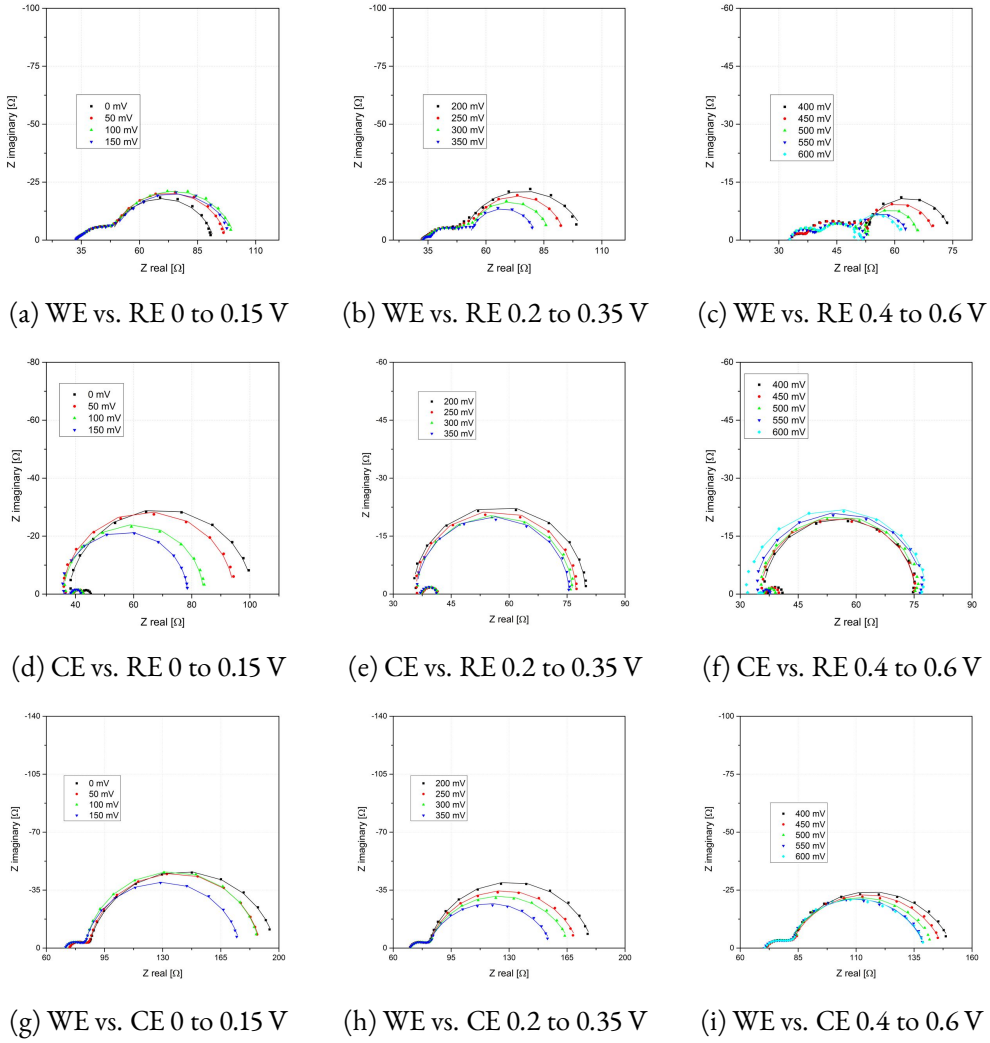


(a) WE vs. RE 0 to 0.15 V (b) WE vs. RE 0.2 to 0.35 V (c) WE vs. RE 0.4 to 0.6 V

(d) CE vs. RE 0 to 0.15 V (e) CE vs. RE 0.2 to 0.35 V (f) CE vs. RE 0.4 to 0.6 V

(g) WE vs. CE 0 to 0.15 V (h) WE vs. CE 0.2 to 0.35 V (i) WE vs. CE 0.4 to 0.6 V

Figure 4.52: Impedance spectra of 5 mm × 5 mm macroelectrodes with bottom current collector grids (10 µm mesh and strip width) measured against each other and versus a reference electrode. Measurements were taken in synthetic air at 625 °C with a set bias of 0 to 600 mV between working and counter electrode. Points represent measured spectra, lines represent fit curves, using the circuit shown in figure 4.4.

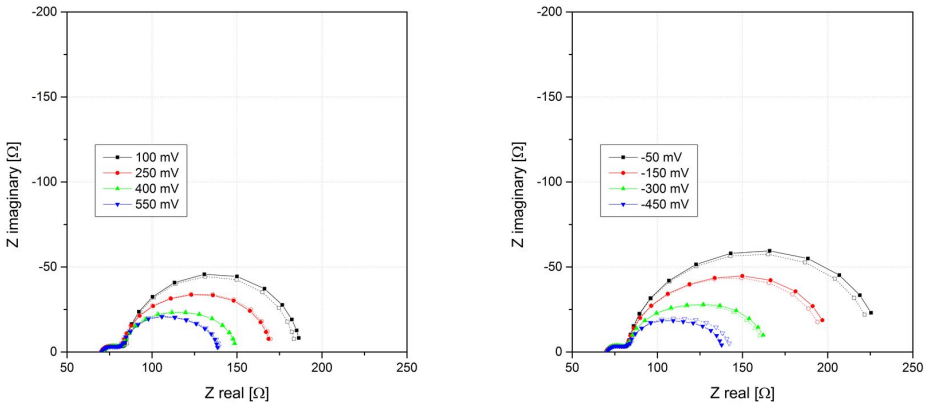


(a) Positive set bias

(b) Negative set bias

Figure 4.53: Impedance spectra of 5 mm × 5 mm macroelectrodes with bottom current collector grid (10 µm mesh and strip width) measured against each other and versus a reference electrode. Measurements were taken in synthetic air at 625 °C with a set bias of 0 to 600 mV between working and counter electrode. Solid lines are the summed spectra of WE vs. RE and CE vs. RE, dotted lines are measured spectra for WE vs. CE.

## 4.7.2 Variation of oxygen partial pressure

In a second experiment, different oxygen/nitrogen mixtures were used to investigate the effect of oxygen partial pressure and electrode overpotential on the oxygen surface exchange kinetics. Measurements were done in 0.025 %, 1 % and 100 % oxygen, at 625 °C. To reduce measurement time and thereby minimize degradation effects, only one electrode was measured against the reference electrode. In figures 4.54 to 4.56 the spectra obtained in different atmospheres with different set bias voltages are shown.

Samples measured in 1 % oxygen show an additional semicircle in the high frequency regime, which is quite unexpected in view of the spectra in other oxidizing atmospheres. As many spectra showed loop features in the high frequency range, an average offset resistance of 45 Ω was estimated by eye. During the impedance measurements, also the DC current was measured. In figure 4.57 the DC current in different atmospheres is plotted against the actual electrode overpotential and over the potential against synthetic air.

A clear difference between anodic and cathodic polarization can be seen, especially for lower oxygen contents. Under cathodic polarization, the current is much lower in atmospheres with less oxygen, particularly at more negative potentials. Considering that the cathodic branch is mostly governed by the oxygen incorporation a strong influence of the atmosphere is not surprising but expectable. The electrode potential versus synthetic air was calculated according to 4.8. Thus, for a given potential versus synthetic air, the defect chemistry in the LSF electrode is the same, regardless of the oxygen partial pressure. Plotting the DC current over this potential shows that indeed the atmosphere is the main factor of influence for the cathodic oxygen incorporation.

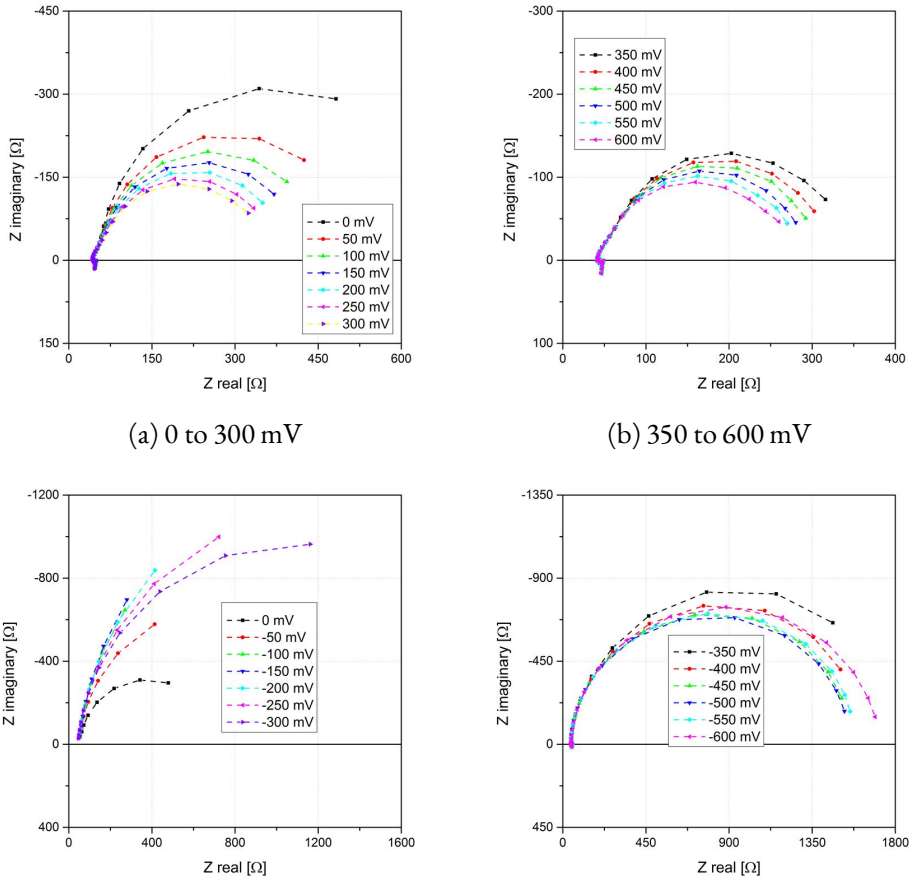


(a) 0 to 300 mV

(b) 350 to 600 mV

(c) 0 to −300 mV

(d) −300 to −600 mV

Figure 4.54: Spectra of a 5 mm × 5 mm macroelectrode with bottom current collector grid (35 µm/5 µm mesh and strip width) measured against a reference electrode. Measurements were taken in 0.025 % oxygen, at 625 °C with a set bias of 0 to ±600 mV between working and counter electrode. Points represent measured spectra, lines are guides to the eye.

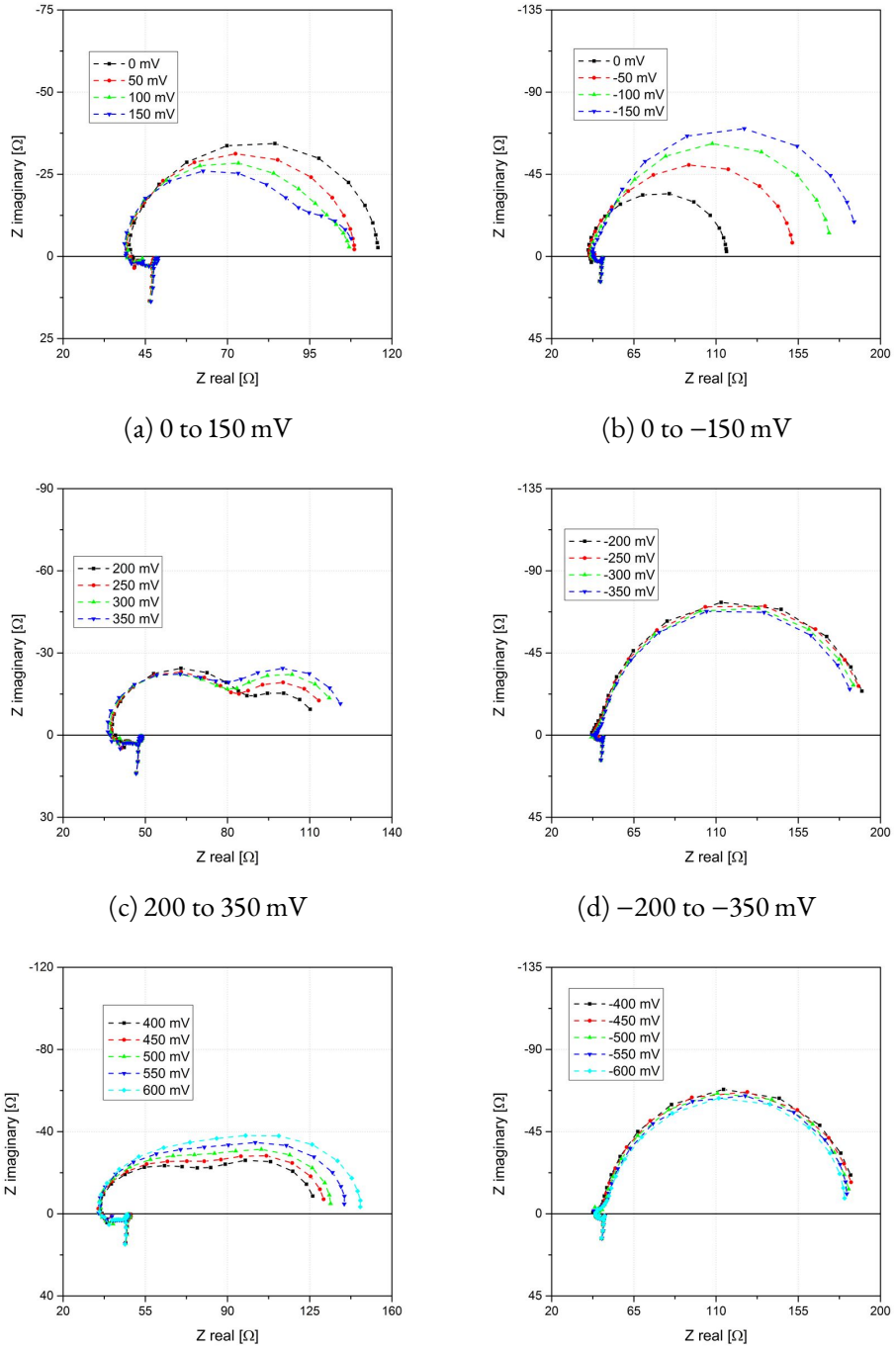


(a) 0 to 150 mV

(b) 0 to −150 mV

(c) 200 to 350 mV

(d) −200 to −350 mV

(e) 400 to 600 mV

(f) −400 to −600 mV

Figure 4.55: Spectra of a 5 mm × 5 mm macroelectrode with bottom current collector grid (35 µm/5 µm mesh and strip width) measured against a reference electrode. Measurements were taken in 1 % oxygen, at 625 °C with a set bias of 0 to ±600 mV between working and counter electrode. Points represent measured spectra, lines are guides to the eye.

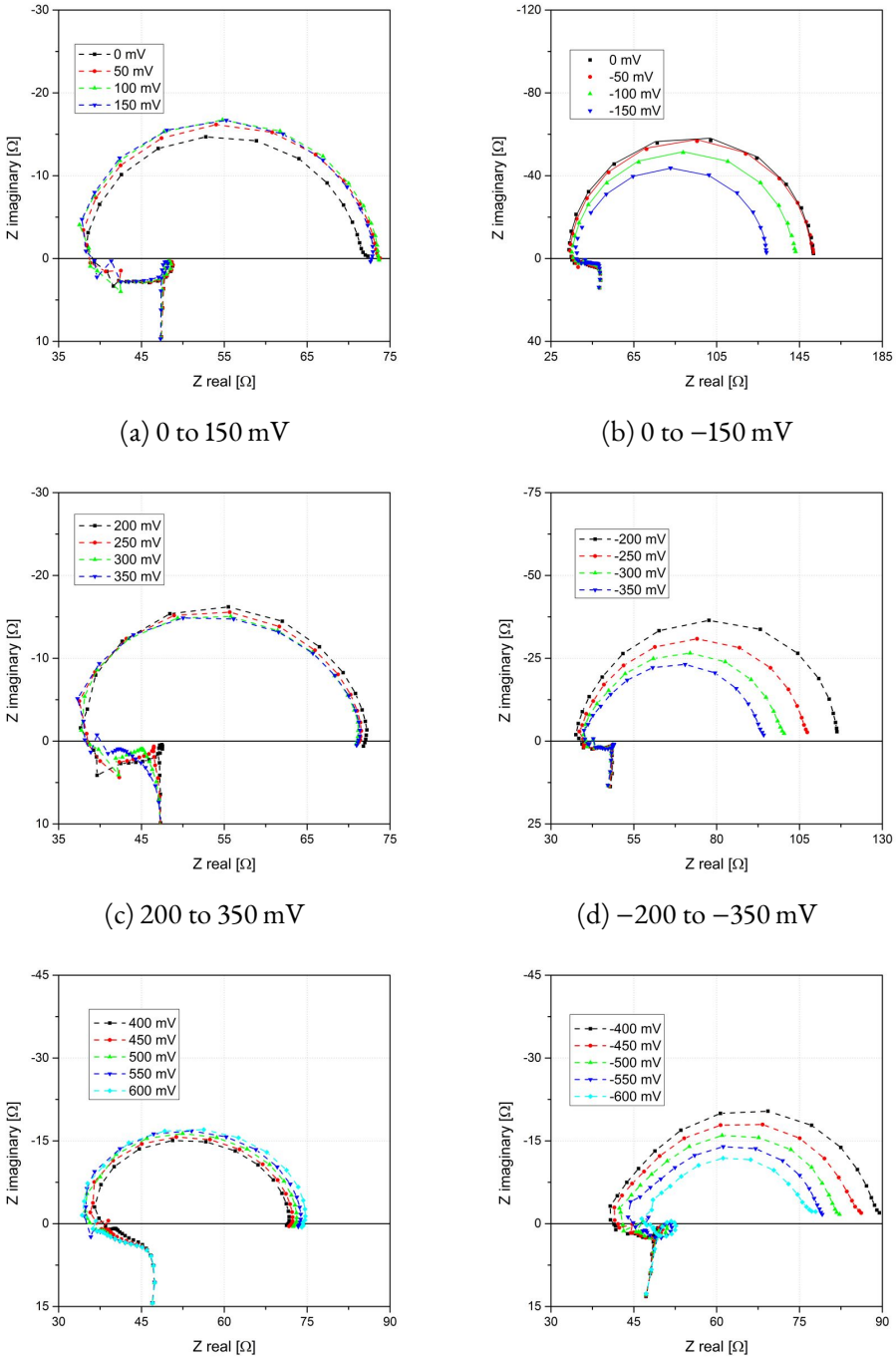


(a) 0 to 150 mV

(b) 0 to −150 mV

(c) 200 to 350 mV

(d) −200 to −350 mV

(e) 400 to 600 mV

(f) −400 to −600 mV

Figure 4.56: Spectra of a 5 mm × 5 mm macroelectrode with bottom current collector grid (35 µm/5 µm mesh and strip width) measured against a reference electrode. Measurements were taken in 100 % oxygen, at 625 °C with a set bias of 0 to ±600 mV between working and counter electrode. Points represent measured spectra, lines are guides to the eye.

The difference in DC current at a given cathodic potential between 1 % and 0.025 % oxygen is larger when plotted versus the potential against air, than when plotted versus the actual electrode overpotential. This suggests that higher oxygen contents in the atmosphere increase the DC current, but also change the defect chemistry in the electrode material leading to lower oxygen exchange currents. An increased oxygen partial pressure in the atmosphere causes a lower concentration of oxygen vacancies in the LSF. The concentration of oxygen vacancies is therefore likely to be of great importance in the rate limiting step. Wang et.al. reported the importance of oxygen vacancies for the oxygen exchange kinetics in $Ba_xSr_{1-x}Co_yFe_{1-y}O_{3-\delta}$. [42]

Under anodic polarization, which is dominated by the oxygen release reaction, the differences between individual atmospheres are much less pronounced. When normalizing to the potential versus air, thereby to the same defect chemical state, these differences are even smaller and diminish under higher polarization. At higher polarization the oxygen release current corresponds to the total current, whereas at lower potentials the incorporation current still contributes to the total current. This suggests that the oxygen release reaction is mostly governed by the defect chemical state within the electrode, and that the surrounding atmosphere plays only a minor role. However more detailed investigations with larger ranges of polarizations and a wider range of oxygen partial pressures are needed for more detailed investigation on this topic.

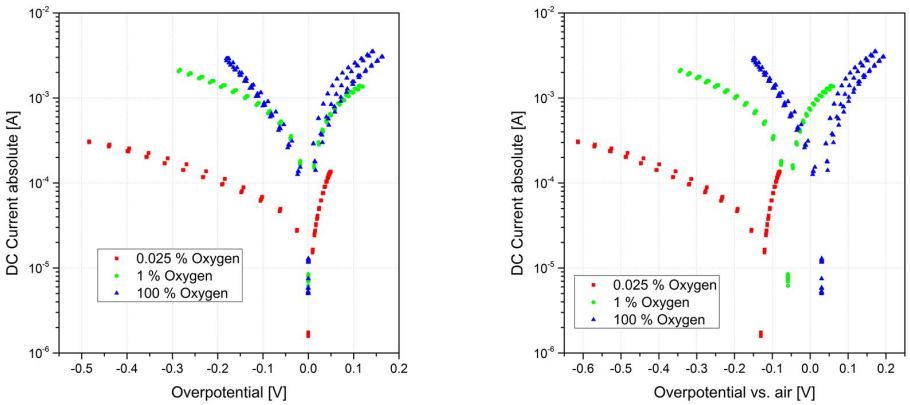


(a) DC current over actual overpotential (b) DC current over potential vs. air

Figure 4.57: DC current versus overpotential curves in different oxidizing atmospheres. Overpotential is plotted as actual electrode overpotential versus the respective atmosphere during the measurement and as overpotential versus synthetic air.

# 5 Summary

Well defined LSF thin film electrodes were prepared by pulsed laser deposition on YSZ single crystal substrates. Electrodes were produced as symmetric 5 mm × 5 mm macroelectrode or as microelectrodes of various size. Platinum current collector grids were produced by lift-off lithography and sputter deposition to ensure uniform polarization of the LSF thin films.

Impedance spectroscopy was used for electrochemical characterization of the LSF thin film electrodes. Measurements were done with different polarizations and in different atmospheres to compare effects of polarization and atmosphere on defect chemistry and oxygen exchange kinetics of the LSF thin film electrodes.

The microstructuring procedure could be shown to increase the surface exchange resistance of microelectrodes compared to as deposited macroelectrodes by at least one order of magnitude in oxidizing atmospheres. In reducing atmospheres no influence of the microstructuring process was observed.

Measurements in humidified hydrogen and synthetic air revealed a drastic decrease of the surface exchange resistance under polarization. A comparison of the bias dependent chemical capacitance in oxidizing and reducing atmospheres showed almost perfect accordance after normalization to the same equivalent oxygen partial pressure. Thereby, it could be shown that the defect chemical state of LSF thin film electrodes solely depends on the potential of oxygen in the electrode, defined by atmosphere and polarization, independent of the reactive species involved in the oxygen exchange reaction.

Comparison of measured chemical capacitances with defect model calculations based on bulk samples showed qualitative agreement between calculated and measured chemical capacitance. However, measurements show significantly lower absolute values of chemical capacitance in oxidizing conditions compared to calculations from bulk data.

Impedance spectroscopy in three point geometry was used to investigate the kinetics of the oxygen exchange reaction on as deposited macroelectrodes. Emphasis was put on analyzing the effects of atmosphere and polarization. Comparison of different oxidizing atmospheres revealed great impact of the atmosphere on the oxygen incorporation reaction, while the oxygen release reaction is mostly governed by the oxygen potential within the electrode.

# 6 Acknowledgments

First and foremost I want to thank my supervisor Ghislain Rupp for his advice, his patience with me and for always taking some time to answer my questions and teach me new things.

Special thanks go to Prof. Jürgen Fleig for giving me the opportunity to do my master thesis on this topic and for providing valuable insights when I was at the end of my wits.

My thanks also go to Andreas Welzl, who together with Ghislain made for the greatest office colleagues. Thank you for all the fun we had, and for all the advice you gave me.

Of course I also want to thank all other members of the research group electrochemistry for a nice working environment, numerous interesting discussions, many valuable words of advice and for all the good times we had.

Finally I want to thank my friends and family for their love, friendship and support.

# Bibliography


[1] B. Timurkutluk, C. Timurkutluk, M. D. Mat, and Y. Kaplan, "A review on cell/stack designs for high performance solid oxide fuel cells," *Renewable and Sustainable Energy Reviews*, vol. 56, pp. 1101–1121, Apr 2016.

[2] M. Laguna-Bercero, "Recent advances in high temperature electrolysis using solid oxide fuel cells: A review," *Journal of Power Sources*, vol. 203, pp. 4–16, Apr 2012.

[3] V. M. Janardhanan and O. Deutschmann, "Modeling of Solid-Oxide Fuel Cells," *Zeitschrift für Physikalische Chemie*, vol. 221, pp. 443–478, Apr 2007.

[4] X.-M. Ge, S.-H. Chan, Q.-L. Liu, and Q. Sun, "Solid Oxide Fuel Cell Anode Materials for Direct Hydrocarbon Utilization," *Adv. Energy Mater.*, vol. 2, pp. 1156–1181, Aug 2012.

[5] T. Matsui, R. Kishida, J.-Y. Kim, H. Muroyama, and K. Eguchi, "Performance Deterioration of Ni-YSZ Anode Induced by Electrochemically Generated Steam in Solid Oxide Fuel Cells," *J. Electrochem. Soc.*, vol. 157, p. B776, 2010.

[6] N. Q. Minh, "Ceramic Fuel Cells," *J American Ceramic Society*, vol. 76, pp. 563–588, Mar 1993.

[7] C. Sun and U. Stimming, "Recent anode advances in solid oxide fuel cells," *Journal of Power Sources*, vol. 171, pp. 247–260, Sep 2007.

[8] S. Tao and J. T. S. Irvine, "A redox-stable efficient anode for solid-oxide fuel cells," *Nat Mater*, vol. 2, pp. 320–323, Mar 2003.

[9] S. Cho, D. E. Fowler, E. C. Miller, J. S. Cronin, K. R. Poeppelmeier, and S. A. Barnett, "Fe-substituted $SrTiO_3$ - $Ce_{0.9}Gd_{0.1}O_2$ composite anodes for solid oxide fuel cells," *Energy Environ. Sci.*, vol. 6, no. 6, p. 1850, 2013.

[10] S. P. Jiang, L. Zhang, and Y. Zhang, "Lanthanum strontium manganese chromite cathode and anode synthesized by gel-casting for solid oxide fuel cells," *Journal of Materials Chemistry*, vol. 17, no. 25, p. 2627, 2007.

[11] E. Konysheva and J. T. Irvine, "Effect of Minor Additions of $CeO_2$ on Conductivity of Perovskites with Mixed Ionic-Electronic Conductivity," in *ECS Transactions*, pp. 115–122, The Electrochemical Society, 2008.

[12] E. Konysheva and J. T. S. Irvine, "Thermochemical and Structural Stability of A- and B-Site-Substituted Perovskites in Hydrogen-Containing Atmosphere," *Chem. Mater.*, vol. 21, pp. 1514–1523, Apr 2009.

[13] T. Nakamura, G. Petzow, and L. Gauckler, "Stability of the perovskite phase $LaBO_3$ (B = V, Cr, Mn, Fe, Co, Ni) in reducing atmosphere I. Experimental results," *Materials Research Bulletin*, vol. 14, pp. 649–659, May 1979.

[14] C. Savaniu and J. Irvine, "La-doped $SrTiO_3$ as anode material for IT-SOFC," *Solid State Ionics*, vol. 192, pp. 491–493, Jun 2011.

[15] E. Lay, G. Gauthier, S. Rosini, C. Savaniu, and J. T. Irvine, "Ce-substituted LSCM as new anode material for SOFC operating in dry methane," *Solid State Ionics*, vol. 179, pp. 1562–1566, Sep 2008.

[16] P. Plonczak, M. Gazda, B. Kusz, and P. Jasinski, "Fabrication of solid oxide fuel cell supported on specially performed ferrite-based perovskite cathode," *Journal of Power Sources*, vol. 181, pp. 1–7, Jun 2008.

[17] M. Kuhn, S. Hashimoto, K. Sato, K. Yashiro, and J. Mizusaki, "Oxygen nonstoichiometry, thermo-chemical stability and lattice expansion of $La_{0.6}Sr_{0.4}FeO_{3-\delta}$," *Solid State Ionics*, vol. 195, pp. 7–15, Jul 2011.

[18] M. Gazda, B. Kusz, P. Płończak, S. Molin, and P. Jasinski, "Chemical Interaction between Perovskite $La_{0.6}Sr_{0.4}FeO_{3-\delta}$ and Super-Ionic $Zr_{0.84}Y_{0.16}O_x$," *Acta Physica Polonica A*, vol. 114, no. 1, p. 135, 2008.

[19] M. Søgaard, P. Vang Hendriksen, and M. Mogensen, "Oxygen nonstoichiometry and transport properties of strontium substituted lanthanum ferrite," *Journal of Solid State Chemistry*, vol. 180, pp. 1489–1503, Apr 2007.

[20] J. A. Bahteeva, I. A. Leonidov, M. V. Patrakeev, E. B. Mitberg, V. L. Kozhevnikov, and K. R. Poeppelmeier, "High-temperature ion transport in $La_{1-x}Sr_xFeO_{3-\delta}$," *J Solid State Electrochem*, vol. 8, Feb 2004.

[21] J. Mizusaki, T. Sasamoto, W. R. Cannon, and H. K. Bowen, "Electronic Conductivity, Seebeck Coefficient, and Defect Structure of $La_{1-x}Sr_xFeO_{3-\delta}$ (x=0.l, 0.25)," *J American Ceramic Society*, vol. 66, pp. 247–252, Apr 1983.

[22] M. Patrakeev, I. Leonidov, V. Kozhevnikov, and K. Poeppelmeier, "p-Type electron transport in $La_{1-x}Sr_xFeO_{3-\delta}$ at high temperatures," *Journal of Solid State Chemistry*, vol. 178, pp. 921–927, Mar 2005.

[23] E. V. Bongio, H. Black, F. C. Raszewski, D. Edwards, C. J. McConville, and V. R. W. Amarakoon, "Microstructural and High-Temperature Electrical Characterization of $La_{1-x}Sr_xFeO_{3-\delta}$," *Journal of Electroceramics*, vol. 14, pp. 193–198, Jul 2005.

[24] M. C. Kim, S. J. Park, H. Haneda, J. Tanaka, and S. Shirasaki, "High temperature electrical conductivity of $La_{1-x}Sr_xFeO_{3-\delta}$ x>0.5," *Solid State Ionics*, vol. 40-41, pp. 239–243, Aug 1990.

[25] S. Kogler, *Electrochemical properties of $La_{0.6}Sr_{0.4}FeO_{3-\delta}$ in reducing and oxidizing conditions*. PhD thesis, Technische Universität Wien, 2014.

[26] S. Kogler, A. Nenning, G. M. Rupp, A. K. Opitz, and J. Fleig, "Comparison of Electrochemical Properties of $La_{0.6}Sr_{0.4}FeO_{3-\delta}$ Thin Film Electrodes: Oxidizing vs. Reducing Conditions," *Journal of the Electrochemical Society*, vol. 162, pp. F317–F326, Dec 2014.

[27] J. Yoo, A. Verma, S. Wang, and A. J. Jacobson, "Oxygen Transport Kinetics in $SrFeO_{3-\delta}$, $La_{0.5}Sr_{0.5}FeO_{3-\delta}$, and $La_{0.2}Sr_{0.8}Cr_{0.2}Fe_{0.8}O_{3-\delta}$ Measured by Electrical Conductivity Relaxation," *J. Electrochem. Soc.*, vol. 152, no. 3, p. A497, 2005.

[28] J. E. ten Elshof, "Oxygen Exchange and Diffusion Coefficients of Strontium-Doped Lanthanum Ferrites by Electrical Conductivity Relaxation," *J. Electrochem. Soc.*, vol. 144, no. 3, p. 1060, 1997.

[29] J. Mizusaki, M. Yoshihiro, S. Yamauchi, and K. Fueki, "Thermodynamic quantities and defect equilibrium in the perovskite-type oxide solid solution $La_{1-x}Sr_xFeO_{3-\delta}$," *Journal of Solid State Chemistry*, vol. 67, pp. 1–8, Mar 1987.

[30] T. Kawada, J. Suzuki, M. Sase, A. Kaimai, K. Yashiro, Y. Nigara, J. Mizusaki, K. Kawamura, and H. Yugami, "Determination of Oxygen Vacancy Concentration in a Thin Film of $La_{0.6}Sr_{0.4}CoO_{3-\delta}$ by an Electrochemical Method," *Journal of The Electrochemical Society*, vol. 149, no. 7, p. E252, 2002.

[31] S. Adler, X. Y. Chen, and W. J.R., "Mechanisms and rate laws for oxygen exchange on mixed-conducting oxide surfaces," *Journal of Catalysis*, vol. 245, pp. 91–109, Jan 2007.

[32] A. M. Ritzmann, A. B. Muñoz-García, M. Pavone, J. A. Keith, and E. A. Carter, "Ab Initio DFT+U Analysis of Oxygen Vacancy Formation and Migration in $La_{1-x}Sr_xFeO_{3-\delta}$ ( x = 0, 0.25, 0.50)," *Chemistry of Materials*, vol. 25, pp. 3011–3019, Aug 2013.

[33] J. Jamnik, "Treatment of the Impedance of Mixed Conductors Equivalent Circuit Model and Explicit Approximate Solutions," *J. Electrochem. Soc.*, vol. 146, no. 11, p. 4183, 1999.

[34] W. C. Chueh and S. M. Haile, "Electrochemical studies of capacitance in cerium oxide thin films and its relationship to anionic and electronic defect densities," *Physical Chemistry Chemical Physics*, vol. 11, no. 37, p. 8144, 2009.

[35] J. Jamnik and J. Maier, "Generalised equivalent circuits for mass and charge transport: chemical capacitance and its implications," *Physical Chemistry Chemical Physics*, vol. 3, no. 9, pp. 1668–1678, 2001.

[36] A. Nenning, A. K. Opitz, T. M. Huber, and J. Fleig, "A novel approach for analyzing electrochemical properties of mixed conducting solid oxide fuel cell anode materials by impedance spectroscopy," *Phys. Chem. Chem. Phys.*, vol. 16, no. 40, pp. 22321–22336, 2014.

[37] D. R. Lide, ed., *CRC handbook of chemistry and physics*. Fiona Macdonald, 90 ed., 2010.

[38] A. Opitz, *Die Kinetik der $O_2$ -Reduktion an mikrostrukturierten Platinschichten auf Yttrium-stabilisiertem $ZrO_2$*. PhD thesis, Technische Universität Wien, 2008.

[39] A. K. Opitz, A. Nenning, C. Rameshan, R. Rameshan, R. Blume, M. Hävecker, A. Knop-Gericke, G. Rupprechter, J. Fleig, and B. Klötzer, "Enhancing Electrochemical Water-Splitting Kinetics by Polarization-Driven Formation of Near-Surface Iron(0): An In Situ XPS Study on Perovskite-Type Electrodes," *Angewandte Chemie International Edition*, vol. 54, pp. 2628–2632, Dec 2014.

[40] F. S. Baumann, J. Fleig, M. Konuma, U. Starke, H.-U. Habermeier, and J. Maier, "Strong Performance Improvement of $La_{0.6}Sr_{0.4}Co_{0.8}Fe_{0.2}O_{3-\delta}$ SOFC Cathodes by Electrochemical Activation," *J. Electrochem. Soc.*, vol. 152, no. 10, p. A2074, 2005.

[41] X. Chen, "Electrochemical behavior of La(Sr)$MnO_3$ electrode under cathodic and anodic polarization," *Solid State Ionics*, vol. 167, pp. 379–387, Feb 2004.

[42] L. Wang, R. Merkle, and J. Maier, "Surface Kinetics and Mechanism of Oxygen Incorporation Into $Ba_{1-x}Sr_xCo_yFe_{1-y}O_{3-\delta}$ SOFC Microelectrodes," *Journal of The Electrochemical Society*, vol. 157, no. 12, p. B1802, 2010.